# Dynamics and Control of Nonholonomic Systems with Internal Degrees of Freedom

---

A Dissertation
Presented to
the Graduate School of
Clemson University

---

In Partial Fulfillment
of the Requirements for the Degree
Doctor of Philosophy
Mechanical Engineering

---

by
Vitaliy Fedonyuk
May 2020

---

Accepted by:
Dr. Phanindra Tallapragada, Committee Chair
Dr. Suyi Li
Dr. Ardalan Vahidi
Dr. Martin Schmoll

ProQuest Number: 27956297

ProQuest.

ProQuest 27956297

الم_ارة للاستشارات

www.manaraa.com
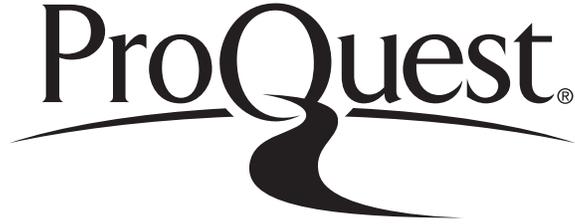
# Abstract

Nonholonomic systems model many robots as well as animals and other systems. Although such systems have been studied extensively over the last century, much work still remains to be done on their dynamics and control. Many techniques have been developed for controlling kinematic nonholonomic systems or simplified dynamic versions, however control of high dimensional, underactuated nonholonomic systems remains to be addressed. This dissertation helps fill this gap by developing a control algorithm that can be applied to systems with three or more configuration variables and just one input. We also analyze the dynamic effects of passive degrees of freedom and elastic potentials which are commonly observed in such systems showing that the addition of a passive degree of freedom can even be used to improve the locomotion characteristics of a system. Such elastic potentials can be present due to compliant mechanisms or origami, both of which can exhibit bistability and many other properties that can be useful in the design of robots.

# Acknowledgments

First of all I would like to thank my advisor, Dr. Phanindra Tallapragada. I am very fortunate to have met him through the Departmental Honors program at Clemson as I always felt we were well matched by both personality and research interests. His passion for dynamics inspired my interest in research and our undergraduate research together led me to consider graduate school more seriously. He introduced me to interesting problems, pushed me when I needed it and always provided excellent guidance in my graduate career. I would also like to thank my lab mates Beau Pollard and Jake Buzhardt for their company in the office and for our many discussions, scholarly and otherwise. My graduate experience would have been much more difficult without the friendship and support of my brother, Andriy Fedonyuk. Finally I would like to thank my parents and all my family for all their love, support and encouragement throughout my academic journey.

# Table of Contents

# Chapter 1

# Introduction

Nonholonomic constraints play a key role in the dynamics of mobile robots due to the relationship between rolling motion and no slip constraints [6]. The study of their dynamics and control, therefore, becomes critical for improving performance of wheeled robots. The research on nonholonomic dynamics has been focused on the study of certain canonical systems with nonholonomic constraints. These include the rolling coin [51], the roller racer [4,11], the snakeboard [11,18,61,62], and the Chaplygin sleigh [9, 15, 22, 25, 41, 60, 79]. Early work on such problems involved finding integrable cases and studying the stability of particular solutions [10]. Nonholonomic systems can be dynamic or kinematic [75]. Kinematic systems are such that the kinematics of the system are fully prescribed by the control inputs. Such systems often have multiple nonholonomic constraints and the shape is assumed to be fully controlled. Currently the majority of the work on control of nonholonomic systems considers kinematic systems [6, 44, 55]. Such control techniques make use of the properties of kinematic systems such as driftlessness, simplifying analysis as compared to their dynamic counterparts.

This dissertation research focuses on dynamic systems where the number of nonholonomic constraints is less than the number of configuration variables. Dynamic systems exhibit more complex dynamics as the velocities are not fully prescribed by the shape but determined by differential equations allowing for phenomena such as fixed points, limit cycles, bifurcations and chaos. Furthermore, the systems considered herein are underactuated. That is the system does not have enough inputs to follow arbitrary trajectories in the configuration space. This allows us to investigate how nonholonomic constraints and passive degrees of freedom can be used as a passive means of control:

1

to stabilize the system, maneuver it or change its dynamics entirely. Underactuated control may be invaluable in improving energy efficiency of robots as less motors and other actuators are required.

In particular, the Chaplygin sleigh is the case study of this dissertation research [15] (Fig. 1.1). The system consists of a mass with a runner or wheel that is not allowed to slip laterally in the $Y_b$ direction. The system was first introduced by S.A. Chaplygin in 1921 as an example of what would come to be known as Chaplygin systems, or integrable nonholonomic systems [12]. The integrability of the sleigh can be exploited to control its heading, as for example in [79]. However the Chaplygin sleigh is not fully controllable. Due to the invariance of energy, any control input increases the energy of the sleigh. For robotic applications, however, it becomes useful to consider frictional dissipation as this represents an experimental environment more accurately. For this reason many of the systems we consider contain dissipation as done in many other recent works [3, 5, 18]. Viscous dissipation is also used to model hydrodynamic forces which helps us exploit the similarities between land and water nonholonomic systems [67].

The interaction between a Joukowski foil-shaped body and the fluid through vortex shedding has been shown to be an affine nonholonomic constraint [41, 78]. Moreover, this constraint has a formal similarity to that of the constraint on the Chaplygin sleigh. Experimental data related to the motion of a swimming robot propelled by an internal rotor shows that its motion is very similar to that of the Chaplygin sleigh [69]. The Chaplygin sleigh thus serves as a terrestrial analogue of swimming robots and this analogy can be exploited to understand the more complicated dynamics of fluid-robot interaction. In addition to this, almost all commonly encountered nonholonomic systems have constraints of the same affine form as the Chaplygin sleigh making the sleigh an appropriate case study for the dynamics of all such systems.

The locomotion characteristics of many animals, including those of fish, show that rhythmic or periodic actuation, for instance through central pattern generators, plays an important role [36]. There has also been a rich history within the area of nonholonomic mechanics where motion planning was achieved through sinusoidal inputs [56]. For example certain ratios of input frequencies are shown to produce useful gaits for the snakeboard in [61] and another snake like robot in [63]. We therefore consider sinusoidal inputs in control of the systems considered herein. In our works [25, 27] we have shown that for many systems sinusoidal forcing elicits a limit cycle response which can be calculated using the harmonic balance method [30, 66]. A combination of harmonic balance method and feedback can then be used for simultaneous heading and velocity control as shown in [25]. This

2
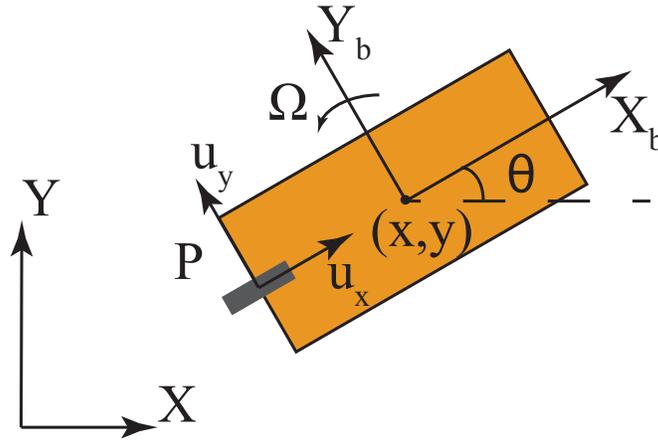
Figure 1.1: Chaplygin sleigh

dissertation extends such techniques and shows their applicability to many nonholonomic systems with a periodic response. One such extension is developing a path tracking algorithm based on harmonic balance techniques as well as vector pursuit [77]. Pursuit algorithms are based on choosing a target point on the path which can be visualized as an evader vehicle and steering the robot towards this target referred to as the goal point. Such algorithms are intuitive and found to work well in practice [?].

Passive degrees of freedom are naturally utilized by animals to facilitate efficient motion. Examples are the passive flapping of wings by insects to generate lift in hovering flight [21, 82], passive deformations of fish to extract energy from ambient wake in a stream [65, 72]. Experiments have demonstrated that the maneuverability of swimming fish-like robots improves with passive tails, [71]. In particular such fish like swimming robots have been shown to be subjected to nonholonomic constraints [67, 78, 81]. This work will explore the effect passive degrees of freedom have on nonholonomic systems and how they can be used for efficient motion and control of mobile robots.

With passive degrees of freedom one can also elastic potentials which serve as an additional passive mechanism to achieve desired behavior. Currently there is little literature on the role springs can play in nonholonomic system. The roller racer with a passive linear spring is considered in [50] and shown to move along a line asymptotically. In [26] we find that similar trajectories are possible for a Chaplygin sleigh with an elastic joint and that motion on a circle is also possible. As a natural extension of passive degrees of freedom with springs we would also like to consider bistable mechanisms. Such mechanisms can retain two possible configurations with no additional forces.

3

Bistable mechanisms can also be realized using compliant mechanisms [34, 38, 53]. Such mechanisms combine multiple rigid links and springs into one or a few flexible parts. Compliant mechanisms can, therefore, greatly reduce assembly time and the number of parts in robots. Compliance is also natural to consider in the context of bioinspired locomotion and control as animals, especially ones like fish and snakes use passive deformation and compliance within their bodies to propel themselves and maneuver.

The contributions of this dissertation are outlined as follows.

- In Chapter 3 we developed a novel method for control of underactuated nonholononomic systems. The systems we consider have three or more configuration variables with only one control input. We show that simultaneous velocity and heading control is possible by regulating the steady state limit cycle dynamics of the system. This is done with the help of the harmonic balance method.

- In Chapter 4 we extend the techniques in Chapter 3 to develop path following for such systems. We show that with just one control input we are able to steer a system along a path with a specified velocity.

- We show an example of how a passive degree of freedom can cause a nonholonomic system to become chaotic in Chapter 5.

- We then introduce an elastic potential to the system in Chapter 6 and show that this causes the dynamics to become regular as we observe limit cycles (Hopf bifurcations) and convergence to fixed points instead of chaos.

- In Chapter 7 we show that the introduction of a passive degree of freedom can in fact improve the locomotion characteristics like speed and energy efficiency of an underactuated nonholonomic system by comparing a Chaplygin sleigh with a degree of freedom to one without.

- Finally, in Chapter 8 we give two more examples of how elastic potentials can be introduced in nonholonomic systems. Namely by compliant mechanisms or origami. Such systems can exhibit bistability and different dynamics in different stable configurations.

# Chapter 2

# Equations of Motion

The Euler Lagrange equations of motion for nonholonomic systems in terms of Lagrange multipliers were first introduced by N.M. Ferrers in 1971 [28]. This method is useful as it yields explicit expressions for the forces required to enforce the nonholonomic constraints. Knowledge of such forces is crucial in the design of robots as wheels are subject to slip should these forces become too high.

The position of a robot may be described by generalized coordinates $q = (g, r) \in \mathbb{R}^n$ where $g \in \mathbb{R}^m$ denotes the configuration of the robot ($g \in SE(2)$ for example) and $r \in \mathbb{R}^k$ denotes the shape of the robot such as the angles between parts of the robot ($n = m + k$). The configuration describes the position of the robot in a global reference frame whereas the shape is independent of the global position. The generalized coordinates $q$ must fully define the configuration of the system relative to some reference configuration. For the Chaplygin sleigh with a passive rotor, for example $g = (x, y, \theta) \in SE(2)$, the position and orientation of the sleigh in the plane and $r = \phi \in S^1$, the orientation of the rotor relative to the sleigh. If any of the shape variables $r$ are not controlled we call these passive degrees of freedom. The Lagrangian for a mechanical system is given by

$$\mathcal{L} = \mathcal{T}(q, \dot{q}) - \mathcal{V}(q). \tag{2.1}$$

Here $T = \frac{1}{2}\dot{q}^T \mathcal{M}(q)\dot{q}$ is the kinetic energy of the system with $M(q)$ being the inertia tensor and $\mathcal{V}(\delta)$ is its potential energy. The system must also satisfy $p$ nonholonomic constraints of the

form

$$\mathcal{W}(q)\dot{q} = 0 \tag{2.2}$$

where $\mathcal{W}(q) \in \mathbb{R}^{p \times n}$. Note that the constraint is linear in velocities as is the case for most non-holonomic systems, especially those which involve wheeled locomotion. A system with $n$ generalized coordinates and $p$ constraints has $n - p$ degrees of freedom, or allowable directions of motion. Suppose the system is also subject to $k$ control inputs. A major contribution of this dissertation is the development of a controller for systems where $n - p - k \geq 1$. We may also consider viscous dissipation to model frictional effects a robot experiences. This is done using a Raleigh dissipation function of the form

$$\mathcal{R} = \frac{1}{2} \sum_i c_i v_i^2 \tag{2.3}$$

where $v_i$ is the velocity of the point where friction is applied or the angular velocity where rotational damping is present and $c_i$ is the dissipation coefficient. The equations of motion with multipliers are then given by

$$\frac{d}{dt}\left(\frac{\partial \mathcal{L}}{\partial \dot{q}_i}\right) - \frac{\partial \mathcal{L}}{\partial q_i} = \mathcal{W}_{ij}\lambda_j + -\frac{\partial \mathcal{R}}{\partial q_i} + \tau_i(t) \tag{2.4}$$

where $\lambda_j$ is the Lagrange multiplier corresponding to the $j$'th constraint, $\mathcal{W}_{i,j}$ is the coefficient of $\dot{q}_k$ in (8.4), and $\tau_i$ are the other external forces and torques.

Straight forward calculations yield the Euler-Lagrange equations as

$$\begin{bmatrix} \mathcal{M} & -\mathcal{W}^T \\ \mathcal{W} & 0 \end{bmatrix} \begin{bmatrix} \ddot{q} \\ \lambda \end{bmatrix} = \mathcal{B}(q,\dot{q}) + \Gamma(q,\dot{q}) + \tau(t) \tag{2.5}$$

where

$$\mathcal{B}(q,\dot{q}) = \begin{bmatrix} \mathcal{C}(q,\dot{q})\dot{q} \\ \dot{\mathcal{W}}\dot{q} \end{bmatrix} + \frac{\partial \mathcal{L}}{\partial q}.$$

Here $\frac{\partial \mathcal{L}}{\partial q}$ is a vector of partial derivatives of the potential terms. The matrix $\mathcal{C}(q,\dot{q})$ contains elements $C_{jk} = \sum_{i=1}^{n} C_{ijk}\dot{q}_i$ where $C_{ijk}$ are the Christoffel symbols of the first kind computed as $C_{ijk} = \frac{\partial \mathcal{M}_{kj}}{\partial q_i} + \frac{\partial \mathcal{M}_{ki}}{\partial q_j} - \frac{\partial \mathcal{M}_{ij}}{\partial q_k}$.

The last $p$ equations of (2.9) is obtained by differentiating the nonholonomic constraints

6

with respect to time. This is needed to complete the system in this form and solve for the velocities. For many systems we can eliminate the constraint force using gaussian elimination in order to obtain the equations in matrix form useful for fixed points analysis and other analytical techniques. The systems we consider in this research have the property of gauge symmetry, or invariance of the equations of motion under rigid body motion of the vehicle [42, 76]. This is to say that the dynamics are independent of $g$ and this allows us to rewrite the equations of motion in terms of only shape variables and body velocities to eliminate dependence on $g$. For this we define a body fixed velocity vector $\xi = R\dot{q}$ such that the velocities are always aligned with a body-fixed axis. For example for the Chaplygin sleigh we typically chose

$$\xi = \begin{bmatrix} u_x \\ u_y \\ \omega \end{bmatrix} = \begin{bmatrix} \cos(\theta) & \sin(\theta) & 0 \\ -\sin(\theta) & \cos(\theta) & -b \\ 0 & 0 & 1 \end{bmatrix} \begin{bmatrix} \dot{x} \\ \dot{y} \\ \dot{\theta} \end{bmatrix} \tag{2.6}$$

This is a natural choice as the nonholonomic constraint of the sleigh can now be expressed as $u_y = 0$ and one of the equations of motion becomes trivial ($\dot{u}_y = 0$). Therefore putting the equations of motion in terms of $\xi$ can not only eliminate dependence on $g$ but also reduce the order of the system in many cases. The reduction of equations is performed by computing the intertial velocities and accelerations in terms of $\xi$ and $r$ using

$$\dot{q} = R^{-1}\xi, \quad \text{and} \quad \ddot{q} = \dot{R}^{-1}\xi + R^{-1}\dot{\xi} \tag{2.7}$$

and substituting the above expressions into 2.9. This yields the following system.

$$\begin{bmatrix} \mathcal{M}_b & 0 & -\mathcal{W}_b^T \\ 0 & I & 0 \\ \mathcal{W}_b & 0 & 0 \end{bmatrix} \begin{bmatrix} \dot{\xi} \\ \dot{r} \\ \lambda \end{bmatrix} = \mathcal{B}_b(\xi, r) + \Gamma(\xi) + \tau(t) \tag{2.8}$$

where the $\dot{r}$ equations are needed to solve for the shape variables and $\mathcal{B}_b$ is defined according to the above partition. The reduced equations of motion as well as expressions for the Lagrange multipliers

7

are then given as

$$
\begin{bmatrix} \dot{\xi} \\ \dot{r} \\ \lambda \end{bmatrix} = \begin{bmatrix} \mathcal{M}_b & 0 & -\mathcal{W}_b^T \\ 0 & I & 0 \\ \mathcal{W}_b & 0 & 0 \end{bmatrix}^{-1} (\mathcal{B}_b(\xi, r) + \Gamma(\xi) + \tau(t)) = \mathcal{F}(\xi, r, t) \tag{2.9}
$$

**Example 2.0.1.** As an example we will derive and briefly analyze the equations of motion for the classical Chaplygin sleigh. As mentioned, the configuration of the sleigh is parameterized by $q = (x, y, \theta)$. The Lagrnagian is given as

$$
\mathcal{L} = \frac{1}{2}m(\dot{x}^2 + \dot{y}^2) + \frac{1}{2}J\dot{\theta}^2
$$

The sleigh is subject to a nonholonomic constraint that point $P$ is not allowed to slip in the $Y_b$ direction. This is expressed as

$$
[-\sin(\theta), \cos(\theta), -b]\dot{q} = 0
$$

and using 2.4 the Euler Lagrange equations become

$$
m\ddot{x} = -\lambda\cos(\theta) \tag{2.10}
$$

$$
m\ddot{y} = \lambda\sin(\theta) \tag{2.11}
$$

$$
J\ddot{\theta} = -b\lambda. \tag{2.12}
$$

Next we define $\xi$ according to 2.6 and use 2.7 to find $\dot{q}$ and $\ddot{q}$ in terms of $\xi$ and $\theta$. We then substitute these expressions into 2.10 to obtain the following system:

$$
\begin{bmatrix} m\cos(\theta) & 0 & -mb\sin(\theta) & -\sin(\theta) \\ m\sin(\theta) & 0 & mb\cos(\theta) & \cos(\theta) \\ 0 & 0 & J & -b \\ 0 & 1 & 0 & 0 \end{bmatrix} \begin{bmatrix} \dot{u}_x \\ \dot{u}_y \\ \dot{\omega} \\ \lambda \end{bmatrix} = \begin{bmatrix} -u_x\omega\sin(\theta) - \omega^2 b\cos(\theta) \\ u_x\omega\cos(\theta) - \omega^2 b\sin(\theta) \\ 0 \\ 0 \end{bmatrix} \tag{2.13}
$$

As the fourth equation is trivial and decoupled, we typically set $u_x = u$ and consider the system

$$\begin{bmatrix} m\cos(\theta) & -mb\sin(\theta) & -\sin(\theta) \\ m\sin(\theta) & mb\cos(\theta) & \cos(\theta) \\ 0 & J & -b \end{bmatrix} \begin{bmatrix} \dot{u} \\ \dot{\omega} \\ \lambda \end{bmatrix} = \begin{bmatrix} -u_x\omega\sin(\theta) - \omega^2 b\cos(\theta) \\ u_x\omega\cos(\theta) - \omega^2 b\sin(\theta) \\ 0 \end{bmatrix}. \tag{2.14}$$

Using 2.9 we derive the final equations as well as the expression for the constraint force to be.

$$\begin{bmatrix} \dot{u} \\ \dot{\omega} \\ \lambda \end{bmatrix} = \begin{bmatrix} b\omega^2 \\ -\frac{mb}{J+mb^2}u\omega \\ \frac{Jm}{J+mb^2}u\omega \end{bmatrix} \tag{2.15}$$

Note that due to gauge symmetry the above equations are independent of the sleigh's orientation in the global frame. Notice that $\dot{u} > 0$ and when $u > 0$, $\omega$ converges to zero. Therefore, due to the conservation of energy the assymptotic motion of the sleigh is that of a straight line with $u > 0$ and $\omega = 0$. The phase plot as well as a sample trajectory of the sleigh are shown in Fig. 2.1. In Fig. 2.1 (a) we see that trajectories are elliptical in the phase space. Figure 2.1 (b) shows the assymptotic linear motion of the sleigh given some initial conditions
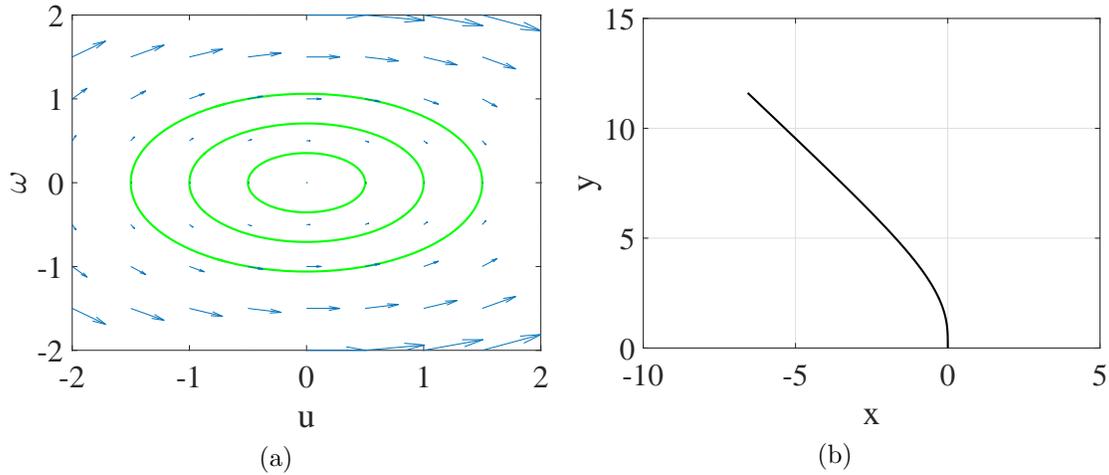


Figure 2.1: A phase portrait of the Chaplygin sleigh is shown in a) with sample trajectories shown as solid curves. A generic trajectory of the sleigh is shown in b). Initial conditions are $(u(0) = 0, \omega(0) = 1)$.

We will now see how a torque driven internal rotor can be used to control the sleigh. This was done on the idealized sleigh in [80], however due to conservation of energy any control input

9

causes the energy of the sleigh to increase rendering the sleigh uncontrollable. As the absence of dissipation is unrealistic, we introduce viscous dissipation to the sleigh and develop a controller for the modified system in the following Chapter.

# Chapter 3

# Control of Dynamic Systems via Estimation of Limit Cycles

In [25, 27] we developed a control scheme to control the average velocity and orientation of the sleigh using torque as the only means of actuation. These results are summarized herein. We model frictional effects via Raleigh dissipation at point $P$. This is done using the dissipation function

$$\mathcal{R} = \frac{1}{2}cu^2 = \frac{1}{2}c(\dot{x}\cos\theta + \dot{y}\sin\theta)^2.$$

The final equations become similar to those of the classical sleigh but with additional terms due to the friction and torque.

$$\dot{u} = b\omega^2 - \frac{c}{m}u \tag{3.1}$$

$$\dot{\omega} = \frac{-mbu\omega + \tau}{I + mb^2} \tag{3.2}$$

There is a rich history within the area of nonholonomic mechanics, where motion planning was achieved through sinusoidal inputs [56, 61, 63]. Motivated by this we consider inputs of the form $\tau = A\sin(\Omega t + \phi)$. However, as $\phi$ does not affect the asymptotic behavior of the sleigh we take it to

11

be zero simplifying our formulation. A typical trajectory of the sleigh under such forcing is shown in Fig. 3.1.
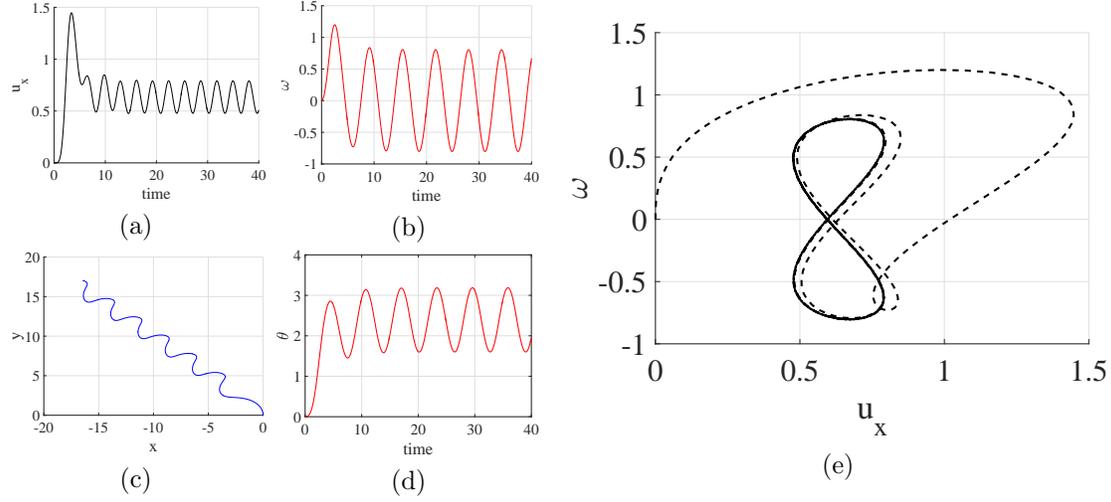


Figure 3.1: Simulation of chaplygin sleigh with $(u(0), \omega(0)) = (0,0)$ with the input being $I_r \ddot{\phi} = -2 \sin t$, i.e. $A = 2$ and $\Omega = 1$.

In Figs. 3.1 (a) and (b) we see that the longitudinal velocity becomes periodic with some nonzero mean while the angular velocity also becomes periodic but with zero mean. This is also seen in Fig. 3.1 as the velocities converge to a figure eight shape limit cycle in the $(u, \omega)$ space. Similar limit cycles are seen in other nonholonomic systems [3, 5, 13]. The existence of a limit cycle for the viscous sleigh is also proven for a certain range of parameters in [3]. In Figs. 3.1 (c) and (d) we see that these dynamics lead to a serpentine trajectory in the $(x, y)$ plane with some constant average angle.

## 3.1    Approximate Solution of the Viscous Sleigh

Unlike for the classical Chaplygin sleigh, the equations of motion for the viscous sleigh with forcing are not integrable through analytical techniques. However the periodic input, periodic output structure of the system allows us to use the harmonic balance method in combination the a nonlinear systems solver to predict the limit cycle dynamics for any given forcing. Following this approach and motivated by the numerical simulation, Fig. 3.1 we will make the ansatz that $u$ and $\omega$ are T-periodic functions The harmonic balance technique assumes the outputs of a system to be sinusoidal and attempts to use the equations of motion to predict the limiting trajectory. From the

12

simulations we see that only harmonics up to the second order appear in the velocities. We use this as motivation to to neglect periodic terms with frequency greater than $2\Omega$. Suppose that $u$ and $\omega$ are of the form

$$u = u_c + a_1 \sin \Omega t + a_2 \cos \Omega t + A_u \sin 2\Omega t + B_u \cos 2\Omega t$$

$$\omega = A_w \sin \Omega t + B_w \cos \Omega t + b_3 \sin 2\Omega t + b_4 \cos 2\Omega t.$$

The angular velocity will assumed to periodic with zero mean, since numerical simulations such as those shown in Fig. 3.1 (e) indicate that limit cycles in the velocity space are symmetric about $\omega$ axis. The assumed form of $u$ and $\omega$ will be substituted into (5.5) and (5.7). In applying the harmonic balance approach we will substitute our assumed solutions into the equations of motion and equate coefficients on both sides. Consider $\dot{u}$, substituting the assumed periodic form into (5.5) and (5.7),

$$\dot{u} = b_1^2 bm + b_2^2 bm - 2cu_c - \frac{c}{m}(a_1 \sin \Omega t + a_2 \cos \Omega t)$$

$$+ (2b_1 b_2 b - 2A_u c) \sin 2\Omega t$$

$$+ (-b_1^2 bm + b_2^2 bm - 2B_u c) \cos 2\Omega t...$$

A direct differentiation of the assumed periodic form of $u$ yields

$$\dot{u} = -\Omega a_2 \sin \Omega t + \Omega a_1 \cos \Omega t$$

$$- 2\Omega A_u \sin 2\Omega t + 2\Omega A_w \cos 2\Omega t$$

Equating coefficients of $\sin \Omega t$ and $\cos \Omega t$ we get

$$-\Omega a_2 = -\frac{c}{m}a_1, \quad \Omega a_1 = -\frac{c}{m}a_2$$

which is only satisfied if $a_1 = a_2 = 0$. Substituting the assumed periodic form of $\omega$ and $u$ into the right hand side of (5.7),

13

$$\dot{\omega} = \frac{(-a_3 b_2 bm + b_1 a_4 bm - 2a_3 bmu_c + 2A)}{mb^2 + I} \sin(\Omega t)$$
$$+ \frac{(-a_3 b_1 bm - a_4 b_2 bm - 2b_2 bmu_c)}{mb^2 + I} \cos(\Omega t)... \tag{3.3}$$

The interesting thing to note is that no second order harmonics appear in the (3.3). By equating coefficients of $\sin(2\Omega t)$ and $\cos(2\Omega t)$ with the derivative of our assumed $\omega$ we get simply

$$-2\Omega b_3 = 0, \quad 2\Omega b_4 = 0$$

or $b_3 = b_4 = 0$. Therefore the velocity $u$ has only second harmonics while the angular velocity, $\omega$ has only first harmonic,

$$u = u_c + A_u \sin(2\Omega t) + B_u \cos(2\Omega t) \tag{3.4}$$

$$\omega = A_w \sin(\Omega t) + B_w \cos(\Omega t). \tag{3.5}$$

In order for this solution to exist it must satisfy (5.5)-(5.7). Substituting (4.5) and (4.6) into (5.5)-(5.7) and simplifying,

$$\dot{u} = A_w^2 bm + B_w^2 bm - 2cu_c + (2A_w B_w b - 2A_u c) \sin(2\Omega t)$$
$$+ (-A_w^2 bm + B_w^2 bm - 2B_u c) \cos(2\Omega t)...$$
$$\dot{\omega} = \frac{(-A_u B_w bm + A_w B_u bm - 2A_w bmu_c + 2A)}{mb^2 + I} \sin(\Omega t)$$
$$+ \frac{(-A_u A_w bm - B_u B_w bm - 2B_w bmu_c)}{mb^2 +} \cos(\Omega t)...$$

The higher harmonics are neglected as part of the harmonic balance method. We will later justify this assumption with numerical results. A direct differentiation of (4.5) and (4.6) gives

14

$$\dot{u} = -2\Omega B_u \sin(2\Omega t) + 2\Omega A_u \cos(2\Omega t)$$

$$\dot{\omega} = -\Omega B_w \sin(\Omega t) + \Omega A_w \cos(\Omega t).$$

To determine $u_c$ and the coefficients $A_u$, $B_u$, $A_w$ and $B_w$ we simply equate the coefficients of the above two systems. This yields the following system of nonlinear equations

$$0 = A_w^2 bm + B_w^2 bm - 2cu_c \tag{3.6a}$$

$$-4m\Omega B_u = 2A_w B_w bm - 2A_u c \tag{3.6b}$$

$$4m\Omega A_u = -A_w^2 bm + B_w^2 bm - 2B_u c \tag{3.6c}$$

$$-2\alpha\Omega B_w = -A_u B_w bm + A_w B_u bm - 2A_w bmu_c + 2A \tag{3.6d}$$

$$2\alpha\Omega A_w = -A_u A_w bm - B_u B_w bm - 2B_w bmu_c. \tag{3.6e}$$

where we denote $\alpha = mb^2 + I$ to keep the notation compact. We employ the Newton-Raphson method to solve the equations (3.6) numerically.

To illustrate the calculation of the coefficients, we choose the sleigh parameters and the input, $\tau$ to be the same as the parameters for the simulation in Fig. 3.1. Performing the calculations yields $u_c = 0.6341$, $A_u = 0.1103$, $B_u = 0.1071$, $A_w = 0.2069$ and $B_w = -0.7689$ after just 4 iterations of the Newton-Raphson method. To compare this solution with the numerical simulation we may define $C_u = \sqrt{A_u^2 + B_u^2}$ and $C_w = \sqrt{A_w^2 + B_w^2}$, which are the amplitudes of $u$ and $\omega$ respectively. In a similar manner we will define $C_u^*$ and $C_w^*$ to be the amplitude of $u$ and $\omega$ on the limit cycle in the numerical simulation. This allows us to define the error between the limit cycle solution obtained through the harmonic balance method and the limit cycle solution obtained through a numerical simulation,

$$e = \sqrt{(u_c - u_c^*)^2 + (C_u - C_u^*)^2 + (C_w - C_w^*)^2} \tag{3.7}$$

The error was found to be $e = 8.6e - 3$ which is two orders of magnitude smaller than the values of the coefficient $(u_c, A_u, B_u, A_w, B_w)$. In Fig. 3.1 we can see further agreement between the analytical solution of the limit cycle and one obtained through direct numerics. The dotted graph shows a

15

trajectory with generic initial values of $(u, \omega)$ converging to the analytically predicted limit cycle (solid line).

## 3.2   Effect of forcing amplitude and frequency on motion

The motion of sleigh due to changes the amplitude and frequency of oscillation of the rotor, shows a rich variety of dynamics. The effect on the average longitudinal velocity, $u_0$, of the knife edge and hence the average velocity, $v_{net}$ of the sleigh due to the variations in the forcing amplitude, $A$ and the frequency $\Omega$ are shown in Fig. 3.2.
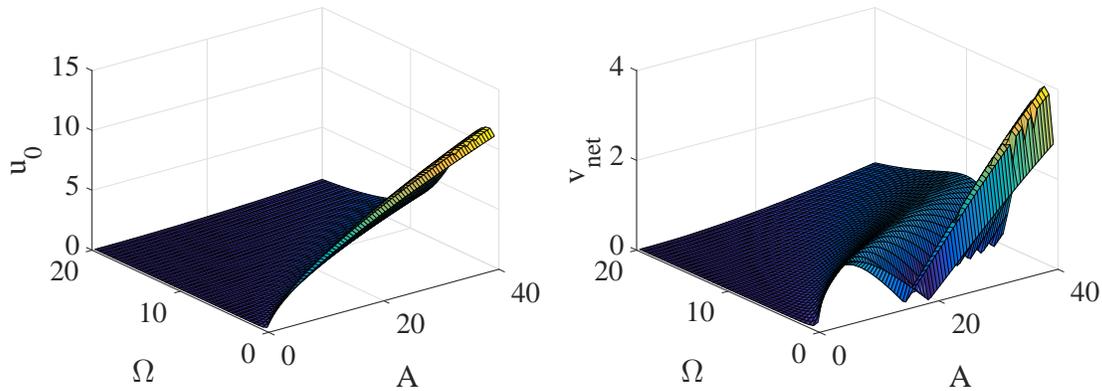


Figure 3.2: Velocity of the sleigh for different inputs. a) shows $u_0$ and b) shows $v_{net}$ for amplitudes of up to 40 and values of $\Omega$ up to 20.

The average longitudinal velocity of the wheel $u_0$ only increases with amplitude and shows little variation with respect to the forcing frequency $\Omega$ at low amplitudes. This means that the instantaneous speed of the sleigh along its path is higher for higher amplitude input. The average velocity of the sleigh in the plane $v_{net}$ appears to reach a local maximum and then decrease to zero before increasing again for higher amplitudes. Figure 3.4 shows a plot of $u_0$ and $v_{net}$ for a fixed $\Omega$ and a large range of amplitudes. We note that although $u_0$ monotonically increases with $A$, $v_{net}$ can decrease or increase touching $v_{net} = 0$ at discrete points. This results in a closed trajectory in the $(x, y)$ plane. Two such trajectories are shown in Fig. 3.3.

Figure 3.5 shows the transitions in steady paths of the sleigh in $x - y$ plane as $A$ increases. These are the paths of the sleigh when the velocities $u$ and $\omega$ are on or very close to the limit cycle in the reduced velocity space. The net displacement of the sleigh in a time period $T$ shrinks, with the path curving back onto itself, as illustrated in the paths for $A = 5$ and $A = 10$. As $A$ increases

further, path of the sleigh forms a closed loop at $A \approx 16.82$. This is when $v_{net}$ converges to zero for the first time. As $A$ increases further, $v_{net}$ becomes nonzero again and the figure eight path breaks open to produce a net displacement, as shown for $A = 20$. Larger values of $A$ lead to the path increasingly close onto itself, eventually leading to a closed path as shown in fig. 3.5.
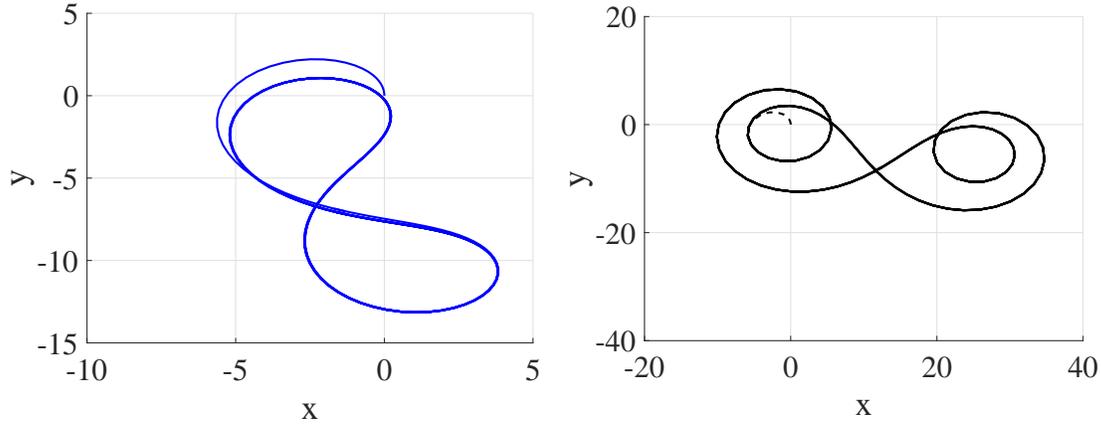


Figure 3.3: Simulations of the chaplygin sleigh executing a closed trajectory in the $(x, y)$ plane. Input parameters are $\Omega = 1$ and (a) $A = 16.82$, (b) $A = 175.4$.
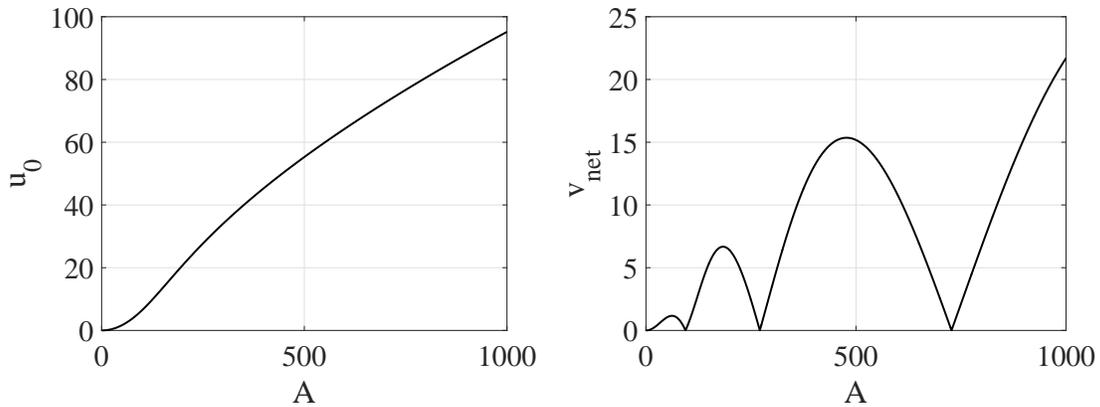


Figure 3.4: Velocity of the sleigh for different amplitudes. a) shows $u_0$ and b) shows $v_{net}$ for amplitudes of up to 1000 with $\Omega$ set to 15.5.

## 3.3 Hybrid Control of the Chaplygin Sleigh

The approximate solution to the limit cycle shows that the average angular velocity of the sleigh converges to zero, i.e. the change in the heading angle of the sleigh during one time period
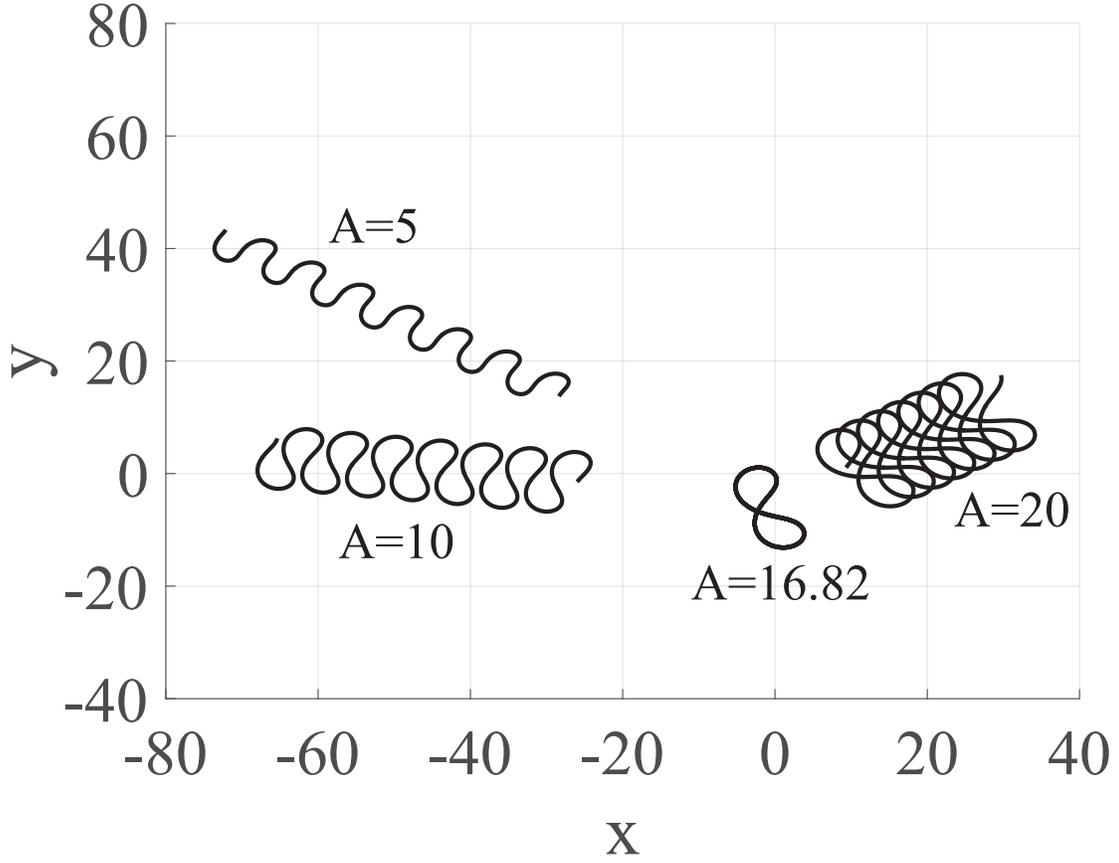
Figure 3.5: Trajectories of the sleigh for four different values of $A$ with $\Omega = 1$. Each starts with $(u, \omega) = (0, 0)$. Each trajectory is shown for $t > 4T$ allowing for the velocities $u$ and $\omega$ to converge to the limit cycle. The trajectories for the transient phase are not shown.

$T = \frac{2\pi}{\Omega}$ is

$$\Delta\theta = \int_0^T \omega \, dt = \int_0^T (A_w \sin \Omega t + B_w \cos \Omega t) dt = 0. \tag{3.8}$$

The average longitudinal velocity of the sleigh $u_0$ is in general non zero. This is also borne out in the simulated trajectories of the sleigh in Fig. 3.1(a). On the velocity limit cycle, the average velocity of the sleigh can be defined as

$$\overline{\mathbf{v}} = \frac{1}{T} \int_{t_1}^{t_1+T} (\dot{x}\hat{i} + \dot{y}\hat{j}) dt \tag{3.9}$$

Since the average heading angle converges to a constant value, for the purpose of computing the average speed, one can assume that the average heading angle is $\overline{\theta} = 0$, i.e., $\frac{1}{T} \int_{t_1}^{t_1+T} \dot{y} \, dt = 0$. The

18

average speed of the sleigh is then

$$\bar{v} = \frac{1}{T} \int_{t_1}^{t_1+T} \dot{x} dt = \frac{1}{T} \int_{t_1}^{t_1+T} (u_x \cos\theta - \omega b \sin\theta) dt \tag{3.10}$$

where it should be noted that $\frac{1}{T} \int_{t_1}^{t_1+T} \omega b \sin\theta dt = 0$.

Suppose the reference average speed of the sleigh is $\bar{v}_r$. The amplitude of the applied torque, $\tau = A \sin\Omega t$, can be be used as the control input to track this reference speed. In Fig. 3.4 (b) we see that many such velocities are possible for a fixed input frequency. The maximum speed possible before inefficient motion is $\bar{v} \approx 1$ for the sample parameters in Fig. 3.2. We now treat the amplitude $A$ required to achieve $\bar{v}_r$ as an unknown. In this case (3.6a)-(3.6e) together with (3.10) (evaluated at $\bar{v} = \bar{v}_r$) form six equations in the six unknowns, $(A_w, B_w, A_u, B_u, u_0, A)$. These unknowns can be found using a numerical algorithm like the Newton-Raphson method.

When the solution to (5.5) and (5.7) converge to the limit cycle, the average heading angle of the sleigh converges to a constant value, as shown in Fig. 3.1 (c) and Fig. 3.1 (d). In order to control the average heading angle to some desired angle $\theta_r$ it is intuitive to consider an additional term in the torque input that is proportional to the error in average heading angle, i.e.

$$\tau_I = -K_I \int_{t-T}^{t} (\theta(t) - \theta_r) dt. \tag{3.11}$$

Numerical simulations for a large range of sleigh parameters, reference angles and average velocities of the sleigh show that an input torque of the form

$$\tau = A \sin\Omega t + \tau_I \tag{3.12}$$

allows simultaneous control of the average speed of the sleigh and its heading. The first term $A \sin(\Omega t)$ allows the sleigh to track reference average speed and the second term $\tau_I$ allows the sleigh to track a desired average angle.

The utility of the hybrid control law is shown in Fig. 4.2 where we see the sleigh execute a turn after tracking a zero reference angle while also tracking $v_{net} = 0.2$. The sleigh's average heading angle first converges towards zero and then to $90^o$ (Fig. 4.2(d)) while its average speed tracks the reference value (Fig. 4.2(b)). The sleigh's angular velocity converges to the limit cycle, then experience a perturbation away from the limit cycle when the torque $\tau_I$ is added to the input

19

and converge back to the limit cycle as $\tau_I$ converges to zero, see 4.2(c). The control input for executing this maneuver is such that $\tau_I$ is much smaller in magnitude than $A$ as shown in Figs. 4.2(e) and (f).

$$\tau_I \to 0 \quad \Longleftrightarrow \quad \frac{\int_{t-T}^{t} \theta(t)dt}{T} \to \theta_r.$$

The average heading angle approaches the desired average heading angle.
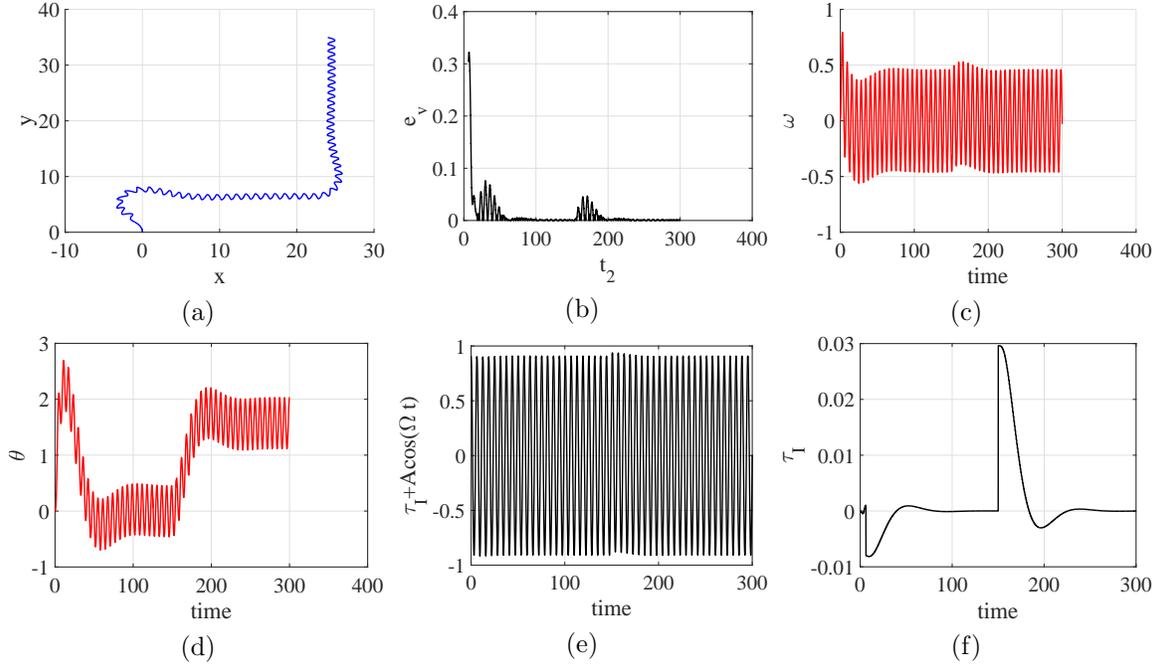


Figure 3.6: Required input for simulation with $\theta_r = 0$. Input due to integral control is shown in (a) and total input in (b).

## 3.4 Chaplygin Sleigh as a Surrogate Model for a Swimming Joukowsli Foil

The dynamics of the swimming Joukowski foil are described by a high dimensional dynamical system. However the dynamics of the system are confined to a low dimensional attractor that is topologically similar to the attractor of the velocity equations of the Chaplygin sleigh. The existence of such a low dimensional attractor allows the Chaplygin sleigh to serve as a surrogate model for the swimming Joukowski foil. We use the harmonic balance equations to define such a reduced order surrogate model of the foil. The Chaplygin sleigh with a no slip constraint will be used as the

20

surrogate model as opposed to the sleigh with an affine constraint, even though the unsteady Kutta condition could impose a small periodic affine constraint. As observed in [67] the limit cycles for both the types of sleigh are nearly identical when the prescribed slip velocity is small in magnitude. The analytical approximation of the limit cycles are, however, easier to compute if the surrogate model is the Chaplygin sleigh with the homogeneous constraint.

A surrogate model for the swimming foil is constructed by first finding the amplitudes $(A_x, B_x, A_w, A_w)$ of the harmonics of the limit cycle solution as well as the velocity constant $u_c$ from (4.5) and (4.6). With an approximate solution for the foil limit cycle known, the remaining problem is to determine the parameters of a Chaplygin sleigh that produce a limit cycle with the same solution. This requires the solution to an inverse problem where the parameters $(m, b, c, \alpha = I + mb^2)$ are the unknowns and the parameters $(A_x, B_x, A_w, A_w, u_c)$ in (3.6) are known. The parameters $(A_x, B_x, A_w, A_w, u_c)$ are determined from the foil simulations by first assigning the cosine $(A)$ amplitudes based on the foil velocities at the beginning of one input period. Next an initial sine $(B)$ amplitude is assigned and the error is summed between the estimated velocities and the simulation data for one complete time period. The $(B)$ values are updated based on the error from the previous iteration and the process is repeated until the errors converge. The same iterative process is then repeated to determine the $u_c$ value. This leaves the system of equations (3.6) overdetermined with five equations and four unknowns.

The overdetermined system of equations can be approximately solved through a constrained least squares method, the constraint being that all the four unknowns $(m, b, c, \alpha)$ should be non negative,

$$
\begin{aligned}
&\min_x \frac{1}{2}||\mathbf{C}\vec{x} - \vec{d}||_2^2 \\
&s.t. \quad \mathbf{A}\vec{x} \leq \vec{b}
\end{aligned}
\tag{3.13}
$$

where

$$\mathbf{C} = \begin{bmatrix} A_w^2 + B_w^2 & 0 & -2u_c & 0 \\ B_w^2 - A_w^2 & -4\Omega A_x & -2B_x & 0 \\ A_w B_w & 2B_x\Omega & -A_x & 0 \\ A_x A_w + B_x B_w + 2u_c B_w & 0 & 0 & 2\Omega A_w \\ B_x A_w - A_x B_w - 2u_c A_w & 0 & 0 & 2\Omega B_w \end{bmatrix},$$

$$\vec{x} = \begin{bmatrix} \delta \\ m \\ c \\ \alpha \end{bmatrix}, \vec{d} = \begin{bmatrix} 0 \\ 0 \\ 0 \\ 2A \\ 0 \end{bmatrix}, \mathbf{A} = -\mathbf{I}_{4\times 4}, \vec{b} = \begin{bmatrix} 0 \\ 0 \\ 0 \\ 0 \end{bmatrix}.$$

We used MATLAB's *lsqlin* function to perform this calculation. As an example, using the limit cycle parameters $A_x = 0.001779$, $B_x = -0.000932$, $A_w = 0.115531$, $B_w = 0.699560$, and $u_c = 0.434879$ the least squares computation yielded the following surrogate sleigh parameters $m = 401.2119$, $b = 0.0959$, $c = 22.3925$, $\alpha = 0.4450$. These parameters were plugged into the sleigh equations (5.5)-(5.7) to simulate the dynamics of the surrogate sleigh. The solution of (5.5)-(5.7) is shown in (red) fig. 3.7(a). For comparison the same trajectory for the swimming foil is shown in red. As the sleigh and foil approach their steady state speeds the figure 8 limit cycles emerge. The trajectories of both the systems converge to limit cycles that are nearly identical. The limit cycles themselves, obtained from the simulations are shown in fig. 3.7(b).
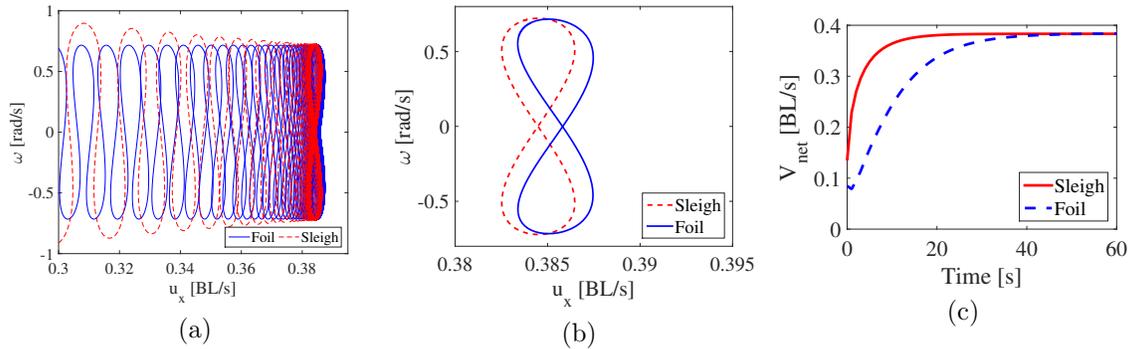


Figure 3.7: (a) Foil and sleigh velocities as they converge to their respective limit cycles. (b) Foil and sleigh limit cycles. (c) The average velocities of the foil and the equivalent sleigh converge to nearly the same value.

22

It should be noted from fig. 3.7(a) that the transient trajectories of the foil do not match those of the sleigh very well. This is expected since only dynamics on the limit cycles have been modeled and matched with each other.

Beyond a qualitative match of the limit cycles, the average speeds of the sleigh and foil can be used as a quantitative measure of the accuracy of the sleigh as a surrogate model for the swimming foil. Their average speeds, $\overline{v}$, calculated using (3.10) are shown in fig. 3.7(c). In fig. 3.7(c) the blue dashed line is the average velocity for the foil, while the red solid line is the average velocity of the equivalent sleigh given the same periodic input. It is obvious that the transient dynamics of the two systems differ but both the foil and the sleigh's average speeds converge to nearly the same value, with the difference in the two being $\approx 0.0006 \quad [BL/s]$ or $\approx 0.18\%$. The small error arises due to the least squares approximation of the sleigh model, (3.13). The closeness of the average speeds is also seen in fig. 3.7(b). The point of intersection of the two branches of the limit cycle which also lies on the horizontal axis is the average speed. This is very close in magnitude for both the limit cycles shown in fig. 3.7(b).

Here we remark once again that while Kutta condition could lead to an affine nonholonomic constraint, the limit cycle of the foil's dynamics are close to that of the Chaplygin sleigh with a homogeneous nonholonomic constraint. Since it was shown that the limit cycle of the sleigh with an affine periodic constraint is nearly the same, it implies that the limit cycle of the foil's dynamics is close to that of the sleigh with an affine periodic constraint.

## 3.5 Turning Control

The utility of having a low dimensional Chaplygin sleigh surrogate model for the swimming foil is that it can prove useful in controlling the dynamics of the swimming foil. Determining the control input that produces the desired motion and path of the swimming foil is greatly simplified by the very low dimensional equivalent sleigh model. Essentially a control input is designed to steer the surrogate Chaplygin sleigh with prescribed average speed. Such an input is given by (3.12). The same control input is then applied to the swimming foil.

This control via the surrogate Chaplygin sleigh is demonstrated through a numerical simulation of the turning maneuver of the foil. The foil first starts from rest and tracks an average speed of $\overline{\mathbf{v}} = 0.385$ body lengths per second and an average heading angle $\theta = 0$. It is then re-

23

quired to make a 90 degree turn while tracking the same speed. The necessary control inputs for the turning maneuver are the amplitude and frequency of oscillations of the applied torque via the internal reaction wheel. One can freely choose a frequency and determine the necessary amplitude of the torque to accomplish the prescribed maneuver. The frequency of the control torque is chosen to be the same as in the computations described earlier. The amplitude of the control torque is determined by first obtaining the equivalent sleigh parameters, $(m, b, I, c)$. These parameters of such an equivalent sleigh were computed in the previous section from the numerical simulations of the foil-vortex interactions and using (3.13), where the parameters are determined described in the previous section. Once the equivalent sleigh parameters are determined using (3.13), the control torque (3.12) is applied on the foil to steer it to make a 90 degree turn, while tracking the average speed of $\overline{v} = 0.385$.



(a)

(b)

(c)
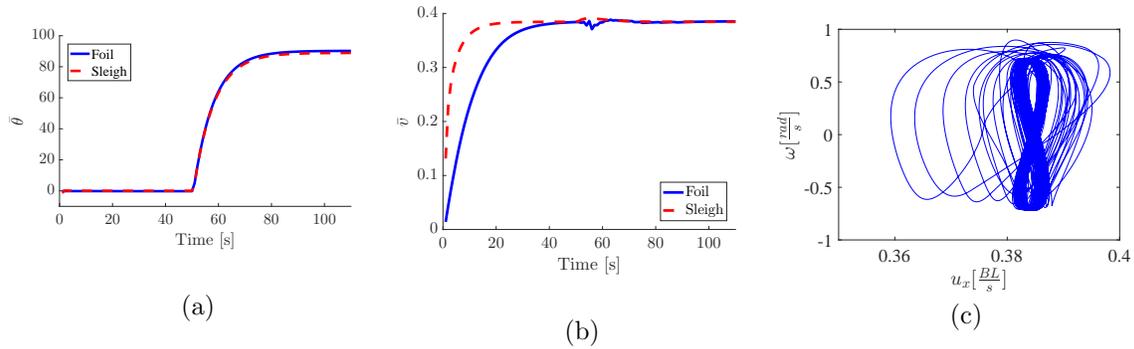
Figure 3.8: Turning maneuver of the foil by 90 degrees while tracking a specified average speed, with control torque computed from the surrogate sleigh model. (a) Average heading angle of the foil (blue solid line) and equivalent sleigh (red dashed line). (b) Average speed of the foil (blue solid line) and equivalent sleigh (red dashed line). (c) The sleigh's velocity and angular velocity undergo a perturbation from the limit cycle during the turn, but converge back to the limit cycle.

The average heading angle from the simulation of the surrogate Chaplygin sleigh and the coupled fluid-foil is shown in Fig. 3.8(a), where the angle $(\overline{\theta})$ is the angular position of the body averaged over one time period of the forcing function. In Fig. 3.8(a) the red dashed line is the average heading angle for the surrogate Chaplygin sleigh while the blue solid line is the average heading angle for the foil with the same torque input. The heading angle is originally 0 degrees with the foil swimming along a horizontal line. The foil begins its turning maneuver at $t = 50$. At about $t = 70$ the difference in the final heading angle of the foil and the sleigh was $\approx 1^o$. The average speed of the foil and the surrogate sleigh are shown in fig. 3.8(b), which converges to the desired speed and deviates only slightly during the turning maneuver. During the turning motion

24

the trajectory of the foil deviates from the limit cycle before converging back to it as shown in fig. 3.8(c). Here we remark that the small differences between the average speed of the surrogate sleigh and the foil during the turning motion seen in fig. 3.8(b) cannot be attributed solely to errors to the numerics. The Chaplygin sleigh is a good surrogate model for the swimming foil, only when the velocities of the two systems are close to their respective limit cycles. During the turning motion, when the trajectories in the velocity space deviate from the limit cycle, differences arise between the dynamics of the two systems.

25

# Chapter 4

# Path Tracking for Underactuated Nonholonomic Robots

In previous work it has been shown that the periodically forced Chaplygin sleigh with frictional dissipation moves along a serpentine trajectory with an average heading angle that is constant [3, 25, 27]. The periodic nature of the solutions allows us to apply the harmonic balance method [30, 66] to find these solutions with high accuracy. In [?, ?, 67] the same method is also extended to control the average velocity of the sleigh along the trajectory while a correction term in the input is shown to simultaneously control the average angle. The angle correction was done by a control term proportional to the average error in the angle for the last time period. In [46] another method is used to control the angle which only relies on knowing the orientation of the sleigh at the current time instant. We use the method in [46] in this paper to control the angle as it is found to have faster convergence in simulations. Unlike in [46], however, we use nonautonomous propulsion which allows us to accurately predict the periodic response. Since tracking both velocity and heading angle are achieved in previous work, the ground has been laid to develop motion planning for the Chaplygin sleigh. In this paper we address the problem of path tracking for the system. In particular we exploit the periodic solutions of the system to control the sleigh along a desired path with some specified average velocity.

Motion planning of nonholonomic systems with sinusoids has been addressed for kinematic systems in works like [54]. In the context of dynamic systems there are also motion planning results

for the snakeboard which take advantage of the geometric properties of the system [18,20]. Optimal control has also been applied to the snakeboard [62], however optimal control is impractical due to the computational intensity of finding optimal trajectories. Stability results can be shown for pure pursuit path tracking of certain nonholonomic vehicles [58]. The analysis in [58], however, is only applicable to autonomous systems. We seek to exploit the predictability of solutions of the Chaplygin sleigh with a prescribed periodic torque to simultaneously control the velocity of sleigh while steering along a path.

For path tracking of the Chaplygin sleigh we employ a vector pursuit algorithm [77]. In pursuit a goal point is chosen to always be some lookahead distance $L$ from the sleigh such that pursuing the point naturally causes the robot to track the path. The two main variants of this method in research and practice are pure pursuit [?] and vector pursuit [43,84]. The only difference between the methods is that vector pursuit takes into account the instantaneous angle of the path at the goal point. For the particular system considered in this Chapter, the eventual trajectory of the sleigh with periodic actuation is always a serpentine curve. The mean of such a curve can track a reference path, and at best the error between only the mean path and the reference path can be expected to converge to zero. We account for this in the control algorithm by assuming the goal point moves in a similar way. In order to prescribe the serpentine motion of the goal point, the orientation of the path near the goal point must be known making the proposed algorithm of vector pursuit type.

The contribution of this Chapter is a motion planning algorithm for the Chaplygin sleigh. The algorithm involves simultaneous tracking of a reference limit cycle in a reduced velocity space and the tracking of a path in the configuration (physical) space. This simultaneous tracking is achieved by combining the calculations of matching the harmonics (the harmonic balance method) and a vector pursuit algorithm. Circular and straight line reference paths are tracked with the torque as the only control input.

## 4.1  Control via Harmonic Balance Method

In this section we present another method of controlling the average heading angle of the sleigh and extend the results of Chapter 3 to the case where the torque has a nonzero mean. The equations of motion of the Chaplygin sleigh with friction are reminded to be

$$\dot{u} = b\omega^2 - \frac{c}{m}u \tag{4.1}$$

$$\dot{\omega} = \frac{-mbu\omega}{I + mb^2} + \frac{\tau}{I + mb^2} \tag{4.2}$$

$$\dot{\theta} = \omega. \tag{4.3}$$

A periodic torque on the sleigh, applied through the periodic rotation of the rotor, can propel the sleigh forward. It was shown in [25, 27, 68, 70] that the solution to (5.5) and (5.7) when $\tau = A\cos\Omega t$ is a limit cycle shaped as a figure eight in the reduced velocity space. The existence of limit cycle solutions was proven in [3] using the Brouwer fixed point theorem for the associated Poincare map. An analytical approximation to this limit cycle was constructed in [?] and it was shown that tracking a reference average speed was equivalent to generating a desired limit cycle in the reduced velocity space which was accomplished by computing the required periodic torque. The limit cycle in the reduced velocity space produces a serpentine path in the configuration space.

We extend this method of tracking limit cycles in the reduced velocity space to simultaneously track a reference average velocity and a reference path in the configuration space. The assumed control input is a sum of three inputs of the form

$$\tau = \tau_0 + A\cos(\Omega t) + K\sin(\theta - \theta_r). \tag{4.4}$$

We may still find the solution due to the above torque using harmonic balance method. The constant torque $\tau_0$ is largely responsible for steering the sleigh at a constant rate along circular arcs. The torque $K\sin(\theta - \theta_r)$ is similar to a proportional controller for tracking a reference angle $\theta_r$ as was shown in [46]. This term produces faster convergence to a reference heading than the averaging used in [25].

We make the ansatz that the solution to (5.5)-(4.3) due to the torque (4.4) is a sum of harmonics of the form

$$u = u_0 + A_{u1}\sin(\Omega t) + B_{u1}\cos(\Omega t)$$

$$+ A_{u2}\sin(2\Omega t) + B_{u2}\cos(2\Omega t) \tag{4.5}$$

$$\omega = \omega_0 + A_{w1}\sin(\Omega t) + B_{w1}\cos(\Omega t)$$

$$+ A_{w2}\sin(2\Omega t) + B_{w2}\cos(2\Omega t). \tag{4.6}$$

Therefore the solution to (4.3) should follow

$$\begin{aligned}
\theta(t) - \theta(0) = \int_0^t \omega(\tau)d\tau = \omega_0 t &- \frac{A_{w1}}{\Omega}\cos(\Omega t) \\
&+ \frac{B_{w1}}{\Omega}\sin(\Omega t) - \frac{A_{w2}}{2\Omega}\cos(2\Omega t) \\
&+ \frac{B_{w2}}{2\Omega}\sin(2\Omega t) + \frac{-2A_{w1} - A_{w2}}{2\Omega}.
\end{aligned} \tag{4.7}$$

The average velocity of the sleigh in one time period of the periodic component of the torque is

$$\bar{v} = \frac{1}{T}\sqrt{\left(\int_{t_2}^{t_2+T}\dot{x}dt\right)^2 + \left(\int_{t_2}^{t_2+T}\dot{y}dt\right)^2} \tag{4.8}$$

where $\dot{x}$ and $\dot{y}$ can be expressed using the reduced velocities and $\theta$. If the sleigh traverses a circular path on the average, then the radius of the circular path is $R = \frac{\bar{v}}{\omega_0}$.

The torque term $K\sin(\theta - \theta_r)$ is expanded to the third order as

$$\sin(\theta - \theta_r) \approx (\theta - \theta_r) - \frac{(\theta - \theta_r)^3}{6}.$$

This third order expansion allows for the term to be accounted for in the harmonic balance method by rewriting it as a sum of sine and cosine functions.

Two specific types of reference paths will be considered in this paper : a straight line and a circle and in each case a reference average velocity will also be tracked. The assumed solutions (4.5) and (4.6) can be substituted into the reduced equations (5.5)-(5.7) and a reference average speed given by (4.8). The corresponding harmonics on each side of the equations can then be matched. This leads to a system of 11 nonlinear equations with 11 unknowns ($u_0$, $A_{u1}$, $B_{u1}$, $A_{u2}$, $B_{u2}$, $A_{w1}$, $B_{w1}$, $A_{w2}$,

29

$B_{w2}, \tau_0, A)$. Since the equations are nonlinear we use Newton's method to solve them numerically to calculate the input required to produce the desired motion. In the absence of $\tau_0$ the average motion is along a straight line and $\omega_0$ will be zero.

The reference angle $\theta_r$ is of course known in the preceding calculations. This reference angle will be the means of steering the sleigh for the path tracking algorithm.

### 4.1.1 Path Tracking

The schematic Fig. 4.1 shows the geometric setup of vector pursuit in a plane.
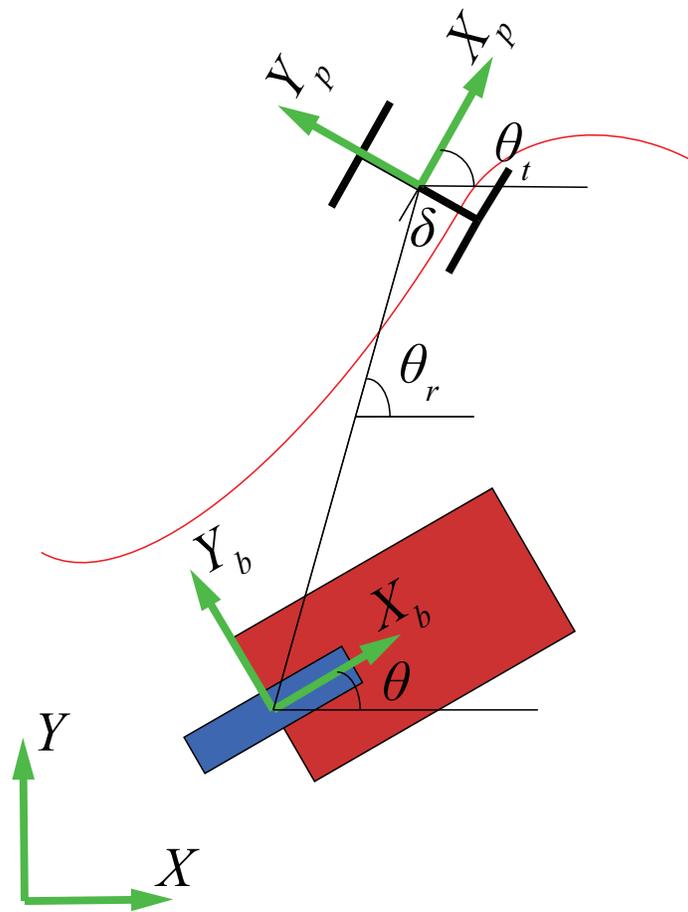


Figure 4.1: Diagram of the path and goal point. The $X_p - Y_p$ coordinate system is such that the $X_p$ axis is tangent to the path point closest to the goal point. The red line represents a sample path and $\delta$ is the lateral offset to account for serpentine motion of the sleigh.

To calculate the reference angle required for the sleigh to track the path we employ a vector

pursuit path tracking problem. First we define the coordinates and orientation of the path at the goal point to be $(x_t, y_t, \theta_t)$. The goal point is defined to be one look ahead distance $L$ from the sleigh at any given time. The desired reference angle is then

$$\theta_r = sign(y_t - (y - b\sin(\theta)))\cos^{-1}\left(\frac{x_t - (x - b\cos(\theta))}{L}\right)$$

which is the angle of the line connecting point $P$ of the sleigh to the goal point as shown in Fig. 4.1.

Note that if the goal point is always on the path, the serpentine motion of the sleigh will cause oscillations in the reference angle. Such oscillations are undesirable as the harmonic balance assumes the reference angle to be either constant or linearly increasing and the harmonic balance solutions would not be valid when the reference angle is oscillating. In order to take this into account we require that the goal point executes serpentine motion around the path similar to the sleigh. This ensures that in the ideal case when the sleigh is following the path, $\theta_r$ remains constant or linearly increasing as necessary.

Serpentine motion of the target can be prescribed by assuming ideal limit cycle motion for the target. We define $\delta(t)$ to be the signed distance between the sleigh and its average path for $t \in [0, T]$ where $T = 2\pi/\Omega$ is the time period. The goal point is then calculated using the following procedure

1. Find the point on the path closest to the sleigh

2. Beginning from this point search along the path for the first point that is a distance $L$ from the sleigh

3. Find the point $\delta(mod(t, 2\pi))$ away from the above path point along the $Y_p$ direction as shown in Figure 4.1 and set this to be the goal point

## 4.2   Simulation

The effectiveness of the path tracking algorithm was tested with numerical simulations. In this section we show the sleigh's ability to track both linear and circular paths using the proposed algorithm. In each case we specify a velocity of $\bar{v}_d = 0.2$ and for the circle we chose a radius of

31

$R = 10$. We define the normalized error in the velocity of the sleigh to be

$$e_v = \frac{\bar{v} - \bar{v}_d}{\bar{v}_d}$$

Figure 4.2 demonstrates the convergence of the proposed control law for a set of parameters. For the straight line trajectory the initial conditions are some distance away from the from the path to show convergence to the path. In Figure 4.2 (a) we see that the sleigh is able to recover and track a straight line path. In Figure 4.2 (b) we see that as the sleigh converges to the desired path, the velocity also converges to the desired velocity as the normalized error goes to zero. From Figure 4.2 (c) we see that convergence to the specified limit cycle is excellent. The sleigh is also able to track a circular path as shown in Figure 4.2 (d). Convergence to the desired path is not as good as for the linear motion due to the fact that the goal point is always some distance away from the sleigh. However in Figure 4.2 (e) we see that convergence to the desired velocity is also achieved for motion of nonzero curvature. The dots in Figure 4.2 (e) are due to the chord length only being checked
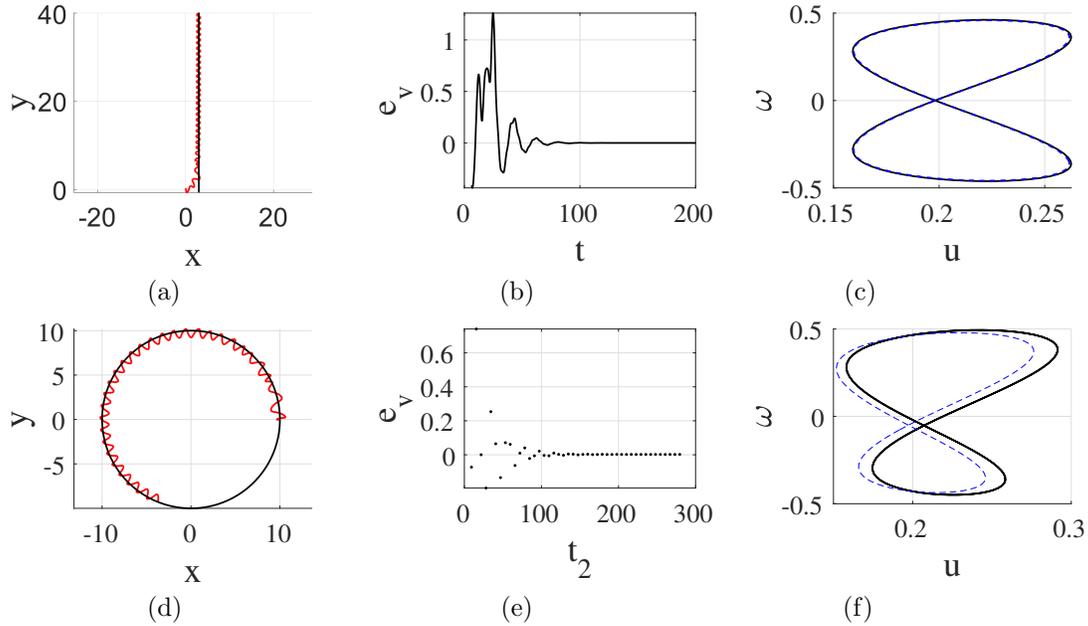


Figure 4.2: Simulation of sleigh tracking the line $x = 3$ (top row) and circle of radius $R = 10$ (bottom row). The velocity specified in each simulation is $\bar{v}_d = 0.2$. Figures (a) and (d) are the path of the sleigh in the $(x, y)$ plane where the black line shows the reference path. Figures (b) and (e) the error in $\bar{v}$ and figures (c) and (f) the limit cycle in the reduced velocity space where the desired limit cycle is shown as a blue dashed line. The parameters are $m = 1$, $b = 1$, $I = 1$, $c = 1$, $K = -1$, $L = 2$ for motion on a line and $L = 1.5$ for motion on a circle.

when the sleigh crosses its average path. In Figure 4.2 (f) we see that there is more error between the limit cycle seen in simulation and calculated by the harmonic balance method. This error is likely due to the increased number of equations to be solved for the circular motion and due to the target being some distance away causing the sleigh to track a circle of slightly smaller radius.

Figures 4.3 (a) and (b) show the convergence of the solution of the reduced velocity equations (5.5) and (5.7) to the reference limit cycles for the case of tracking a straight line and a circle respectively. From Figures 4.3 (b) and 4.3 (d) we see that the input is bounded and continuous throughout the motion and eventually converges to a periodic solution. In the case of the straight



(c)                    (d)

(c)                    (d)
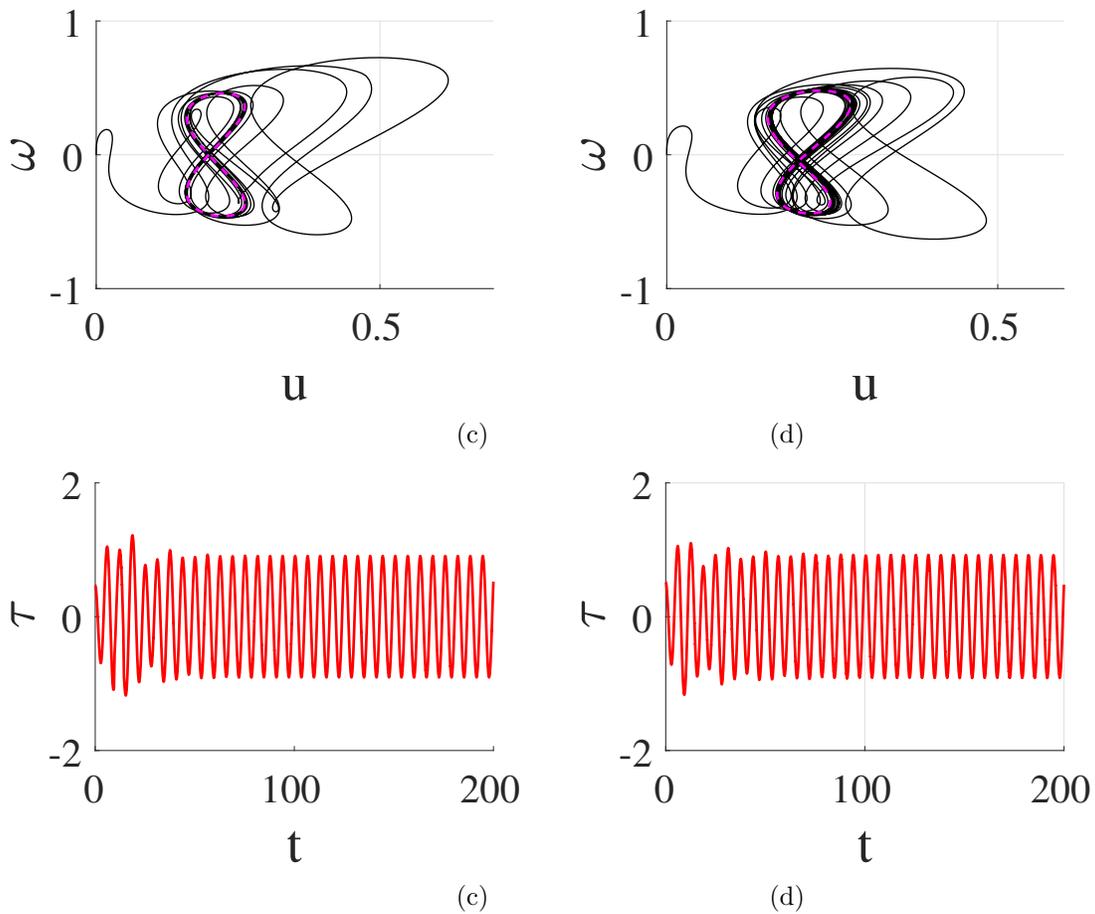
Figure 4.3: Convergence to specified limit cycles and input for the line (top) and circle (bottom) simulations. The subfigures are (a,c) the limit cycle in the $(u, \omega)$ space where the desired limit cycle is shown as a magenta dashed line and (b,d) the torque input for each motion. The parameters are $m = 1$, $b = 1$, $I = 1$, $c = 1$, $K = -1$, $L = 2$ for motion on a line and $L = 1.5$ for motion on a circle.

line motion the steady state solution is

$$\tau = A\cos(\Omega t) + K\sin(\theta(t) - \frac{\pi}{2})$$

and for the circular motion it's

$$\tau = \tau_0 + A\cos(\Omega t) + K\sin(\theta(t) - \omega_0 t)$$

where $\tau_0$, $A$ and $\theta(t)$ are known from the harmonic balance calculation

Periodic forcing is one of the most common methods used to control nonholonomic systems. In literature there is a lot of work addressing the motion planning of kinematic nonholonomic systems using periodic inputs [54]. Gait generation for low dimensional dynamic systems has been addressed in [75]. There are also motion planning results for the snakeboard which take advantage of the geometric properties of the system [18, 20]. In this paper harmonic balance method is shown to accurately predict and control the velocity of the sleigh by exploiting the periodic nature of the solutions. The sleigh can be simultaneously steered via feedback using the same input of a torque on the sleigh. Control of the velocity and heading of the sleigh is used to generate path tracking with velocity control. This work introduces a novel method of motion planning for highly underactuated dynamic nonholonomic systems.

34

# Chapter 5

# Chaotic Dynamics of a Chaplygin Sleigh Due to Passive Unbalanced Rotor

The first version of the two link Chaplygin sleigh was studied in [17] where it is referred to as the landfish. There, the case of periodic actuation is considered on the frictionless two link sleigh. The problem of controllability of the two link sleigh with friction is addressed in [24]. The free response of the two link sleigh with a small rotor is explored in [22]. We summarize these results here to show how the motion of the Chaplygin sleigh is modified in the presence of a passive internal degree of freedom.

A schematic of the Chaplygin sleigh is shown in Fig. 8.1. The sleigh has a runner or a slender wheel at the rear that contacts the ground at the point $P$. The runner is assumed to able to slide smoothly in its longitudinal direction but not in a transverse direction. The mass of the sleigh is denoted by $m_c$ and the moment of inertia about its center by $I_c$. An internal rotor of mass $m_r$ and moment of inertial $I_r$ are hinged to the center of the sleigh, such that the rotor can rotate freely without any resistance. The configuration of the Chaplygin sleigh is parameterized by the location its the center of mass, $(x, y)$ and its orientation $\theta$, with respect to an inertial frame of reference. The configuration of the internal rotor an be parameterized by the angle $\beta \in S^1$. The configuration space of the system is $Q = SE2 \times S^1$.
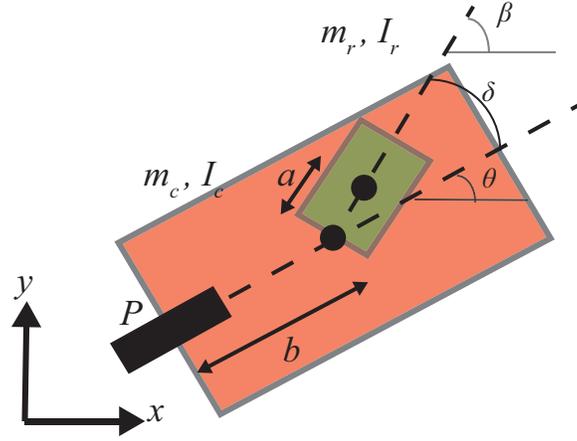
Figure 5.1: The Chaplygin sleigh consists of a sleigh of mass $m_c$ with a rear wheel or a sharp runner at a distance of $b$ from the center of mass. The runner makes contact with the ground at point $P$. An internal rotor of mass $m_r$ is attached to the center of the sleigh. The center of mass of the rotor is at a distance of $a$ from the center of the sleigh.

The Lagrangian for the two link sleigh is given by

$$\mathcal{L} = \frac{1}{2}m(\dot{x}^2 + \dot{y}^2) + m_r a\dot{\beta}(\dot{y}\cos\beta - \dot{x}\sin\beta)$$
$$+ \frac{1}{2}I_c\dot{\theta}^2 + \frac{1}{2}(I_r + m_r a^2)\dot{\beta}^2 \tag{5.1}$$

where $m = m_r + m_c$. By deriving the Euler Lagrange equations and, once again, using a body-fixed velocity we can eliminate $\theta$ yielding the equations of motion as

$$\begin{bmatrix} \mathbf{I} & 0 \\ \mathbf{0} & 1 \end{bmatrix} \begin{bmatrix} \dot{u} \\ \dot{\Omega} \\ \dot{\omega} \\ \dot{\delta} \end{bmatrix} = \begin{bmatrix} m_c b\Omega^2 + m_r a\omega^2 \cos\delta \\ -m_c bu\Omega - m_r ab\omega^2 sin\delta \\ -m_r au\omega\cos\delta \\ \Omega - \omega \end{bmatrix} \tag{5.2}$$

where $\Omega = \dot{\theta}$, $\omega = \dot{\beta}$, $\delta = \theta - \beta$ is the angle made by the internal rotor with respect to the body $X_b$ axis and $\mathbf{I}$ represents the locked inertia tensor,

$$\mathbf{I} = \begin{bmatrix} m & 0 & m_r a\sin\delta \\ 0 & I_c + mb^2 & m_r ab\cos\delta \\ m_r a\sin\delta & m_r ab\cos\delta & I_r + m_r a^2 \end{bmatrix}. \tag{5.3}$$

36

We consider the special case where the mass, moment of inertia and length of the internal rotor are small compared to the corresponding parameters of the sleigh. We choose the small parameter

$$\frac{m_r}{m} = \frac{a}{b} = \epsilon \ll 1. \tag{5.4}$$

The reduced equations of motion are then defined by the dynamical system

$$\dot{u} = \frac{K^4 b\Omega^2 + \epsilon(K^2 - 1)(b\Omega^2 \cos^2 \delta + u\Omega \sin \delta \cos \delta)}{\epsilon(K^2 - 1)\cos^2 \delta + K^4}$$
$$+ \frac{b\omega^2 \epsilon(\epsilon(K^2 - 1) + K^2))\cos \delta}{\epsilon(K^2 - 1)\cos^2 \delta + K^4} \tag{5.5}$$

$$\dot{\Omega} = -\frac{K^2(\epsilon^2 b\omega^2 \sin \delta + u\Omega)}{b(\epsilon(K^2 - 1)\cos^2 \delta + K^4)} \tag{5.6}$$

$$\dot{\omega} = -\frac{(K^2 - 1)\cos(\delta)(\epsilon^2 b\omega^2 \sin \delta + u\Omega)}{\epsilon b(\epsilon(K^2 - 1)\cos^2 \delta + K^4)} \tag{5.7}$$

$$\dot{\delta} = \Omega - \omega \tag{5.8}$$

where $K^2 = 1 + \frac{I_r}{mb^2}$. This is a dynamical system that defines a flow on the manifold $\mathcal{M} = \mathbb{R}^3 \times S^1$. We will denote the flow map of this dynamical system by $\Phi_t^T : \mathcal{M} \mapsto \mathcal{M}$. A discussion of the fixed points of eqs. (5.5)-(5.8) is given in [26] and repeated in the next section. For the purposes of this work it is relevant that there are no stable fixed points for this system. We will demonstrate that the dynamics become chaotic for all parameter values.

## 5.1    Simulation Results

A direct simulation of the equations of motion of the sleigh with an internal rotor shows dramatically different dynamics from those of the classical sleigh. A sample simulation of (5.5), (5.6) and (5.7) for generic initial conditions is shown in Fig. 5.2. The evolution of $u$ and $\Omega$ occurs with two distinct transient stages before convergence to a nearly periodic solution. These transient stages of dynamics are common to any initial condition, with variations in the time periods associated with these individual stages.

In the first transient phase highlighted in Fig. 5.2 (a) and (b) it can be seen that for a short

37
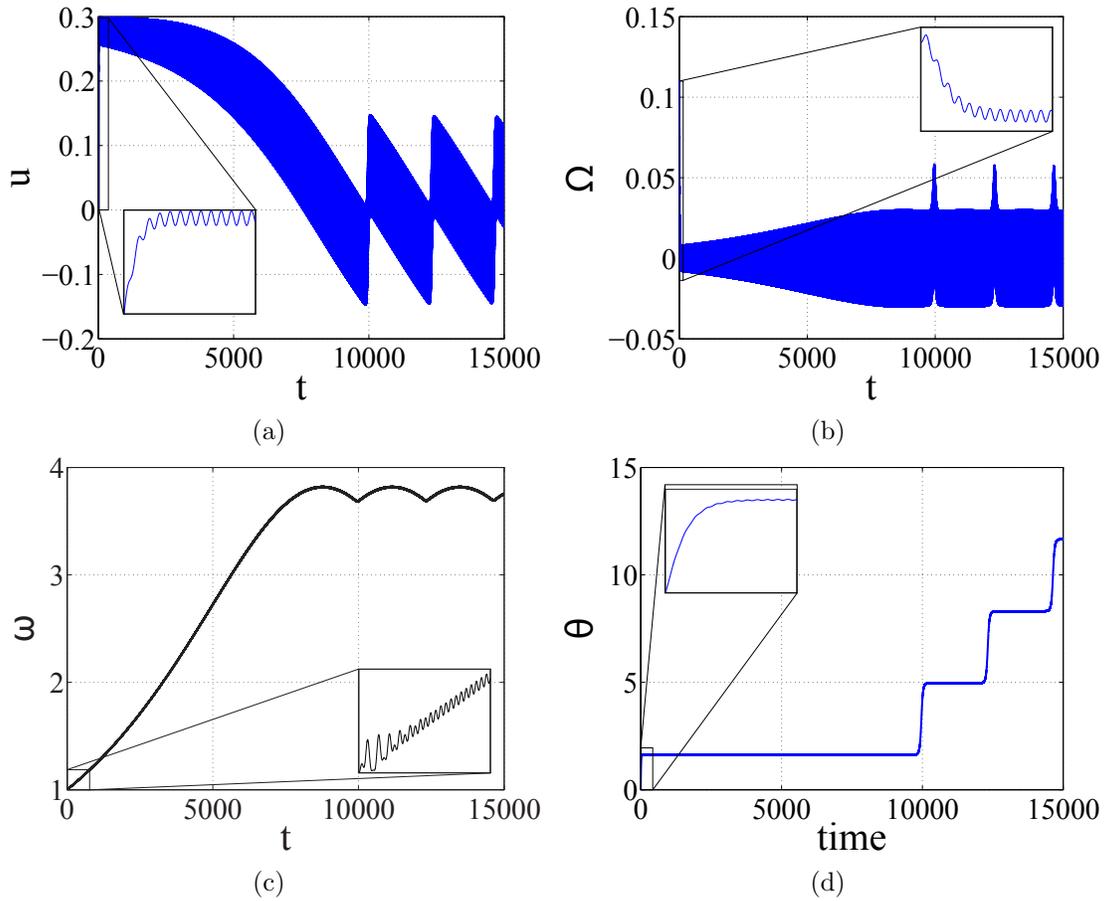
Figure 5.2: Simulation of the Chaplygin sleigh with a small internal rotor with $\epsilon = 0.1$ and initial conditions $u(0) = 0$, $\Omega(0) = 0.1$, $\omega(0) = 1$. Energy is $E = 0.1127$

duration of time ($t < 100$), the dynamics of the sleigh are nearly the same as that of a Chaplygin sleigh without the internal rotor. In this short interval the angular velocity of the sleigh becomes very small and the longitudinal velocity and $u$ reaches a nearly constant value.

In the second transient stage ($100 < t < 8,700$), $u(t)$ decays with oscillations and $\Omega(t)$ oscillates about zero but with an increasing amplitude. The angular velocity of the rotor increases, but with very small amplitude oscillations. At about $t = 8700$ a steady state is reached and as will be discussed later, a trajectory converges to an attractor $\mathcal{A} \subset \mathcal{M}$. From here on the longitudinal velocity of the sleigh has a nearly oscillatory behavior with two frequencies of oscillation. The longitudinal velocity is the sum of two periodic functions, one with a large time period of about 2200 and zero mean and the other a periodic function with a very small time period. The angular

38

velocity of the sleigh oscillates about zero, but with sudden spikes occuring at intervals of about $t = 2200$. The angular velocity of the passive rotor show small oscillations around a non zero mean. The heading angle of the sleigh, $\theta$, is nearly piecewise constant with sudden jumps at time intervals of about 2200.

The transient dynamics of the sleigh and convergence to the attractor follow the same pattern for any initial conditions. Initial conditions of the sleigh with distinct kinetic energies converge to distinct attractors. Conversely all initial conditions with the same kinetic energy converge to a unique attractor. This is shown most clearly in Fig. 5.3 where the angular velocity of the rotor for two sample sets of initial conditions on the same energy level is seen to converge to the same function for all initial conditions with the same energy. Furthermore, the initial transient dynamics are qualitatively the same for all the initial conditions shown in fig.5.3.
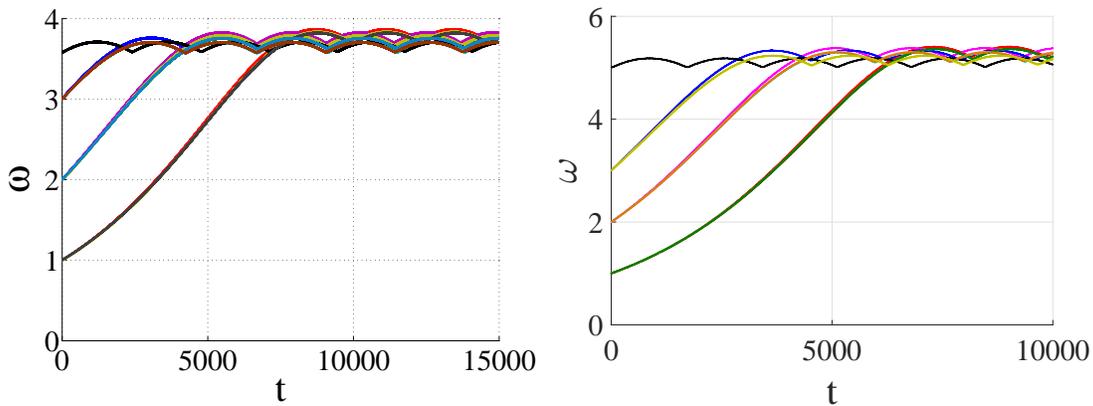


Figure 5.3: Trajectory of the sleigh for different initial conditions on a level set of kinetic energy. (a) $E = 0.1184$ and (b) $E = 0.2313$.

## 5.2    Transient Dynamics of the Sleigh and Regular Perturbation Expansion

The first transient stage of the dynamics of the sleigh can be explained using a regular perturbation analysis of (5.5) - (5.8). Such regular perturbation analysis has been employed for the analysis of other nonholonomic systems such as the twist car, [14, 32, 83]. We expand the states into

a power series in $\epsilon$.

$$u(t) = u_0(t) + \epsilon u_1(t) + \epsilon^2 u_2(t) + ... \tag{5.9}$$

$$\Omega(t) = \Omega_0(t) + \epsilon\Omega_1(t) + \epsilon^2\Omega_2(t) + ...$$

$$\omega(t) = \omega_0(t) + \epsilon\omega_1(t) + \epsilon^2\omega_2(t) + ...$$

$$\delta(t) = \delta_0(t) + \epsilon\delta_1(t) + \epsilon^2\delta_2(t) + ...$$

The right hand side of the preceding equations are expanded in a power series of $\epsilon$. We first note that $K^2 - 1 = O(\epsilon)$. The denominators in each of the right hand side of the equations can then be expanded in a power series in $\epsilon$,

$$\frac{1}{\epsilon(K^2 - 1)\cos^2\delta + K^4} = \frac{1}{K^4}\left(1 - \epsilon\frac{K^2 - 1}{K^4}\cos^2\delta\right.$$
$$\left. + \epsilon^2\frac{(K^2 - 1)^2}{K^8}\cos^4\delta\right). \tag{5.10}$$

We will also use the following,

$$\sin\delta = \sin\delta_0 + (\epsilon\delta_1 + \epsilon^2\delta_2 + ...)\cos\delta_0 + ... \tag{5.11}$$

$$\cos\delta = \cos\delta_0 - (\epsilon\delta_1 + \epsilon^2\delta_2 + ...)\sin\delta_0 + ...$$

Substituting equations (5.10), (5.11) and the assumed power series expansion for $u$, $\Omega$ and $\omega$ into the (5.5), (5.6) and (5.7) and equating the coefficients of the corresponding powers of $\epsilon$, one obtains the following equations for the three leading orders,

40

$$\dot{u}_0 = b\Omega_0^2 \tag{5.12}$$

$$\dot{u}_1 = 2b\Omega_0\Omega_1 \tag{5.13}$$

$$\dot{u}_2 = \frac{1}{K^6}u_0\Omega_0\sin\delta_0\cos\delta_0 + b\Omega_1^2 + 2b\Omega_0\Omega_2 + bK^2\omega_0^2\cos\delta_0 \tag{5.14}$$

$$\dot{\Omega}_0 = -\frac{u_0\Omega_0}{bK^2} \tag{5.15}$$

$$\dot{\Omega}_1 = -\frac{u_1\Omega_0}{bK^2} - \frac{\Omega_1 u_0}{bK^2} \tag{5.16}$$

$$\dot{\Omega}_2 = \frac{1}{bK^6}u_0\Omega_0\cos^2\delta_0 - \frac{u_2\Omega_0}{bK^2} - \frac{u_1\Omega_1}{bK^2} - \frac{u_0\Omega_2}{bK^2} - \frac{1}{K^2}\omega_0^2\sin\delta_0 \tag{5.17}$$

$$\dot{\omega}_0 = -\frac{u_0\Omega_0}{bK^4}\cos\delta_0 \tag{5.18}$$

$$\dot{\omega}_1 = -\frac{1}{bK^4}(u_1\Omega_0 + u_0\Omega_1)\cos\delta_0 \tag{5.19}$$

$$\dot{\omega}_2 = \Big(\frac{1}{bK^8}u_0\Omega_0\cos^2\delta_0 - \frac{u_2\Omega_0}{bK^4} - \frac{u_1\Omega_1}{bK^4} - \frac{u_0\Omega_2}{bK^4}$$
$$- \frac{1}{K^4}\omega_0^2\sin\delta_0\Big)\cos\delta_0 + \frac{1}{K^4 b}u_0\Omega_0\delta_2\sin(\delta_0). \tag{5.20}$$

The validity of the regular perturbation expansion for short time periods is borne from the close match between the solution $u_0(t) + \epsilon u_1(t) + \epsilon^2 u_2(t)$ with the solution of (5.5) as shown in Fig. 5.4 (a). A similar comparison for the angular velocities is shown in Figs. 5.4 (b) and (c). The initial conditions for a direct numerical simulation of (5.5), (5.6) and (5.7) are $(u(0) = 0, \Omega(0) = 0.1, \omega(0) = 1)$. Since the perturbation expansion, (5.9) is valid for any arbitrarily small value of $\epsilon$, the initial conditions for simulation of the perturbation expansion equations are $(u_0(0) = 0, u_1(0) = 0, u_2(0) = 0)$, $(\Omega_0(0) = 0.1, \Omega_1(0) = 0, \Omega_2(0) = 0)$ and $(\omega_0(0) = 1, \omega_1(0) = 0, \omega_2(0) = 0)$.
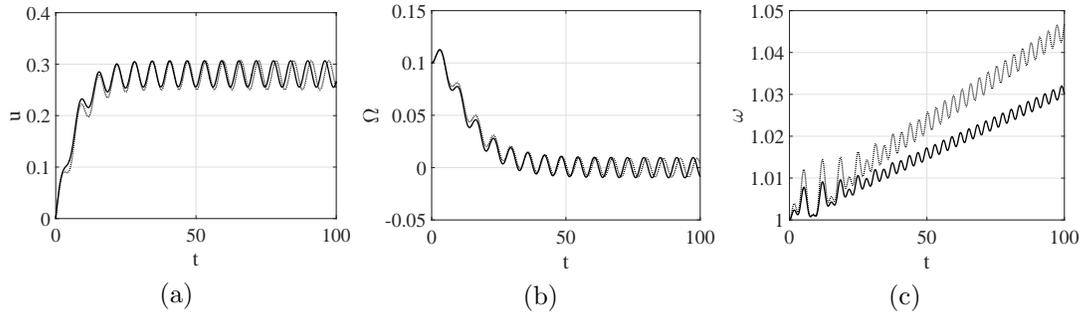


Figure 5.4: Simulation of the Chaplygin sleigh with a small internal rotor for initial conditions $u(0) = 0$, $\Omega(0) = .1$, $\omega(0) = 1$ ($u_0(0) = 0$, $\Omega_0(0) = .1$, $\omega_0(0) = 1$ and other initial conditions are zero for the regular expansion). The solution due to the perturbation expansion is shown as a dashed line and the exact solution as a solid line.

41

In Fig. 5.4 (a) and (b) we see that the longitudinal velocity of the sleigh increases from zero and begins to show small oscillations with a non zero mean. The angular velocity of the sleigh, $\Omega$, decays to zero with small oscillations. Except for the oscillations in the growth of $u$ and the decay of $\Omega$, the evolution of these velocities is similar to those of the regular Chaplygin sleigh. But more significantly there is a transfer of kinetic energy to the motion of the internal rotor, with $\omega(t)$ experiencing slow growth with oscillations. The oscillations in $u(t)$, $\Omega(t)$ and $\omega(t)$ can be explained by the regular perturbation expansion equations. The error between the perturbation solution for $\omega$ and a direct numerical simulation grows faster and even on a time scale of 100s the error is about 2%. This can be expected since the angular velocity $\omega(t)$ can have secular growth as seen in fig. 5.2

Equations (5.12) and (5.15) represent the leading order equations for the evolution of the velocity of the sleigh. These equations are the same as those that describe the motion of the Chaplygin sleigh without an internal rotor, (5.5), (5.7). The leading order solutions $u_0$ and $\Omega_0$ are shown in Fig. 5.5(a) and (c). The $O(\epsilon^0)$ solutions exhibit the behavior of a regular Chaplygin sleigh without an internal rotor.

The right hand sides of equations (5.13) and (5.16) are zero since the initial conditions $(u_1(0) = 0, \Omega_1(0) = 0, \omega_1(0) = 0)$ are the fixed points of the $O(\epsilon)$ equations. Therefore the $O(\epsilon)$ solution is always zero.

The first term on the right hand side of (5.18) decays to zero since $\Omega_0$ decays to zero. Therefore $\omega_0$ converges to a constant value as shown in Fig. 5.5 (e). The first term on the right hand side of (5.14) decays to zero since $\Omega_0$ decays to zero. The second term $b\Omega_1^2$ is zero and the third term $2b\Omega_0\Omega_2$ decays to zero. Therefore the equation (5.14) can be approximated as

$$\dot{u}_2 \approx bK^2\omega_0^2 \cos\delta_0. \tag{5.21}$$

We next make a series of approximations for the relative angle $\delta$ by first noting that

$$\begin{aligned}
\delta(t) &= \delta(0) + \int_0^t (\Omega - \omega)dt \\
&= \delta(0) + \int_0^t (\Omega_0 - \omega_0)dt + \epsilon^2 \int_0^t (\Omega_2 - \omega_2)dt + ....
\end{aligned} \tag{5.22}$$

Since $\Omega_0$ decays to zero rapidly and $\omega_0$ reaches a constant value rapidly, we will make the approxi-

42

mation

$$\delta_0 \approx \delta(0) - \omega_0 t \tag{5.23}$$

Assuming $\delta(0) = 0$, it is clear from (5.21), $u_2$ shows oscillatory behavior, with the oscillations becoming nearly periodic after a short transient, as shown in Fig. 5.5(b).

A similar argument can be made for the right hand side of (5.17). First we set $u_1(t) = 0$, $\Omega_1(t) = 0$ and let $\Omega_0 \to 0$ to obtain

$$\dot{\Omega}_2 \approx -\frac{u_0 \Omega_2}{bK^2} - \frac{1}{K^2}\omega_0^2 \sin\delta_0. \tag{5.24}$$

The stable solutions to the leading order equations are such that $u_0 > 0$. Therefore first term on the right hand side of (5.24) causes a decay of $\Omega_2 \to 0$. The second term causes periodic oscillations around zero, as shown in Fig. 5.5 (f). Equation (5.24) is a linear differential equation with a periodic forcing, the steady state solution for which is also periodic with the same frequency as the forcing frequency,

$$\Omega_2 = -\left(\frac{1}{\sqrt{\omega_0^2 + \frac{u_0^2}{b^2 K^4}}}\right) \frac{\omega_0^2}{K^2} \sin(\delta + \phi_1) \tag{5.25}$$

where $\phi_1 = tan^{-1}\left(\frac{-\omega_0 bK^2}{u_0}\right) = 0.4705\pi \approx \pi/2$. The amplitude of the steady solution of $\Omega_2$ is 0.892.

The evolution of $u_2$ and $\Omega_2$ by the simulation of (5.12)-(5.20) is shown in Fig. 5.5 (b) and (d). The two velocities converge to oscillatory solutions with a time period of $T_1 = 6.276$ that is nearly equal to $\frac{2\pi}{\omega_0} = 6.277$, which bears out the validity of the series of approximations we made leading to (5.25).

The steady state behavior of $\omega_2$ , seen in Fig. 5.5 (f) is a periodic function with time period $T_2 = 3.138$ which is half that of $T_1$. This can be understood by examining the several terms on the right hand side of (5.20). Since $\Omega_0 \to 0$ and $u_1 = 0$ and $\Omega_1 = 0$, the steady state evolution of $\omega_2$ is approximately governed by the equation

$$\dot{\omega}_2 = -\frac{u_0 \Omega_2}{bK^2}\cos\delta_0 - \frac{1}{K^2}\omega_0^2 \sin\delta_0 \cos\delta_0$$
$$\approx \frac{u_0 A}{bK^2}\cos^2\delta_0 - \frac{1}{2K^2}\omega_0^2 \sin 2\delta_0.$$

where we substituted for the steady state solution of $\Omega_2$ from (5.25) with the further approximation that the phase angle $\phi_1$, in (5.25) is approximately $\pi/2$. It is straightforward to show that

43
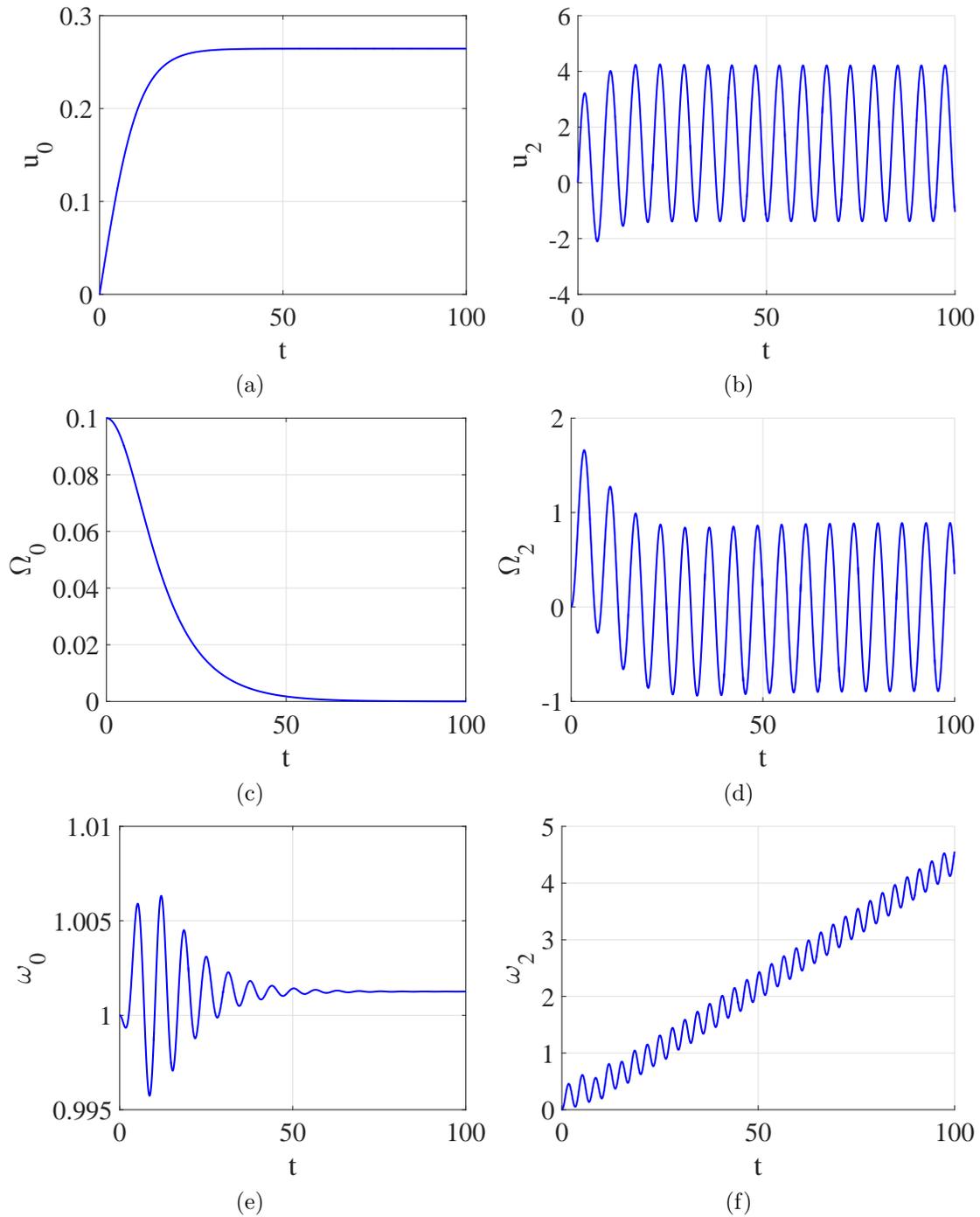
Figure 5.5: Order $\epsilon^0$ and order $\epsilon^2$ solutions for the velocities of the sleigh with initial conditions $u_0 = 0$, $\Omega_0 = .1$, $\omega_0 = 1$, $\delta_0 = 0$ and all other initial conditions zero. Order one $\epsilon^1$ solutions remain zero for all time.

$$\dot{\omega}_2 = \frac{u_0 A}{2bK^2} + \frac{u_0 A}{2bK^2} \cos 2\delta_0 - \frac{\omega_0^2}{2K^2} \sin 2\delta_0$$
$$= \frac{u_0 A}{2bK^2} - B \sin\left(2\delta_0 - \phi_2\right)$$
$$\approx \frac{u_0 A}{2bK^2} + B \sin\left(2\omega_0 t + \phi_2\right) \tag{5.26}$$

where

$$B = \sqrt{\left(\frac{u_0 A}{2bK^2}\right)^2 + \left(\frac{\omega_0^2}{2K^2}\right)^2}$$

and $\phi_2 = tan^{-1}\left(\frac{u_0 A}{b\omega_0^2}\right)$. The constant term and the periodic term on the right hand side of (5.26) produce respectively a linear growth in $\omega_2$ and an oscillatory response with time period $T_2 = \frac{\pi}{\omega_0}$. Using the previously obtained values of $\omega_0$ and $u_0$ we find that $T_2 = 3.135$, $B = 0.238$ and the average value of $\Omega_2$ grows linearly at a rate of 0.0415. A direct simulation of equation (5.20) shown in Fig. 5.5 (f) show that time period $T_2 = 3.138$, $B = 0.241$ and the linear growth rate is 0.0445 which are in very good agreement with the values obtained through the analytical approximations. Note that the growth rate is approximate and any discrepancy from the true growth rate causes the error in $\omega$ to accumulate. This is why in Fig. 5.4 (c) we see the approximate and actual solutions slowly growing apart.

As Fig. 5.2 (a) shows the longitudinal velocity decays with oscillations after about $t > 100$ until about $t = 8,700$. In the same time period the angular velocity of the sleigh oscillates about zero with the amplitude steadily increasing until it reaches a nearly steady value as seen in Fig. 5.2 (b). This second transient phase is generic to any initial conditions with positive longitudinal velocity, although the time period associated with this transient behavior changes with the initial conditions.

This second transient phase cannot be explained through a perturbation analysis. The third order perturbation solutions, $u_3$, $\Omega_3$ and $\omega_3$ turn out to be zero. The equations for the fourth order variables contain many secular terms, leading to unbounded solutions. It is however easy to see that the velocities, $u$, $\Omega$ and $\omega$ should remain bounded since the kinetic energy is invariant. We first point out that the second order solution, $\omega_2$ itself grows without a bound. Therefore in the second transient stage the decay of the longitudinal velocity $u$ is due to the conservation of the kinetic energy of the sleigh.

45

## 5.3  Chaotic Dynamics of the Sleigh on the Attractor

Numerical simulations show that for all initial conditions, except those of a zero measure, the longitudinal velocity of the sleigh converges to a periodic function with multiple frequencies. This is shown in Fig. 5.2 (a) where from about $t = 8,700$ the velocity $u$ undergoes rapid oscillations, with the mean value of $u$ itself oscillating at a much lower frequency. The angular velocity of the sleigh also undergoes high frequency oscillations with zero mean, along with a spike that occurs between much longer time intervals, Fig. 5.2 (b). The angular velocity of the rotor also oscillates with a high frequency with the mean value oscillating at a lower frequency, Fig. 5.2 (c). We will denote this state of motion of the sleigh as the steady state. To explain this steady state behavior we show in Fig. 5.6 the kinematic variables over a smaller time window along with the trajectory of the sleigh in the plane during this time window.
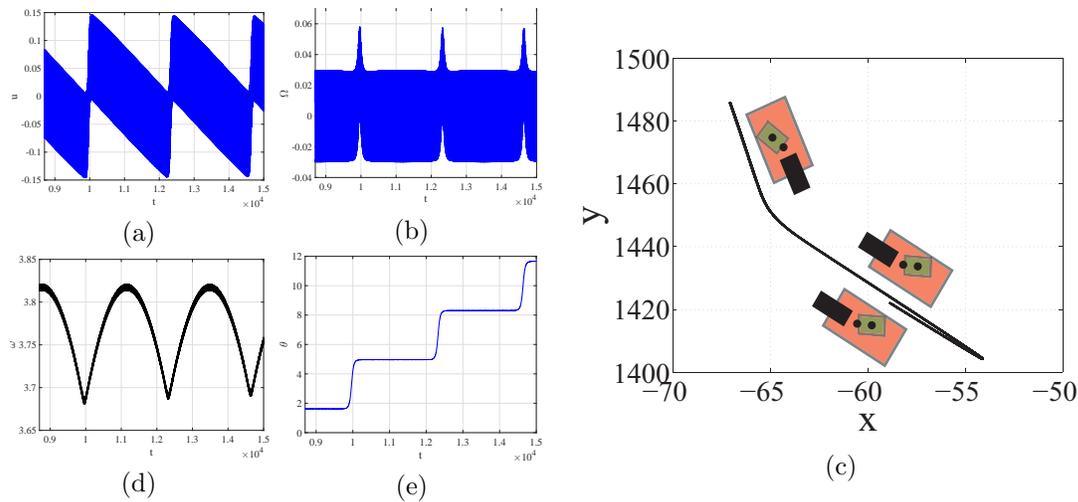


Figure 5.6: Steady State behavior of the sleigh. Initial conditions are $u_0 = 0$, $\Omega = .1$, and $\omega = 1$. Subfigures a), b), d) and e) show the parameters of the sleigh over time. Subfigure c) shows the trajectory of the sleigh for the time window $t = 9,000s$ to $t = 11,500$.

In Fig. 5.6 (a) at about $t = 9,800$, despite the oscillations, the maximum longitudinal velocity of the sleigh is negative, i.e. the cart moves backwards. As shown in the phase portrait for the zeroth order dynamics, the motion of the Chaplygin sleigh in the backward direction is unstable. Therefore at about $t = 10,000$ $u$ increases, resulting in an increase in magnitude of $\Omega$. This sudden increase in the angular velocity of the sleigh is reflected in the spike in Fig. 5.6 (b). Figure 5.6 (c) shows the trajectory of the sleigh in the physical plane during this spike in angular velocity. In the first transition, between position A and position B, shown in Fig. 5.6 (c) the sleigh's orientation

changes by a large amount (nearly $\pi$ radians) due to the spike in the angular velocity of the sleigh. The motion of the sleigh changes from the backward (in body frame) direction to forward direction, i.e. $u$ becomes positive. At about $t = 12,000$ the longitudinal velocity of the sleigh is once again wholly negative. The average motion of the cart is once again in the backward direction (in the body frame). What appears to be a sharp turn in the trajectory of the sleigh in the $x - y$ plane is actually the second transition which is characterized by the average longitudinal velocity becoming negative. So the sleigh does not execute a turn at this point, it simply changes the direction of travel.
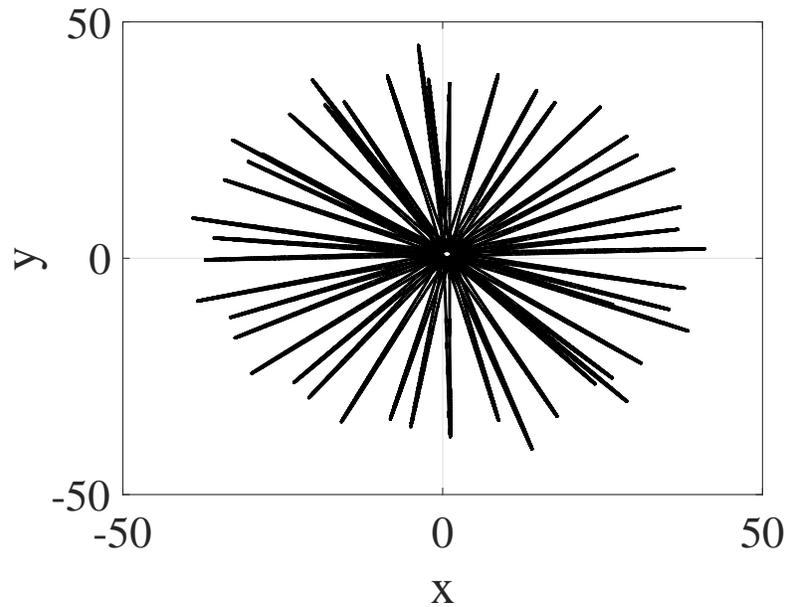


Figure 5.7: Path of the sleigh after $t = 100,000s$. Initial conditions are taken after the transient phase to capture the steady state trajectory.

As the mean value of the longitudinal velocity itself undergoes low frequency oscillations (Fig. 5.6 (a)) the trajectory of the sleigh in the $x - y$ plane undergoes what seem like many sharp turns. Figure 5.7 shows a generic trajectory of the sleigh in the $x - y$ plane. This trajectory of the sleigh in the $x - y$ plane is in sharp contrast to the trajectory of the Chaplygin sleigh without the internal rotor, whose angular velocity converges to zero for almost all initial conditions. The trajectory of a Chaplygin sleigh without the internal rotor converges asymptotically to a straight line in the $x - y$ plane and the trajectory is not bounded, see Fig. 2.1 (b). In contrast the trajectory of the sleigh with even a small passive rotor is bounded as shown in fig. 5.7. Moreover numerical simulations suggest that the path of the sleigh is not periodic. To illustrate the non periodic

47

nature of the trajectories of the dynamical system (5.5)-(5.8), we consider the Poincare section, $\Sigma_{2\pi} = \{u, \Omega, \omega, \delta = 2n\pi\}$ where $n = 0, 1, 2, 3...$ and the first return Poincare map to the Poincare section,

$$P_{2\pi} : (u_n, \Omega_n, \omega_n, 2n\pi) \mapsto \Phi_{t_n}^{t_{n+1}}(u_n, \Omega_n, \omega_n, 2(n+1)\pi). \tag{5.27}$$

Figure 5.8(a) shows the Poincare map for a large number of iterations. The Poincare map is not periodic for thousands of iterations and fills out a closed curve. We further consider the Poincare section, $\Sigma_{\pi/2} = \{u, \Omega, \omega, \delta = n\pi/2\}$ and the first return Poincare map, $P_{\pi/2}$ to this section $\Sigma_{\pi/2}$. Figure 5.8 (b) shows a large number of iterations of this map, which form four distinct closed loops. In the steady state the trajectory of the dynamical system (5.5)-(5.8) lies on an attractor $\mathcal{A}$. The iterations of these Poincare maps lie on the projection of the attractor, $\pi_{\mathcal{A}} \subset \mathbb{R}^3$ which is the projection of the flow map $\pi_{\Phi} : \mathbb{R}^3 \times S^1 \mapsto \mathbb{R}^3$. The attractor, $\pi_{\mathcal{A}}$, is shown by the small dots in Fig. 5.8 (b).

The reduced equations of motion of the sleigh, (5.5) - (5.8) are dissipative in the sense of decreasing phase space volumes. The trace of the Jacobian obtained by linearizing these reduced velocity equations is nonzero for almost any $(u, \Omega, \omega, \delta)$. However the kinetic energy of the sleigh is an invariant. The manifold $\mathcal{M}$ is foliated by level sets of the kinetic energy. Trajectories that lie on a level set of the kinetic energy converge to an attractor that is a subset of this level set. The attractor and its projection shown in Fig.5.8 (b) are subsets of an invariant level set of the kinetic energy. The attractor is dependent on the kinetic energy of the sleigh as well as the value of $\epsilon$. However the topology of the attractor persists across a broad range of values of $\epsilon$, and $E$. For example Fig. 5.8 (c) shows the attractor for a different energy $E = 0.8313$ and the same $\epsilon = 0.1$ while Fig. 5.8 (d) shows the attractor for the same energy and $\epsilon = 0.01$. For the combination of larger values of $\epsilon$ and smaller values of total energy $E$, the attractor $\pi_{\mathcal{A}}$ can be flatter with smaller variations in the range of the $\omega$.

The dynamics on the attractor have sensitive dependence on initial conditions. This can be seen through the computation of the Lyapunov exponents. Adopting the algorithm proposed in [23], we computed the four Lyapunov exponents for the dynamical system, (5.5)-(5.22). The four Lyapunov exponents are $2.9e^{-4}$, $2.203e^{-4}$, $-2.2e^{-4}$ and $2.02e^{-5}$. The Lyapunov exponents were computed for a simulation time of 4000s at intervals of 0.01s. A pre simulation for an initial run time of 10000s performed first to allow the transient dynamics to decay to very small values. We
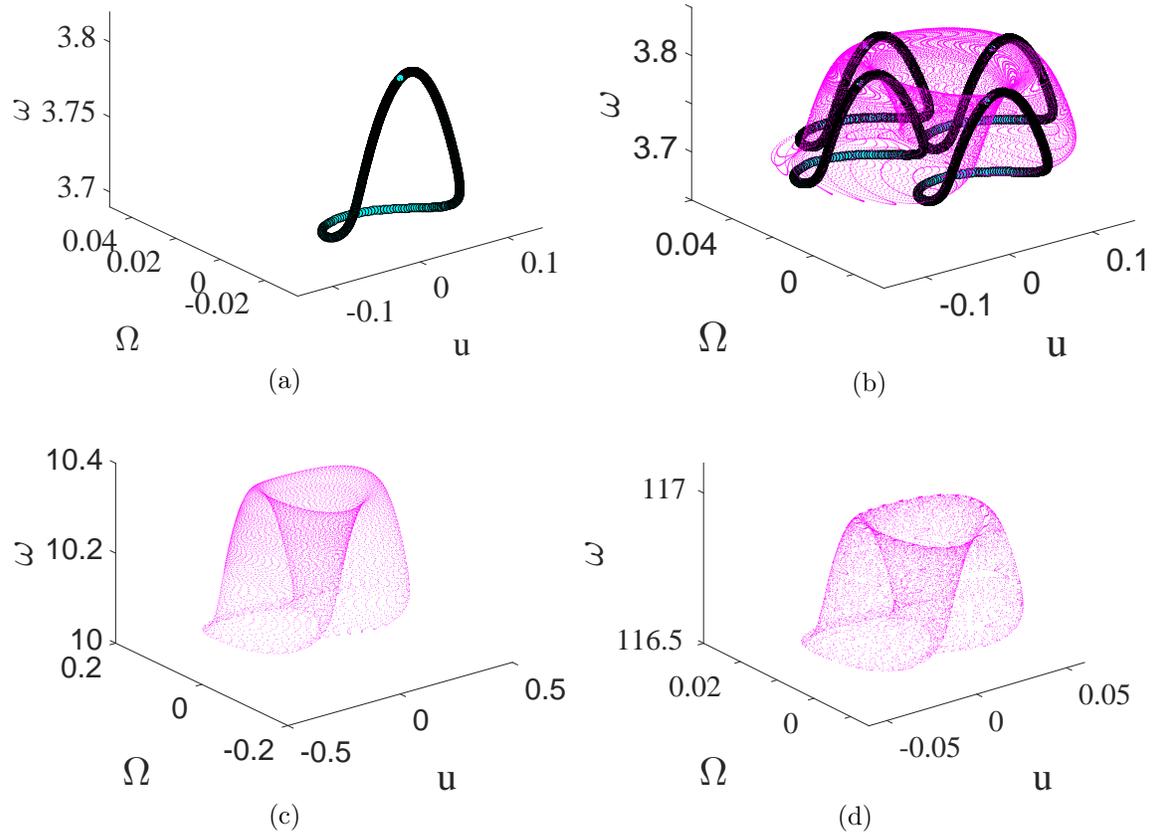
Figure 5.8: (a) Iterations of the Poincare map $P_{2\pi}$. (b) Iterations of the Poincare map $P_{\pi/2}$ shown by the large filled circles forming four closed loops lie on the attractor $\pi_\Phi\mathcal{A}$ shown by the smaller dots, energy is $E_0 = 0.1127$ and $\epsilon = 0.1$ (c) attractor $\pi_\Phi\mathcal{A}$ for $\epsilon = 0.1$ and an energy of $E = 0.8313$ and (d) for $\epsilon = 0.01$ and $E = 0.1127$.

verified the convergence of the computation of the Lyapunov exponents by checking the variation in the computed values of these exponents. This variation of the Lyapunov exponents between time steps oscillated between $7 \times 10^{-8}$ and $-9 \times 10^{-8}$ for the last 200s of the simulation. This variation is of the order of 0.01% in the values of the positive Lyapunov exponents.

The leading Lyapunov exponents are calculated for different energy levels, $E$, holding the values of $\epsilon = 0.1$ and $b = 1$, to verify that the chaotic behavior does not depend on the energy on the system. The highest Lyapunov exponent plotted against the energy is shown in Fig. 5.9. The highest Lyapunov exponent increases with the energy associated with the system and the LE is positive for energy as low as $10^{-4}$. Similarly changes to the parameters $\epsilon$ and $b$ across a range of values of the energy $E$ produce chaotic dynamics, with the largest Lyapunov exponent always being

www.manaraa.com
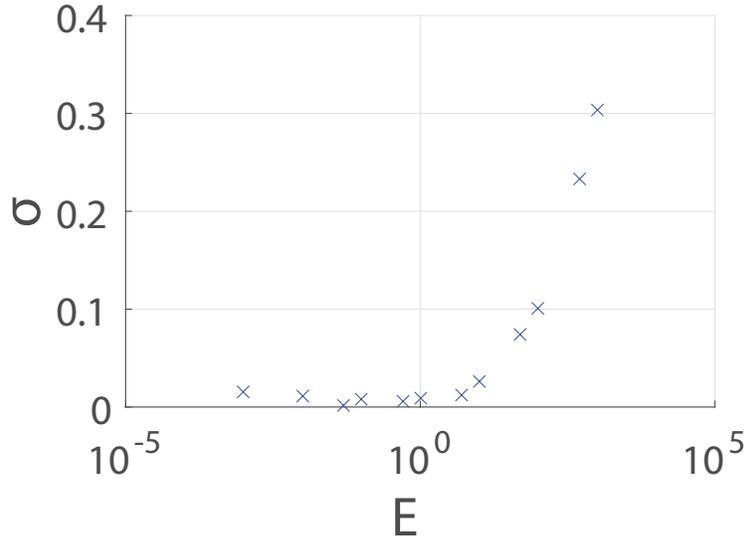
Figure 5.9: Maximum Lyapunov exponent for energies ranging from $E = 10^{-3}$ to $E = 10^3$ with $\epsilon = 0.1$. The smallest value of leading Lyapunov exponent in the above graph is about $1.1 \times 10^{-4}$.

positive. The leading Lyapunov exponent is shown in Fig. 5.10 for a range of values of $b$ and $\epsilon$ with $E = 0.1127$. The smallest value of the leading Lyapunov exponent in Fig. 5.10 is greater than $10^{-4}$. The calculations of the Lyapunov exponents strongly suggest the existence of sensitive dependence of initial conditions, positive Lyapunov exponents and a chaotic attractor for the dynamical system (5.5)-(5.8) for a broad range of parameters $\epsilon$, $b$ and $E$.

In order to further verify the aperiodic behavior of flow of (5.5)-(5.8) we plot the return times for the map $P_{2\pi}$. The return times for two different values of $\epsilon$ are shown in Fig. 5.11 for a large number of iterations of the map $P_{2\pi}$ are shown. The return times for both the cases in fig. 5.11 are such that they are bounded in an interval. Furthermore, no two return times are the same upto a precision of $10^{-7}$. Return time computations for the map $P_{2\pi}$ for a broad range of values of $\epsilon$, $E$ and $b$ show a similar behavior, suggesting the presence of a large or infinite number of frequencies for the function $\delta(t)$.

The dynamics on the attractor are also aperiodic. A power spectral density plot of $u(t)$ and $\Omega(t)$ reveal that a very large number of frequencies are present clustered into two regions of the frequency spectrum. These plots for the case of $\epsilon = 0.1$ is shown in Fig. 5.12 and for the case of $\epsilon = 0.01$ in fig. 5.13. In Fig. 5.12 (a)-(b) the clustering of the power spectrum for the $u(t)$ and $\Omega(t)$
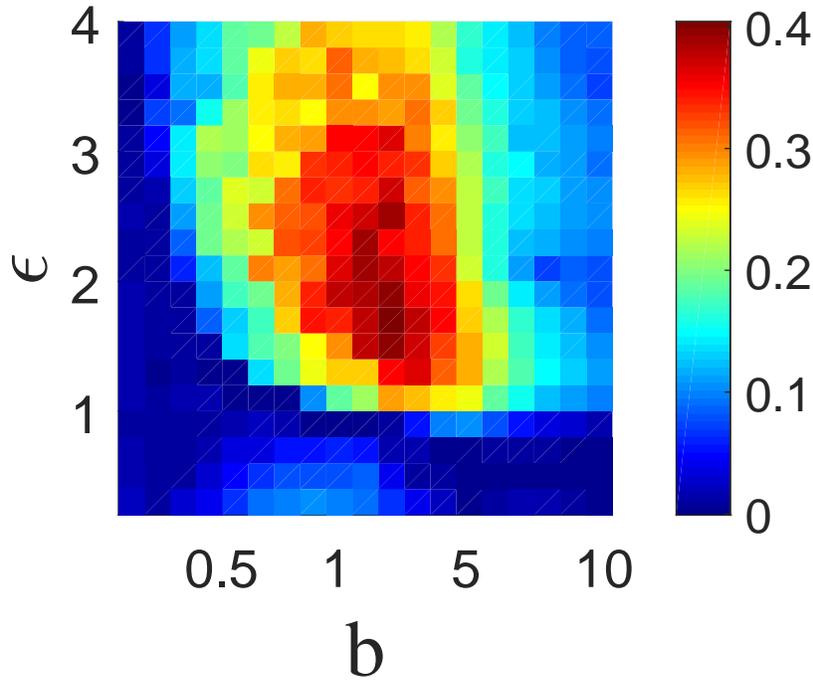
Figure 5.10: Maximum Lyapunov exponent for $E = 0.1127$ for a range of $\epsilon$ and $b$. The largest Lyapunov exponent is always positive.
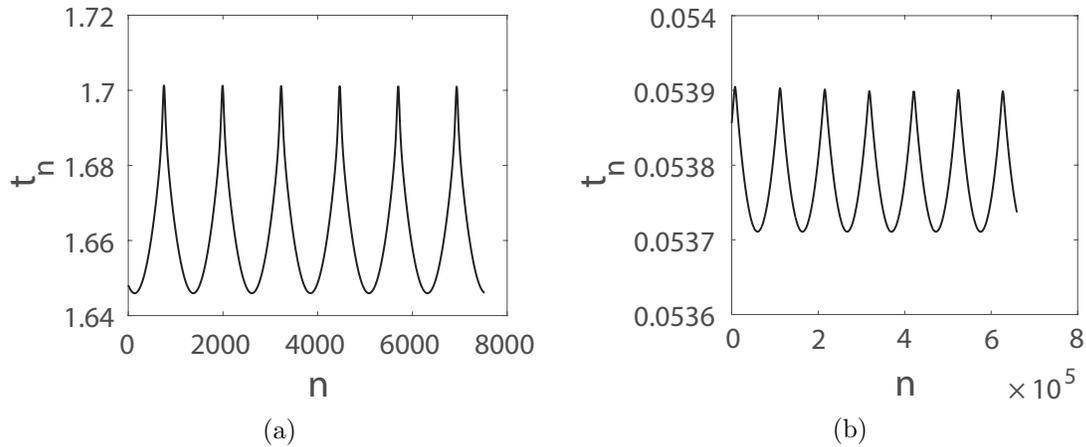


Figure 5.11: Return times $t_n$ of the Poincare map $P_{2\pi}$ for (a) $\epsilon = 0.1$ and (b) $\epsilon = 0.01$ with an energy of $E = 0.1127$.

around the frequency zero has many distinct well defined peaks, which broaden as the frequency increases, suggestive of quasiperiodic behavior. The power spectrum away from zero is clustered in a broadband on a frequency interval that is approximately $f \in [1.45, 1.8]$. The frequency spectra are computed in MATLAB using the $fft$ function with an input signal on a time interval 5000s with

51

time steps of $10^-3$. As in the computation of the Lyapunov exponents a pre simulation for 10000s was performed to allow the transient dynamics to decay to negligible values.
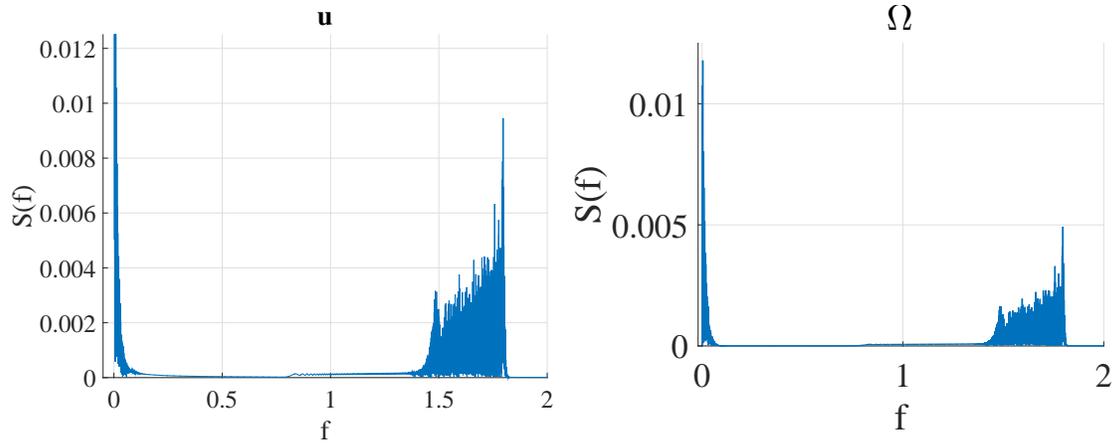


Figure 5.12: Power spectral density plots for $u$ and $\Omega$. Amplitude $S(f)$ is plotted against frequency $f$. $\epsilon = 0.1$ and $E = 0.1127$.

For a smaller value of $\epsilon = 0.01$, Fig. 5.13, the frequency spectra of $u(t)$ and $\Omega(t)$ have a narrower the frequency interval $[0.56, 0.6]$ in which a very large number of frequencies are present in a continuous band. At the zero frequency the frequency spectra has many but distinct peaks, suggestive of quasiperiodic behavior in this small frequency band.
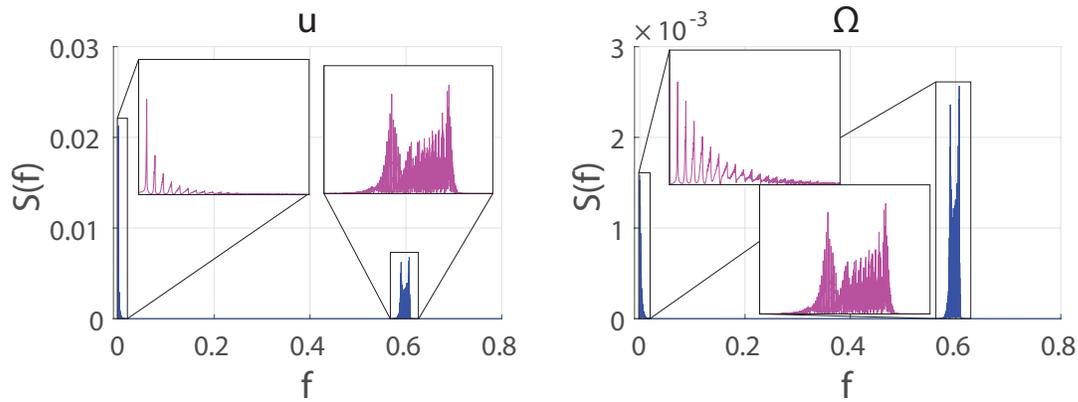


Figure 5.13: Power spectral density plots for $u$ and $\Omega$. Amplitude $S(f)$ is plotted against frequency $f$. $\epsilon = 0.01$ and $E = 0.1127$.

The power spectrum plots for $u(t)$ and $\Omega(t)$ together with the return times suggest that within a small interval all frequencies are present demonstrating the aperiodic behavior. At the same time, the presence of fat peaks in the frequency spectra for smaller $\epsilon$ (Fig. 5.13) along with the

52

the smaller difference in the return times of the map $\P_{2\pi}$ (Fig. 5.11) suggest a possible quasiperiodic route to chaotic behavior. Such chaotic behavior can be verified numerically for values of $\epsilon$ as small as $10^{-5}$. However the numerics become unreliable for as the parameetr $\epsilon$ becomes smaller. Similarly for very large values of $\epsilon$, exceeding 20, the leading Lyapunov exponents become smaller than $10^{-5}$ suggesting that the chaotic behavior could disappear in atleast some windows as the parameters of the system vary.

An analytical approach to the possible bifurcations in the dynamical system (5.5)-(5.8) present many challenges because of the singular nature of $\epsilon$. In the absence of the internal rotor, i.e. $\epsilon = 0$, the dynamical system (5.5)-(5.8) reduces to a two dimensional system. The solution to this case is that the angular velocity of the sleigh, $\Omega$, decays to zero and the longitudinal velocity of the sleigh, $u$, converges to a constant value. For any small but finite $\epsilon$, the dimension of the system increases to four. This singular nature of $\epsilon$ does not allow a traditional analysis of bifurcations (if any) of the invariant sets of the dynamical system (5.5)-(5.8) and the route to chaos. The numerical analysis however indicates that the system follows a quasiperiodic route to chaos around $\epsilon = 0$.

# Chapter 6

# Dynamics Due to a Passive Degree of Freedom and Elastic Potential

In this section we consider the same system as above but also in the presence of a spring connecting the sleigh and the rotor. Here we summarize the results of [26]. Overall we will see that the presence of a spring stabilizes many of the fixed points of the above system, replacing chaotic dynamics with convergence to fixed points or limit cycles. In order to model the effect of a Duffing spring we introduce a nonzero potential energy of the form

$$\mathcal{V}(\delta) = k_1 \delta^2 + k_2 \delta^4$$

where $k_1 \in \mathbb{R}$ and $k_2 > 0$. In order to derive the equations of motion we follow the steps in chapter 2 and then manually eliminate the Lagrange multiplier as in the previous section to get

$$\begin{bmatrix} \mathcal{M}_b & 0 \\ 0 & 1 \end{bmatrix} \dot{\xi} = \begin{bmatrix} \omega_1^2(m_r a \cos \delta + mb) + m_r a \omega_2^2 \cos \delta + 2a m_r \omega_1 \omega_2 \cos(\delta) \\ m_r ab\omega_2^2 sin\delta + 2m_r ab\omega_1 \omega_2 \sin(\delta) - u\omega_1(m_r a \cos(\delta) + mb) \\ -m_r au\omega_1 \cos \delta - m_r ab\omega_1^2 \sin(\delta) - 2k_1 \delta - 4k_2 \delta^3 \\ \omega_2 \end{bmatrix} \tag{6.1}$$

where $\omega_1 = \dot{\theta}$, $\omega_2 = \dot{\delta}$, and $\delta$ is the angle made by the internal rotor with respect to the body $X_b$ axis and $\mathcal{M}_b$ represents the locked inertia tensor,

$$\mathcal{M}_b = \begin{bmatrix} m & -m_r a \sin(\delta) & -m_r a \sin(\delta) \\ -m_r a \sin(\delta) & I_c + I_r + mb^2 + m_r a^2 + 2abm_r \cos(\delta) & m_r ab \cos\delta + I_r + m_r a^2 \\ -m_r a \sin(\delta) & m_r ab \cos\delta + I_r + m_r a^2 & I_r + m_r a^2 \end{bmatrix}. \quad (6.2)$$

## 6.1 Fixed Points of the Elastic Chaplygin Sleigh System and Their Stability

The block diagonal matrix $\begin{bmatrix} \mathcal{M}_b & 0 \\ 0 & 1 \end{bmatrix}$, hereafter denoted by $\mathbb{A}$, is invertible since the diagonal block $\mathcal{M}_b$ is the locked inertia tensor, a symmetric positive definite matrix. Denoting the right hand side of (8.17) by $\mathbf{g}(\xi)$, dynamical system (8.17) can be rewritten as

$$\dot{\xi} = \begin{bmatrix} \mathcal{M}_b & 0 \\ 0 & 1 \end{bmatrix}^{-1} \mathbf{g}(\xi) = \begin{bmatrix} \mathcal{M}_b^{-1} & 0 \\ 0 & 1 \end{bmatrix} \mathbf{g}(\xi) \equiv \mathbf{f}(\xi). \quad (6.3)$$

The fixed points of (8.12), denoted by $\xi^e = (u^e, \omega_1^e, \omega_2^e, \delta^e)$ satisfy $\mathbf{f}(\xi^e) = 0$, i.e., $\mathbb{A}^{-1}\mathbf{g}(\xi^e) = 0$. Since $\mathbb{A}^{-1}$ and $\mathcal{M}_b^{-1}$ are obviously invertible, the only solution to $\mathbb{A}^{-1}\mathbf{g}(\xi^e) = 0$ is the trivial solution $\mathbf{g}(\xi^e) = 0$. The last equation of (8.17), $\dot{\delta} = \omega_2$, implies $\omega_2^e = 0$, for any fixed point of (8.17). The total energy of the system, $E$, the sum of the kinetic energy of the sleigh, $\mathcal{T}(q, \dot{q})$ and the potential energy, $\mathcal{V}(q)$ stored in the elastic element is a constant, since the nonholonomic constraint force does not do any work. The velocity of the sleigh $u$ can be eliminated in the dynamical system,

$$u(\omega_1, \omega_2, \delta; E) = \frac{1}{m} \Big( \sin(\delta)\, am_r \omega_1 \pm \big( (\sin(\delta))^2\, a^2 m_r{}^2 \omega_1{}^2 - 2\cos(\delta)\, abmm_r \omega_1{}^2 - a^2 mm_r \omega_1{}^2$$
$$- b^2 m^2 \omega_1{}^2 - 2\delta^4 k_2\, m - I_r\, m\omega_1{}^2 - I_c m\omega_1{}^2 - 2\delta^2 k_1 m + 2Em)^{1/2} \Big) \quad (6.4)$$

Similarly, for a triplet $\omega_1^e$, $\omega_2^e = 0$ and $\delta^e$, a one parameter set $u^e(E)$ exists. For instance an inspection of (8.17) together with (6.4) shows that one set of fixed points are given by $(\omega_1^e = 0, \omega_2^e = 0, \delta^e = 0)$

and

$$u^e = \sqrt{\frac{2E}{m}}. \tag{6.5}$$

The fixed points of dynamical system (8.17) are nonisolated. The stability of such nonisolated fixed points can be analyzed by first reducing the dimension of (8.17).

If the four components of the vector field $\mathbf{f}(\xi)$ are denoted as $\mathbf{f}(\xi) = [f_1(\xi), f_2(\xi), f_3(\xi), f_4(\xi) = \omega_2]^T$, then the equations of motion reduced to a constant energy manifold are the last three equations of (8.12) with the velocity $u$ replaced by (6.4)

$$\begin{bmatrix} \dot{\omega_1} \\ \dot{\omega_2} \\ \dot{\delta} \end{bmatrix} = \begin{bmatrix} f_2(E; \omega_1, \omega_2, \delta) \\ f_3(E; \omega_1, \omega_2, \delta) \\ \omega_2 \end{bmatrix} \equiv \mathbf{f}_R. \tag{6.6}$$

The fixed points of (6.6), denoted by $(\omega_1^e, \omega_2^e = 0, \delta^e)$ satisfy $\mathbf{f}_R(E(u^e); \omega_1, \omega_2, \delta) = 0$. Equivalently the fixed points satisfy $\mathbf{g}_2(E(u^e); \omega_1^e, \omega_2^e, \delta^e) = 0$, $\mathbf{g}_2(E(u^e); \omega_1^e, \omega_2^e, \delta^e) = 0$ and $\omega_2^e = 0$. Every nonisolated fixed point $\xi^e$ of the original dynamical system (8.12), leads to an isolated fixed point $(\omega_1^e, \omega_2^e = 0, \delta^e)$ on the manifold of constant energy, $E(u^e)$. To analyze the stability of these isolated fixed points we linearize the system about $(\omega_1^e, \omega_2^e = 0, \delta^e)$. This allows us to determine whether the fixed point is stable or unstable by examining the eigenvalues of the Jacobian $\mathbf{Df}_R$, is these eigenvalues do not lie on the imaginary axis. Supposing the eigenvalues of the Jacobian $D\mathbf{f}_R(\omega_1^e, \omega_2 = 0, \delta^e)$ are denoted by $(\lambda_1, \lambda_2, \lambda_3)$ and

$$\sigma = \max_{i=1,2,3} (\mathrm{Re}(\lambda_i))$$

then the fixed point $(\omega_1^e, \omega_2^e = 0, \delta^e)$ is stable if $\sigma < 0$ and unstable if $\sigma > 0$.

Due to the large parametric space in (6.6), the following scaling will be introduced,

$$\frac{m_c}{m} = \epsilon, \quad \frac{b}{a+b} = \epsilon, \quad I_c = K m_c b^2 = K m l^2 \epsilon^3, \quad I_r = K m_r a^2 = K m l^2 (1-\epsilon)^3 \tag{6.7}$$

where $l = a + b$. The spectral stability of the fixed points of (6.7) is investigated numerically for values $\epsilon \in (0, 1)$. The cases of $\epsilon = 0$ and $\epsilon = 1$ are singular, with either the head or the tail link becoming negligible. The stability analysis of fixed points of (6.6) shows dependence on the parameters $\epsilon$ and the total energy $E$, with bifurcations occurring as the parameters change. The following sections contain a detailed analysis of fixed points of (6.6). The fixed points and their

stability are summarized in Table 6.1.

| $k_1, k_2$ | Case | Nonisolated Fixed Points | $\lambda(D\mathbf{f}_R(E(u^*);\omega_1^*,\omega_2^*,\delta^*))$ | Path |
|---|---|---|---|---|
| | 1 | $u^e(E) > 0, \omega_1^e = 0, \omega_2^e = 0, \delta^e = 0$ | $[-a_{1,1}, -a_{1,2}, -a_{1,3}]$ (S/U) | Line |
| $k_1 > 0$ | 2 | $u^e(E) < 0, \omega_1^e = 0, \omega_2^e = 0, \delta^e = 0$ | $[a_{2,1}, a_{2,2} + a_{2,3}i, a_{2,2} - a_{2,3}i]$ (U) | Line |
| $k_2 \geq 0$ | 3 | $u^*(E) > 0, \omega_1^*(E), \omega_2^* = 0, \delta^*$ | $[-a_{3,1}, \pm a_{3,2} - a_{3,3}i, \pm a_{3,2} + a_{3,3}i]$ (S/U) | Circle |
| | 4 | $u^*(E) < 0, \omega_1^*(E), \omega_2^e* = 0, \delta^*$ | $[a_{4,1}, -a_{4,2} - a_{4,3}i, -a_{4,2} + a_{4,3}i]$ (U) | Circle |
| | 5 | $u^e(E) > 0, \omega_1^e = 0, \omega_2^e = 0, \delta^e = 0$ | $[a_{5,1}, -a_{5,2}, -a_{5,3}]$ (U) | Line |
| | 6 | $u^e(E) < 0, \omega_1^e = 0, \omega_2^e = 0, \delta^e = 0$ | $[a_{6,1}, -a_{6,2}, a_{6,3}]$ (U) | Line |
| $k_1 < 0$ | 7 | $u^e(E) > 0, \omega_1^e = 0, \omega_2^e = 0, \delta^e \in \{\delta_1, \delta_2\}$ | $[-a_{7,1} + a_{7,2}i, -a_{7,1} - a_{7,2}i, -a_{7,3}]$ (S/U) | Line |
| $k_2 > 0$ | 8 | $u^e(E) < 0, \omega_1^e = 0, \omega_2^e = 0, \delta^e \in \{\delta_1, \delta_2\}$ | $[a_{8,1} + a_{8,2}i, a_{8,1} - a_{8,2}i, a_{8,3}]$ (U) | Line |
| | 9 | $u^*(E) > 0, \omega_1^*(E), \omega_2^e = 0, \delta^*$ | $[-a_{3,1}, \pm a_{3,2} - a_{3,3}i, \pm a_{3,2} + a_{3,3}i]$ (S/U) | Circle |
| | 10 | $u^*(E) < 0, \omega_1^*(E), \omega_2^e = 0, \delta^*$ | $[a_{10,1}, \pm a_{10,2} - a_{10,3}i, \pm a_{10,2} + a_{10,3}i]$ (U) | Circle |
| $k_1 = 0$ | 11 | $u^e(E) > 0, \omega_1^e = 0, \omega_2^e = 0, \forall \delta$ | $[0, 0, -a_{11,1}]$ (U) | Line |
| $k_2 = 0$ | 12 | $u^e(E) < 0, \omega_1^e = 0, \omega_2^e = 0, \forall \delta$ | $[0, 0, a_{12,1}]$ (U) | Line |
| | 13 | $u^*(E) > 0, \omega_1^*(E), \omega_2^e = 0, \delta^*$ | $[-a_{13,1}, a_{13,2} - a_{13,3}i, a_{13,2} + a_{13,3}i]$ (U) | Circle |
| | 14 | $u^*(E), 0, \omega_1^*(E), \omega_2^e = 0, \delta^*$ | $[a_{14,1}, -a_{14,2} - a_{14,3}i, -a_{14,2} + a_{14,3}i]$ (U) | Circle |

Table 6.1: Fixed points of the dynamics (8.17) of the sleigh with various spring parameters. The fixed points are denoted by $(u^e, \omega_1^e, \omega_2^e, \delta^e)$ in the case of straight line motion and by $(u^*, \omega_1^*, \omega_2^*, \delta^*)$ in the case of circular motion by the sleigh. Here $u^e(E)$ is given by (6.5), $\omega_1^*$ is given by (6.9), $u^*$ is given by (6.10) and $\delta^* = \cos^{-1}\left(\frac{-mb}{m_r a}\right)$. In cases 1, 3, 7 and 9, where there are multiple fixed points, $(u^e, \omega_1^e, \omega_2^e, \delta^e)$, some of are stable and some are unstable which are indicated by (S/U). The fourth column shows nature of the eigenvalues of the Jacobian of the reduced system (8.12). The notation employed is that each $a_{j,k} > 0$ corresponds to the $j$'th case for $j = 1, 2, 3$ and $i = \sqrt{-1}$. The letter (U) indicates that the fixed point is unstable for all values of $E$ and $\epsilon$.

## 6.2 Motion Along a Line

The first category of equilibrium motion of the sleigh is motion along a straight line in $x - y$ plane (cases 1, 2, 5, 6, 7 and 8 in Table 6.1). Inspecting (8.17) these fixed points are such that $\omega_1^e = 0$, $\omega_2^e = 0$. The value of $\delta^e$ is given by the third equation of (8.17), $-2k_1\delta - 4k_2\delta^3$. When $k_1 > 0$ and $k_2 \geq 0$ this implies $\delta^e = 0$. When $k_1 < 0$ and $k_2 > 0$ however, three fixed points exist for $\delta^e \in \{0, \delta_1, \delta_2\}$ where $\delta_1$ and $\delta_2$ are the minima of the elastic potential, $\delta_{1,2} = \pm\sqrt{-\frac{k_2}{k_1}}$. These are the same fixed points for the reduced system, (8.12).

A sample trajectory for the sleigh converging to a straight line motion (case 1 with $\sigma < 0$) is shown in Fig. 6.1. In Fig. 6.1a the trajectory of the sleigh in the plane converges to a straight line whose slope is determined by the transient dynamics. The straight line motion is indicated in Figs. 6.1b and 6.1c as the longitudinal velocity, $u(t)$ converges to the equilibrium value $u^e > 0$ and the angular velocities, $\omega_1$ and $\omega_2$ converge to zero.

57
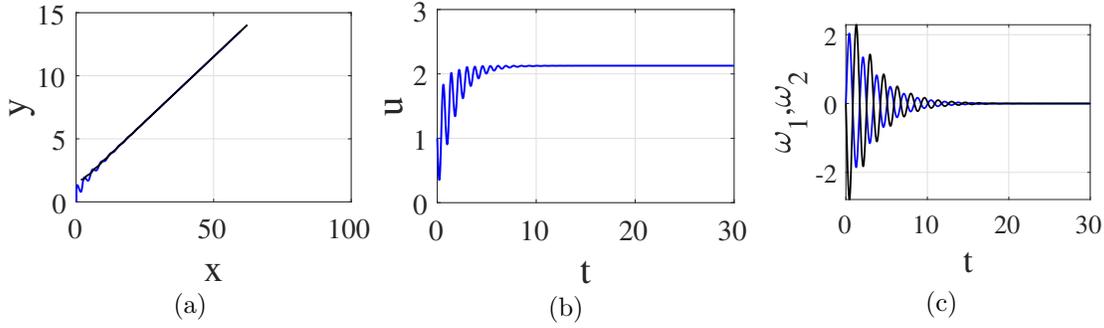
Figure 6.1: Trajectory of the sleigh when $\epsilon = 0.3$ for case 1. Other parameters are $K = 1$, $k_1 = 1$, $k_2 = 0$ and $l = 1$. The $(x, y)$ trajectory of the sleigh (blue) and the rotor (black) are showin in (a), the longitudinal velocity in (b). the angular velocities of the sleigh (blue) and rotor (black) in (c).

When $u^e < 0$, in cases 2, 6 and 8, one of the eigenvalues of the Jacobian, $D\mathbf{f}_R(\omega_1^e, \omega_2^e, \delta^e)$ lies in the right half plane, showing that these fixed points are unstable. In cases 1, 5 and 7, the equilibrium velocity of the sleigh is positive, $u^e > 0$. For case 5, when $k_1 < 0$ and $k_2 > 0$ the equilibrium state of $\delta^e = 0$ is unstable. In the remaining two cases, 1 and 7, the eigenvalues of $D\mathbf{f}_R(\omega_1^e, \omega_2^e, \delta^e)$ lie in the left half plane for a range of values of $\epsilon$ and $E$, showing that fixed points are stable. However these stable fixed points undergo bifurcations and loss of stability as the parameter $\epsilon$ changes.

The fixed point in case 1 undergoes a Hopf bifurcation around $\epsilon = 0.707$. The real part of the three eigenvalues (one complex conjugate pair, and a real eigenvalue) of $D\mathbf{f}_R$ evaluated at the fixed point are shown in fig. 6.2a. The fixed point changes stability only once at $\epsilon \approx \frac{1}{\sqrt{2}}$ in the range of $(0, 1)$ when the real part of the complex conjugate eigenvalues becomes positive. The complex conjugate eigenvalues are plotted in fig. 6.2b showing a crossing from the left half to the right half complex plane when $\epsilon \approx \frac{1}{\sqrt{2}}$. Figure 6.2a shows these changing eigenvalues as the parameter $\epsilon$ is varying for an energy of $E = 1$. Numerical simulations show that the critical value of $\epsilon$ varies by less than $10^{-4}$ from 0.707 for $E = (0, 10^6)$.

In case 7, the stability of the fixed point undergoes three changes as the paramter $\epsilon$ varies in the interval $(0, 1)$.The real parts of the three eigenvalues of $D\mathbf{f}_R$ at the fixed point are plotted in Fig. 6.2c. For $\epsilon < 0.349$ the eigenvalues of $D\mathbf{f}_R$ are real with one of them being positive, with the fixed point being a rank-1 saddle. At $\epsilon \approx 0.349$ the fixed point changes stability from a rank-1 saddle to a stable node. A second bifurcation occurs at $\epsilon \approx 0.351$ when the stable node becomes a stable focus. Here two of the distinct real eigenvalues of $D\mathbf{f}_R$ transition to complex conjugates.

This is shown in the inset figure in Fig. 6.2c. A third bifurcation occurs at $\epsilon \approx 0.698$ when the two complex conjugate eigenvalues cross the imaginary axis into the right half of the complex plane.
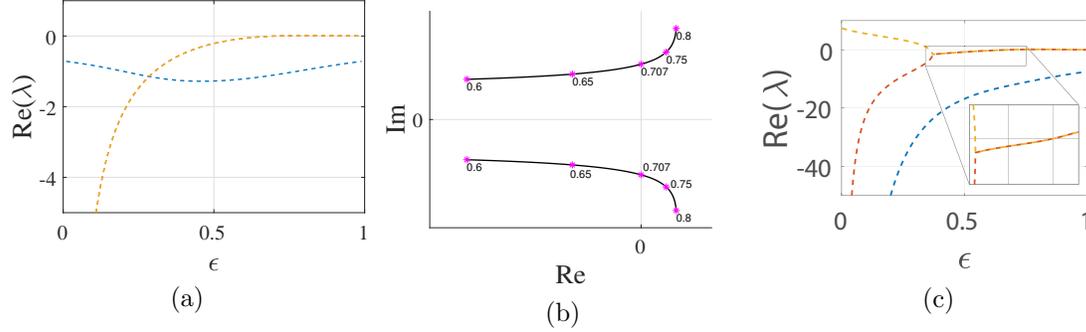


Figure 6.2: (a) Real parts of eigenvalues of $D(\mathbf{f}_R)$ for $\epsilon \in (0,1)$ for case 1 with $k_1 = 1$ and $k_2 = 0$. (b) A pair of eigenvalues crosses the imaginary axis as $\epsilon$ increases for case 1. The numbers on the plots indicate $\epsilon$. (c) Real parts of eigenvalues of $D(\mathbf{f}_R)$ for $\epsilon \in (0,1)$ for case 7 with $k_1 = -7$ and $k_2 = 1$. Other parameters are $K = 1$, $E = 1$ and $l = 1$.

## 6.3   Motion on a Circle

The second category of equilibrium motion of the sleigh is that of a circle in the $x - y$ plane. The fixed points of the dynamical system (8.17) that correspond to this motion are that of cases 3, 4, 9, 10, 13 and 14 in Table 6.1. For these cases the fixed points will be referred to as $\xi^* = (u^*, \omega_1^*, \omega_2^*, \delta^*)$. Inspecting (8.17), $\omega_2^* = 0$ and $\delta^* = \pm \cos^{-1}(\frac{-mb}{m_r a})$ cause all but the third equation to become zero. The existence of $\delta^*$ requires that $\frac{mb}{m_r a} < 1$, that is the internal rotor has to have a larger mass and inertia than the mass of the main body. Due to this feature of the system a bifurcation occurs for all such fixed points such that the fixed point does not exist beyond a value of $\epsilon$ defined by

$$\frac{mb}{m_r a} = \frac{\epsilon}{(1-\epsilon)^2} = 1.$$

Using the fact that $\epsilon \in (0,1)$ we find that this bifurcation occurs at $\epsilon = \frac{3}{2} - \frac{\sqrt{5}}{2} \approx 0.382$. In the alternate physical interpretation of the system, shown in Fig. 8.1b, this implies that the 'tail' is smaller than the main body or the 'head'. Inspecting the third equation of (8.17), we find that equilibrium values $u^*$ and $\omega_1^*$ satisfy

$$0 = -m_r a u^* \omega_1^* \cos \delta^* - m_r ab(\omega_1^*)^2 \sin(\delta^*) - 2k_1 \delta^* - 4k_2 \delta^{*3}. \tag{6.8}$$

The fixed point can be obtained by eliminating $u^e$ from (6.8) using (6.4). This gives

$$\omega_1^* = \pm\sqrt{\frac{A \pm \sqrt{B}}{D}}, \quad \text{where} \tag{6.9}$$

$$A = am_r(\delta^4 k_2 + \delta^2 k_1 - E)(\cos(\delta))^2 + 4\,\delta\,\sin(\delta)(\delta^2 k_2 + 1/2\,k_1)m_r a\cos(\delta)$$
$$+ 4\,bm\delta\,\sin(\delta)(\delta^2 k_2 + 1/2\,k_1)$$

$$B = (a^2 m_r{}^2(\delta^4 k_2 - 4\,\delta^3 k_2 + \delta^2 k_1 - 2\,\delta\,k_1 - E)(\delta^4 k_2 + 4\,\delta^3 k_2 + \delta^2 k_1 + 2\,\delta\,k_1 - E)(\cos(\delta))^2$$
$$+ (8\,am_r(\delta^4 k_2 + \delta^2 k_1 - E)\sin(\delta) - 32\,bm\delta\,(\delta^2 k_2 + 1/2\,k_1))\delta\,(\delta^2 k_2 + 1/2\,k_1)m_r a\cos(\delta)$$
$$- 16\,\delta\,(-1/2\,abmm_r(\delta^4 k_2 + \delta^2 k_1 - E)\sin(\delta) + \delta\,(\delta^2 k_2 + 1/2\,k_1)(-a^2 m_r{}^2 + a^2 mm_r$$
$$+ m(mb^2 + I_c + I_r)))(\delta^2 k_2 + 1/2\,k_1))(\cos(\delta))^2$$

$$D = m_r((a^2 m_r + I_c + I_r)(\cos(\delta))^2 + 2\,\cos(\delta)abm_r + mb^2)a$$

Once $\omega_1^*$ is calculated, $u^*$ can be calculated using (6.8) to get

$$u^* = -\frac{abm_r\omega_1^{*2}\sin(\delta^*) + 4\,k_2\delta^{*3} + 2\,k_1\delta^*}{am_r\omega_1^*\cos(\delta^*)}. \tag{6.10}$$



(a)  (b)  (c)  (d)
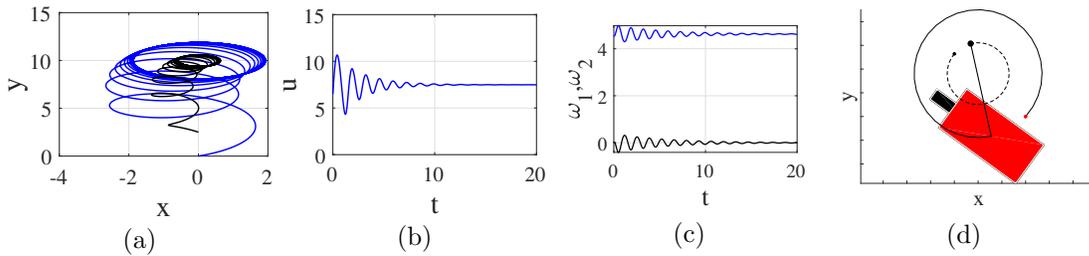
Figure 6.3: Sleigh trajectory converges to motion on a circle (case 9 with $\sigma < 0$). Parameters are $\epsilon = 0.35$, $K = 1$, $k_1 = -7$, $k_2 = 1$ and $l = 1$. The trajectory of the sleigh (blue) and the rotor (black) are shown in (a), the longitudinal velocity in (b). the angular velocities of the sleigh (blue) and rotor (black) in (c). (d) The sleigh traces out a circular path, in cases 3 and 9, with the relative angle between the rotor and the sleigh being constant, $\delta^*$. The dashed line shows the path of the unbalanced rotor and the solid line shows the path of the sleigh.

In order to determine the path of the sleigh in the $x - y$ plane, first note the fact that there

60

is no relative motion between the rotor and the sleigh body, $\delta(t) = \delta^*$, and the sleigh moves with a constant velocity $u^*$ and $\omega_1^*$. Therefore $\theta(t) = \omega_1^* t$ and we can substitute these values into the equations of a point on a circle to get

$$\dot{x} = A\cos(\omega_1^* t + \phi), \text{ and } \dot{y} = A\sin(\omega_1^* t + \phi) \quad \text{where}$$
$$A = \sqrt{u^{*2} + b^2\omega_1^{*2}} \text{ and } \phi = \tan^{-1}(\frac{u}{b\omega_1^*})$$

Integrating these we have

$$x - x_c = \frac{A}{\omega_1^*}\sin(\omega_1^* t + \phi), \text{ and}$$
$$y - y_c = -\frac{A}{\omega_1^*}\cos(\omega_1^* t + \phi).$$

Therefore we get

$$(x - x_c)^2 + (y - y_c)^2 = \frac{A^2}{\omega_1^{*2}} = \left(\frac{u^*}{\omega^*}\right)^2 + b^2,$$

clearly the sleigh's path is a circle of radius $\sqrt{\left(\frac{u^*}{\omega^*}\right)^2 + b^2}$. An example of the simulation of the sleigh's motion in case 9 is shown in Fig. 6.3a trajectory of the sleigh converging to motion on a circle with the trajectory of the sleigh in blue and that of the rotor in black. In this case $\omega_1 \to \omega^*$, $u(t) \to u^*$ and $\omega_2 \to 0$ (Fig. 6.3c). Consequently, the angle of the sleigh grows at a linear rate proportional to $\omega^*$ and $\delta \to \delta^*$. The equilibrium circular path of the sleigh is shown in 6.3d.

We find that for any given energy where the fixed point exists there are eight fixed points $\xi^* = (u^*, \omega_1^*, \omega_2^*, \delta^*)$ due to the positive and negative values of $\delta^*$ as well as the four solutions of (6.8) for $(u^*, \omega^*)$. As we vary the energy, the location of each such fixed points in the $(u, \omega_1)$ plane changes. Different $(u^*, \omega_1^*)$ are shown in Fig. 6.4a for energies ranging from 4.7 to 300 and a representative value of $\epsilon = 0.35$. The stability for these fixed points varies depending on the energy as well as the stiffness values $k_1$, $k_2$. This is seen in Fig. 6.4b where we fix the energy and vary the stiffness. Red regions are where the fixed point does not exist. The blue parameter regions are where the fixed point $\xi^*$ exists but is unstable and green regions are where the fixed point, $\xi^*$ is stable.

As expected, the dynamics are symmetric about the $\omega_1$ axis due to the symmetry in rotational dynamics. We can identify eight unique branches of fixed points $(\xi_1^*, .., \xi_8^*)$ beginning from $E \approx 4.7$, four with $u^* > 0$ (case 9) and four with $u^* < 0$ (case 10). We can take $(\xi_1^*, .., \xi_4^*)$ to be the

61
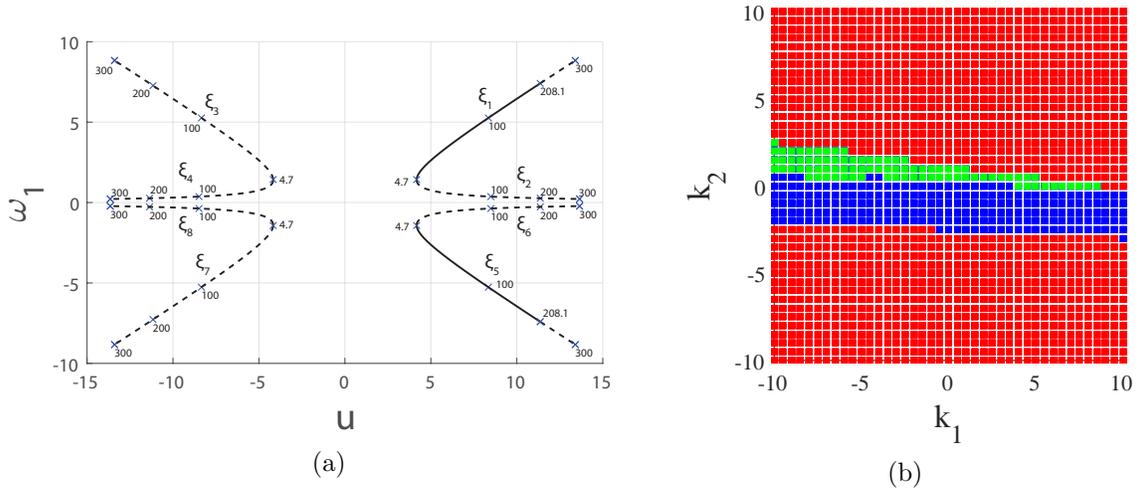
Figure 6.4: (a) Fixed points $\xi^*$ (case 9) in the plane of $u$ and $\omega_1$ for energies ranging from 4.7 to 300. Here $\delta = \delta^*$, $\omega_2 = 0$, $k_1 = -7$, $k_2 = 1$, and $\epsilon = 0.35$. Solid lines indicate stable fixed points and dotted lines are unstable foci. These fixed points do not exist for energies lower than 4.7. Numbers on the plot indicate the energy for different points of interest. (b) Existence and stability of the $\xi^*$ fixed point for various values of $k_1$ and $k_2$ with a fixed energy of $E = 100$. Either the fixed point does not exist (red), it exists but is unstable (blue) or it exists and it stable (green).

four branches in the top half plane ($\omega_1 > 0$). Let $\xi_1^*$ refer to the branch with higher $\omega_1^*$ for $u^* > 0$ in the first quadrant of Fig. 6.4a and let $\xi_2^*$ be the other branch with $u^* > 0$ in the first quadrant. Figure 6.4a shows the result of a numerical computation of the stability, and it can be see that for the given parameters $\xi_1^*$ is stable for low energies and becomes unstable for higher energies. For this value of $\epsilon = 0.35$ we also find that the branch $\xi_2^*$ is unstable for all energies. The other two branches are unstable due to the negative value of $u^*$. In Fig. 6.5 we investigate the stability of $\xi_2^*$ as a function of epsilon. We see in Fig. 6.5b that when we fix the energy and vary epsilon, $\xi_2^*$ is stable for lower values of $\epsilon$ and becomes unstable after $\epsilon = 0.2$. A plot of $(\xi_1^*, .., \xi_2^*)$ is shown in Fig. 6.5a for $\epsilon = 0.1$. We find that the general shape and stability of the branches changes as we vary $\epsilon$.

Consider $k_1 = -7$, $k_2 = 1$ and take $\xi_1^*$ in the first quadrant of Fig. 6.4a for an energy of $E = 100$. The eigenvalues of $D\mathbf{f}$ in this case are of the form $\lambda = [-a_{9,1}, -a_{9,2} - a_{9,3}j, -a_{9,2} + a_{9,3}j]$, therefore $\sigma < 0$ making $\xi_1^*$ is a stable focus at this point. In Fig. 6.6a we see convergence to three different stable fixed points (one for case 7 and case 9 fixed points $\xi_1^*$ and $\xi_5^*$) for different initial conditions at three constant energies ($E = 80, 100, 120$). The fixed points are shown as a function of energy with black lines. The trajectories corresponding to case 7 converge to the $\omega_1 = 0$ axis and the trajectories converging to circular motion in case 9 are symmetrically placed around this fixed

62
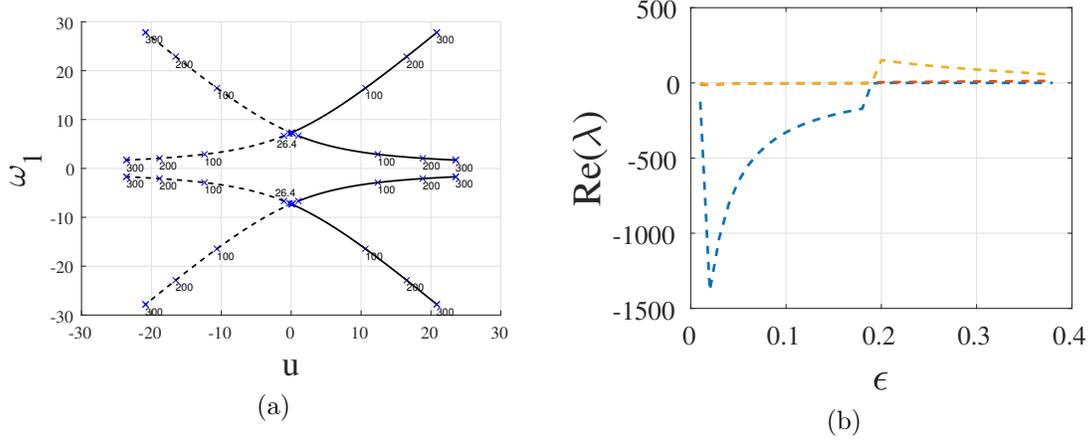
Figure 6.5: (a) Fixed points $\xi^*$ (case 9) in the plane of $u$ and $\omega_1$ for energies ranging from 4.7 to 300. Here $\delta = \delta^*$, $\omega_2 = 0$, $k_1 = -7$, $k_2 = 1$ and $\epsilon = 0.1$. Solid lines indicate stable fixed points and dotted lines are unstable foci. These fixed points do not exist for energies lower than 4.7. Numbers on the plot indicate the energy for different points of interest. (b) Real eigenvalues as a function of $\epsilon$ when the energy is $E = 700$

point at $\pm\omega_1^*$. All three fixed points are stable for the three energy levels shown. This figure shows that for any given energy cases 7 and 9 can both be stable simultaneously with asymptotic behavior of trajectories being dependent on initial conditions.

As the energy $E$ increases $\sigma$ changes sign and $\xi_1^*$ becomes locally unstable. The eigenvalues of $D\mathbf{f}$ cross the imaginary axis into the right half plane at $E = 208.1$, (Fig. 6.6c). A stable limit cycle is formed around the unstable fixed point in a supercritical Hopf bifurcation. This is clearly shown in Fig. 6.6b where we see how the fixed point $\xi_1^*$ is at first a stable focus for energies of $E = 180$ and 200 and a stable limit cycle is formed around it for higher energies of $E = 220$ and $E = 240$. Note that the limit cycle is present in four dimensions. That is $\omega_2$ and $\delta$ also converge to periodic functions.

In order to identify other bifurcations the fixed point $\xi^*$ may undergo we vary $\epsilon \in (0, 0.382)$ and plot the complex eigenvalues of $D\mathbf{f}_R(\xi_1^*)$ of case 9 as well as a fixed point of the same energy for case 3. As $\epsilon$ is varied, holding the energy constant, the stability of these fixed points does not change for energies below $E \approx 520$. However for higher energies, we find a double Hopf bifurcation where the complex eigenvalues cross the imaginary axis twice as $\epsilon$ is varied. This is seen in Figs. 6.7(a) and 6.7(b) where we vary $\epsilon$ for cases 3 and 9 respectively. We find that both cases undergo a similar bifurcation for an energy of $E = 700$. In case 9, the imaginary eigenvalues of $\mathbf{f}_R$ cross the imaginary axis from left to right near $\epsilon = 0.25$ and then in the opposite direction at $\epsilon = 0.36$. Before the first

63
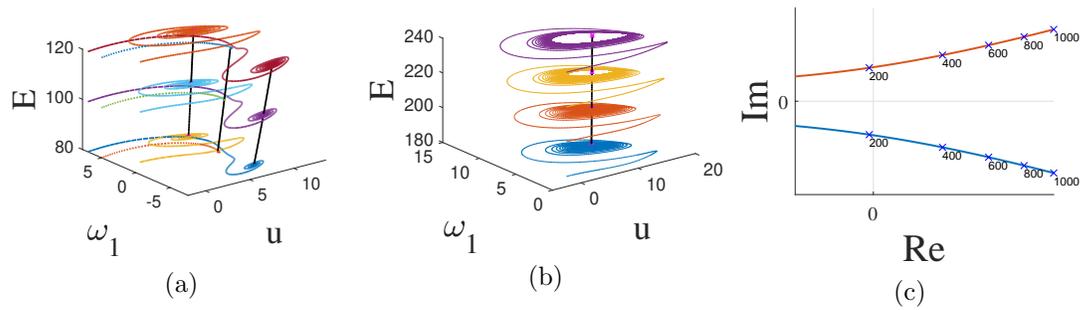
Figure 6.6: (a) Three stable trajectories of the sleigh corresponding to cases 7 and 9 with $\sigma < 0$ at energies of $E = 80$, $E = 100$, and $E = 120$. Initial conditions are chosen to lie on the corresponding energy level and the trajectory is plotted in the $(u, \omega_1, E)$ space. The fixed points as functions of energy are shown by the black lines. The trajectory where $\omega \to 0$ corresponds to case 7 and the trajectories to either side correspond to case 9 with symmetrically placed fixed points at $\pm\omega^*$ ($\xi_1$ and $\xi_5$ in Fig. 6.4a). (b) Fixed point $\xi_1^*$ goes from being stable to unstable and a stable limit cycle is formed around it (case 9 with transition from $\sigma < 0$ to $\sigma > 0$ as we vary energy). Convergence to the stable focus is shown for energies $E = 180$ and $E = 200$ and convergence to a stable limit cycle is seen for $E = 220$ and $E = 240$ (c) Eigenvalues cross the imaginary axis and a supercritical Hopf bifurcation occurs at an energy of $E = 208.1$. Other parameters are $\epsilon = .35$, $k_1 = -7$, $k_2 = 1$, $K = 1$, $m = 1$, and $l = 1$

transition $\xi^*$ is a stable focus. After the first crossing the point becomes unstable and a stable limit cycle is created around the fixed point, but as we increase $\epsilon$ further the fixed point becomes a stable focus once again.
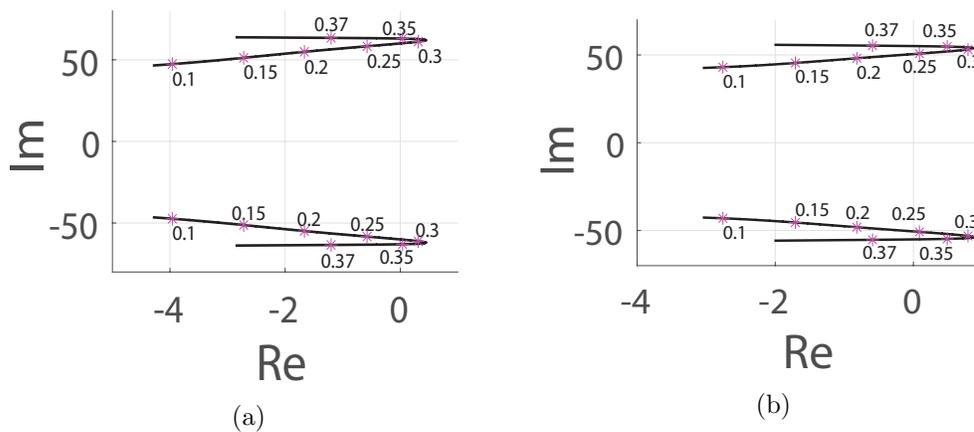


Figure 6.7: Eigenvalues cross the imaginary axis as we vary $\epsilon$ for case 3 (a) and case 9 (b). The numbers on the eigenvalues show $\epsilon$ at select values. In (a) the energy is $E = 1000$ with $k_1 = 0$ and $k_2 = \frac{1}{4}$ and in (b) the energy is $E = 600$ with $k_1 = -\frac{7}{2}$ and $k_2 = \frac{1}{4}$.

64

## 6.4 Dynamics of the System with no Elastic Element

If the spring element between the rotor and the sleigh's body is absent, the rotor is free to spin without any restoring torque. The fixed points for the case $k_1 = 0$ and $k_2 = 0$ correspond to cases 11-14 in Table 6.1. Two of these cases correspond to straight line motion and two to circular motion. However two of the eigenvalues of the $D\mathbf{f}_R$ are zero in case 11, where $u^e > 0$. Here a linearized analysis of stability is insufficient. However extensive numerical simulations have shown that fixed point in case 11 is unstable. The fixed points in the other cases 12-14 are similarly unstable. The solutions to the dynamical system (8.17) converge to a chaotic attractor. For a thorough analysis of this case for a small rotor, we refer readers to [22].

# Chapter 7

# Passive Degrees of Freedom for Improving Locomotion

In this chapter we show that the Chaplygin sleigh with an internal degree of freedom is able to achieve much higher velocities and efficiency of motion for the same inputs as the sleigh without one. We are able to compare the systems by assuming the total mass of the systems is the same, with the same location of the overall center of mass and same moment of inertia when the interlink angle $\delta = 0$. This is shown in Figure 7.1. The relative size of the two links once an internal joint is introduced is quantified by parameter $\epsilon$ which represents the size of the tail link.
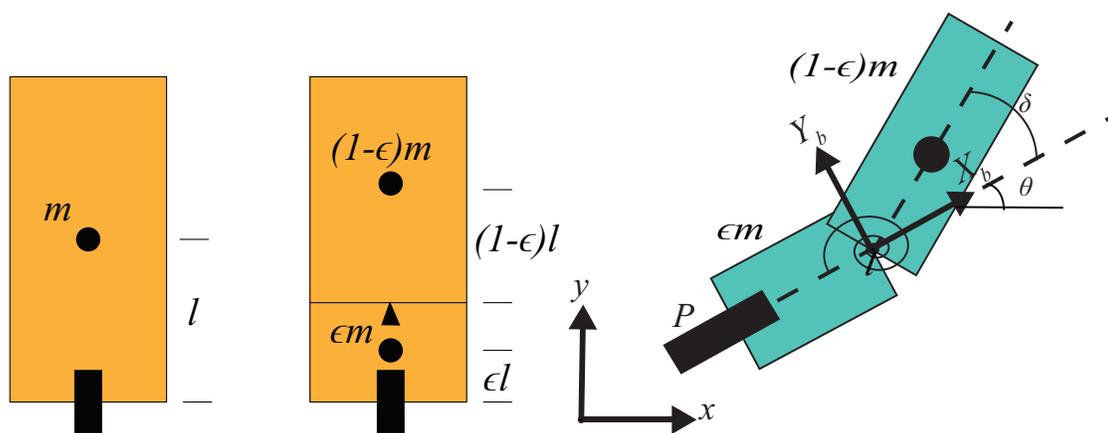


Figure 7.1: Chaplygin sleigh (left) and Chaplygin sleigh with internal degree of freedom (right)

For many cases the moment of inertia of the sleigh may be written as $I = \gamma m (a^2 + b^2)$ where

$\gamma$ is a parameter that determines the shape of the sleigh and $a$ and $b$ are some characteristic lengths. Since we assume the sleigh to be of uniform rectangular shape, the moment of inertia of the sleigh without a passive degree of freedom is taken to be $I = \frac{1}{12}m(l^2 + (2l)^2) = \frac{5}{12}ml^2$. The moments of inertia for the two link system are similarly calculated. As before we represent the dynamics of the two link system using $u$, the velocity of the nonholonomic wheel, the angular velocity of the tail link $\omega_1 = \dot{\theta}$, and the relative angular velocity $\omega_2 = \dot{\delta}$ and the relative angle $\delta$.

## 7.1   Dynamics of two link sleigh with periodic forcing

In order to facilitate the comparison between the systems we nondimensionalize the equations of motion with respect to lengths and mass so that there are less parameters to consider. This is accomplished with the change of variables and parameters

$$u \to ul, \quad A \to Aml^2, \quad K \to Kml^2, \quad c_\omega \to c_\omega l^2, \quad c_\delta \to c_\delta l^2$$

where $K$ is the spring constant for the sleigh with a passive degree of freedom. We also introduce dissipation in $u$, $\omega$ ($\omega_1$ for the two link system) and the interlink angle $\delta$. The dissipation coefficients are $c_u$, $c_\omega$ and $c_\delta$ respectively.

The nondimensional equations of motion for the Chaplygin sleigh become

$$\dot{u} = \omega^2 - c_u u$$

$$(5\gamma + 1)\dot{\omega} = -u\omega + A\cos(\Omega t) - c_\omega \omega$$

67

and the equations of motion for the sleigh with a passive degree of freedom and spring are

$$
\begin{bmatrix}
1 & -\sin(\delta)(\epsilon-1)^2 & -\sin(\delta)(\epsilon-1)^2 \\
-\sin(\delta)(\epsilon-1)^2 & \mathcal{M}_{2,2} & \mathcal{M}_{2,3} \\
-\sin(\delta)(\epsilon-1)^2 & \mathcal{M}_{2,3} & \mathcal{M}_{3,3}
\end{bmatrix}
\begin{bmatrix}
\dot{u} \\
\dot{\omega_1} \\
\dot{\omega_2}
\end{bmatrix}
=
$$

$$
\begin{bmatrix}
(\omega_2+\omega_1)^2(\epsilon-1)^2\cos(\delta)+(-2\epsilon+3)\epsilon\,\omega_1{}^2-c_u u \\
3\epsilon\,(2\omega_1+\omega_2)(\epsilon-1)^2\,\omega_2\sin(\delta)-\omega_1 u(\epsilon-1)^2\cos(\delta)+(2\epsilon-3)\omega_1 u\epsilon-c_\omega\omega_1 \\
-\omega_1 u(\epsilon-1)^2\cos(\delta)-3\,\omega_1{}^2\epsilon(\epsilon-1)^2\sin(\delta)-K\,\delta-\omega_2 c_\delta+A\,\cos(\Omega t)
\end{bmatrix}
$$

where

$$
\mathcal{M}_{2,2} = 6\,\epsilon\,(\epsilon-1)^2\cos(\delta)-9\,\epsilon^3+(12\,\gamma+12)\epsilon^2+(-12\,\gamma-3)\epsilon+5\,\gamma+1
$$

$$
\mathcal{M}_{2,3} = -(\epsilon-1)(4\,\epsilon^2\gamma-3\,\epsilon^2\cos(\delta)-8\,\epsilon\,\gamma+3\,\epsilon\,\cos(\delta)+\epsilon^2+5\,\gamma-2\,\epsilon+1)
$$

$$
\mathcal{M}_{3,3} = -(\epsilon-1)\left(4\,\epsilon^2\gamma+\epsilon^2-8\,\epsilon\,\gamma-2\,\epsilon+5\,\gamma+1\right)
$$

With the above dynamic equations we observe a range of behaviors, both regular and chaotic. The trajectory of the sleigh for a nonzero torque can be of three primary types: converging to a limit cycle such that the sleigh moves in a straight line on average similar to the one link sleigh, converging to a limit cycle such that the sleigh moves on a circle on average, or a chaotic trajectory. An example of each of the three types is shown in Fig. 7.2.

The trajectory where the sleigh travels on a circle (Fig. 7.2 (b)) arises from oscillations about the $\delta^*$ fixed point discussed in Chapter 6. Similar as with the sleigh with no forcing, the type of motion exhibited by the sleigh can depend just on the initial conditions. For the first two types of motion, we see a limit cycle in the velocity space (Fig. 7.2 (d-e)) similar to one seen for the classical sleigh. For the straight line motion, the limit cycle is such that $\int_{t_0}^{t_0+T}\omega dt = 0$. For motion on a circle $\int_{t_0}^{t_0+T}\omega dt \neq 0$ but as shown in Chapter 4 such motion can also be predicted via harmonic balance method.

68
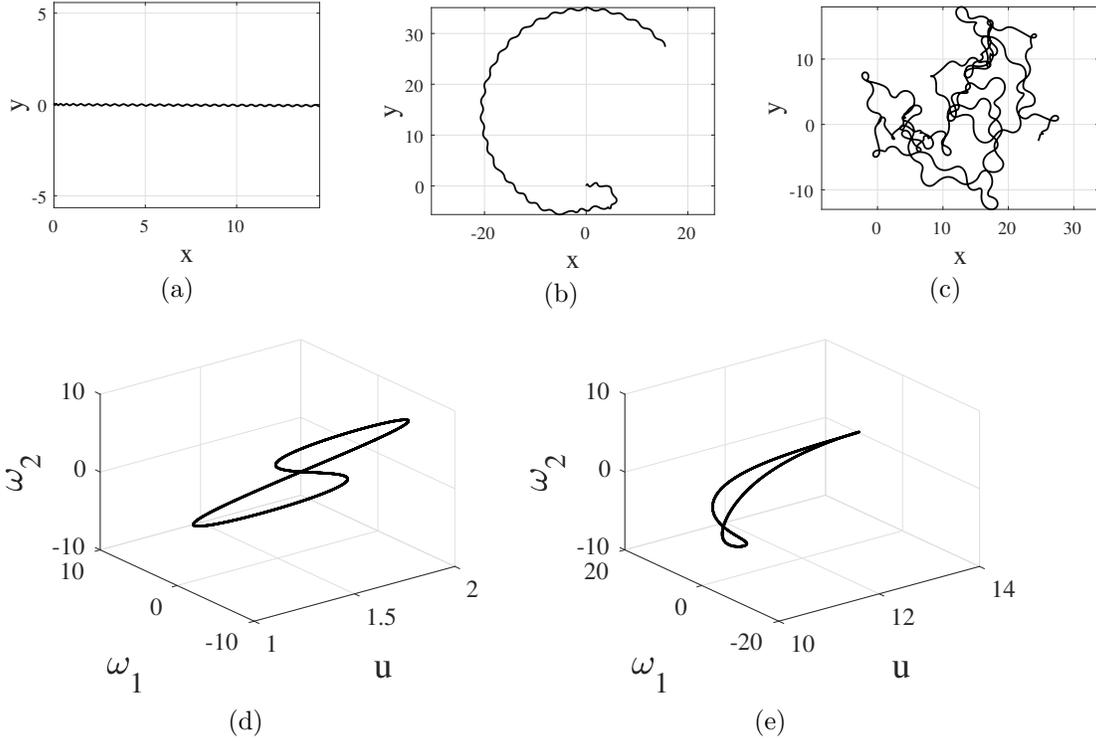
Figure 7.2: Sample trajectories of the Chaplygin sleigh with a passive degree of freedom. The paths in the $(x, y)$ plane are shown for (a) $A = 15$, $\Omega = 20$ (b), $A = 50$, $\Omega = 20$ and (c) $A = 100$, $\Omega = 20$. Initial conditions are all zero.

## 7.2  Efficiency Comparison

To compare the sleigh with a degree of freedom without one, we calculate the efficiency of motion for the three systems over a range of amplitudes and frequencies. The efficiency of motion may be defined as

$$\mu = \frac{\frac{1}{2}mv_{net}^2}{E_{in}}$$

The efficiency of the Chaplygin sleigh without a degree of freedom is plotted for amplitudes up to 200 and frequencies up to 50 in Fig. 7.4 (a). Note that efficiency of motion is maximized for a particular set of of torque inputs. As also shown in Chapter 3, the velocity of the sleigh decreases for large amplitudes due to self-enclosing trajectories. Note that efficiency is maximized at a lower amplitude than $v_{net}$. The magenta line in each of the three plots represents a level set of input energy when $\mu = \max \mu$. We compare the two systems using the level set of energy which produces

69
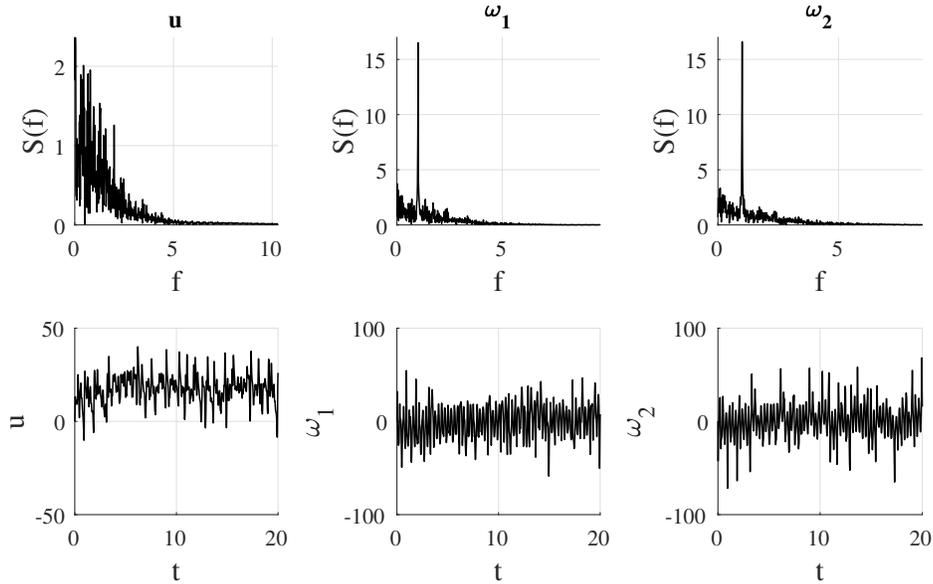
Figure 7.3: Power spectrum density plot for the Chaplygin sleigh with a passive degree of freedom for input $A = 100$, $\Omega = 20$. Parameters are $c_u = 1$, $c_\omega = 1$, $c_\delta = 1$, $\epsilon = 0.1$, and $K = 10$

the highest efficiency for the single link sleigh. Note that for the single link sleigh efficiency is nearly constant for a level set of energy. This means that for a given input energy a particular velocity is achieved regardless of the torque used to achieve this energy. This makes it beneficial to use low frequency inputs as the same velocity and efficiency can be achieved with low torque required by the rotor.

In contrast we see the efficiency for the Chaplygin sleigh with a spring plotted in Fig. 7.5 (a). For this system we see a fundamentally different frequency response. It is important to note that the sleigh with a passive degree of freedom can exhibit a larger range of dynamics including chaos and oscillations about the $\delta^*$ fixed point discussed in Chapter 6. The behavior of the system can change with the parameters as well as input and initial conditions. For this reason we plot the efficiency of the modified system for a lower range of amplitude inputs where only serpentine straight line motions are observed. Such motions can be approximated with the harmonic balance method. We see that the efficiency of motion increases with both frequency and amplitude over a large range of inputs.

Perhaps the most interesting difference between the two systems is in the dynamics on level sets of input energy. Unlike for the single sleigh, for the same input energy we see an increase

www.manaraa.com
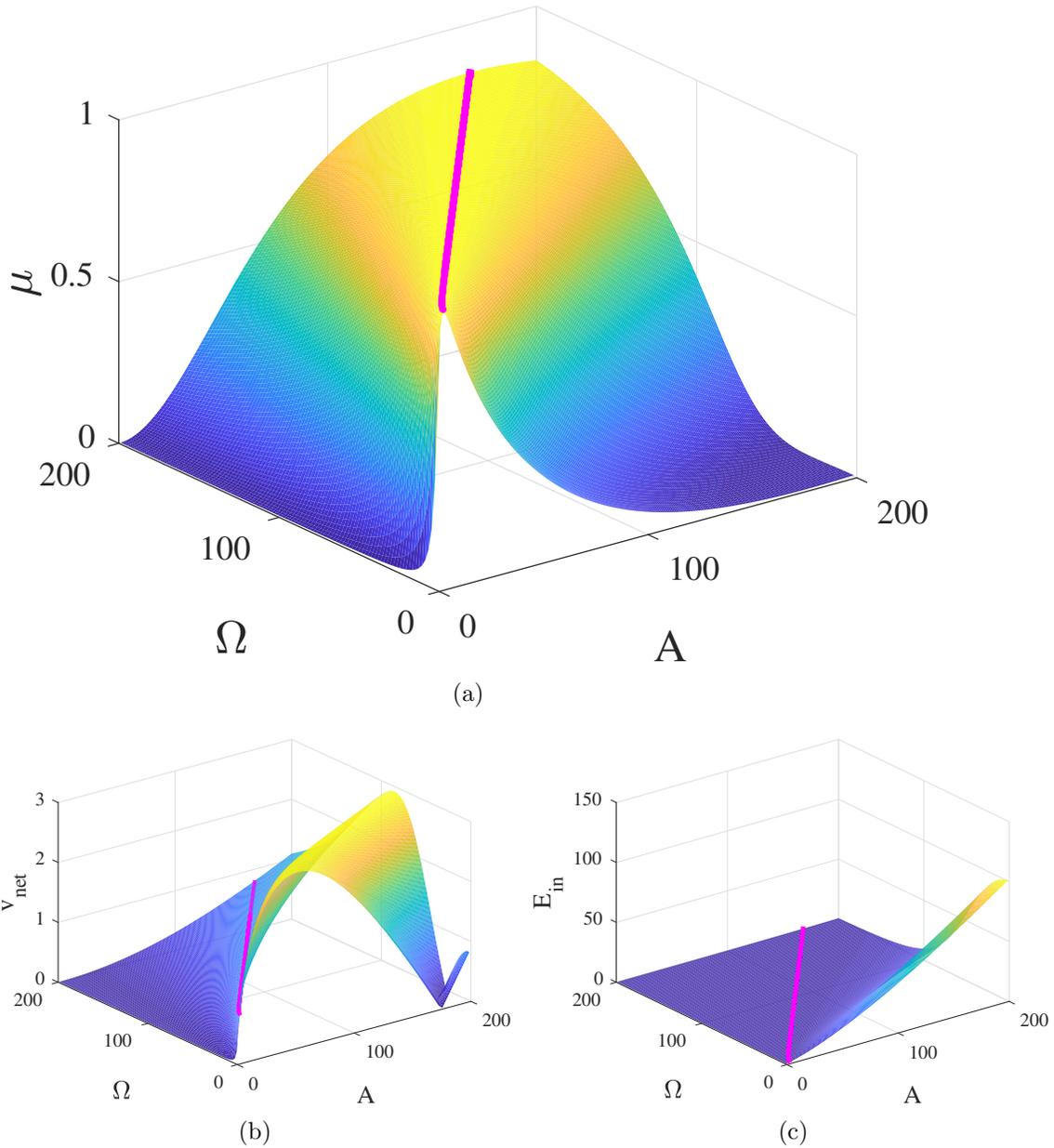
Figure 7.4: Frequency response of Chaplygin sleigh with friction. The magenta line represents the level set of energy $E_{in}|_{\mu=\max\mu}$ (a) Efficiency of motion (b) Average velocity of the sleigh in the $(x, y)$ plane (c) Input energy per time period.

in velocity as higher torque is applied. Although the system may be less efficient for low torque inputs, it can achieve much higher efficiency than its single link counterpart if high torques can be generated. This is shown clearly in Fig. 7.6 where the efficiency and the corresponding velocities are
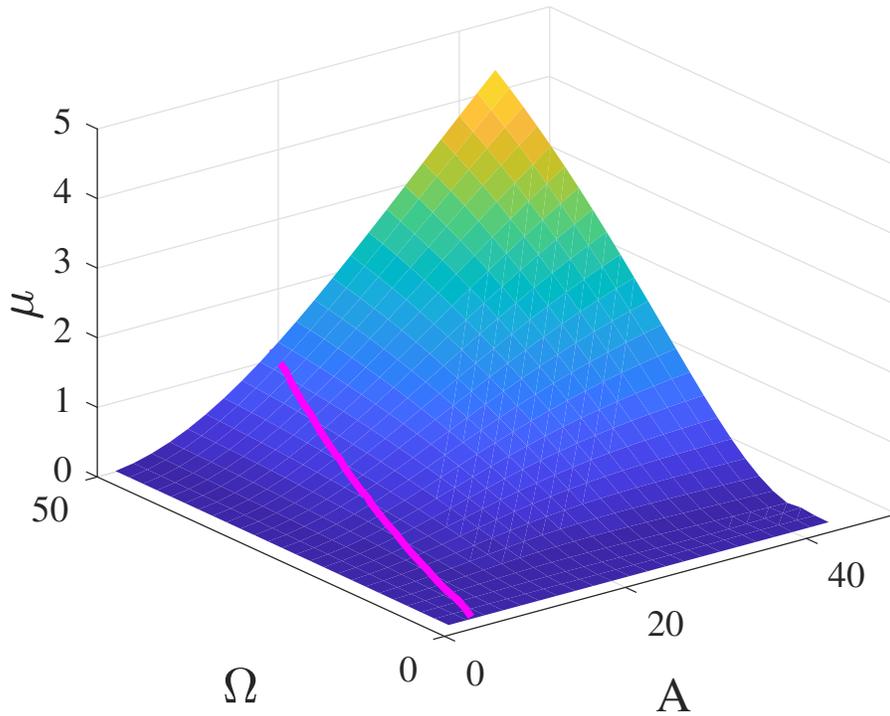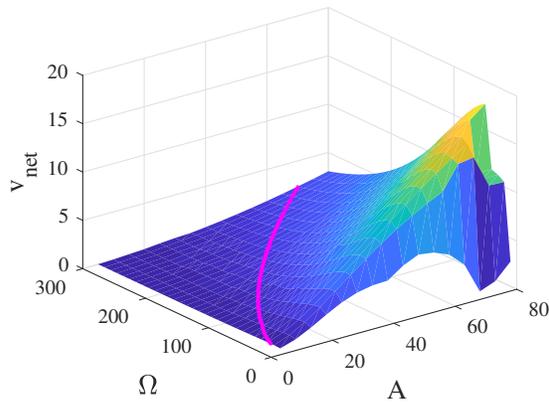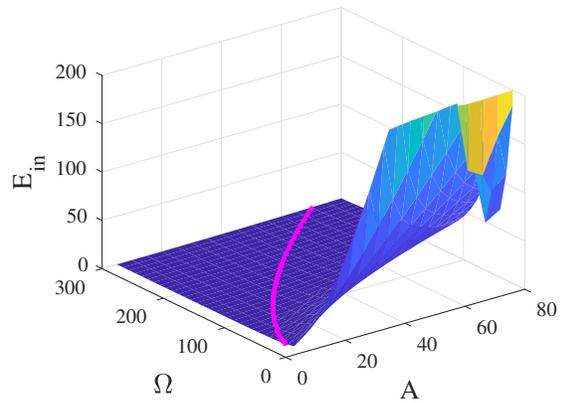
Figure 7.5: Frequency response of Chaplygin sleigh with a passive degree of freedom and friction (a) Efficiency of motion (b) Average velocity of the sleigh in the $(x, y)$ plane (c) Input energy per time period. Parameters are $c_u = 1$, $c_\omega = 1$, $c_\delta = 1$, $\epsilon = 0.1$, and $K = 10$

plotted for two constant energy levels. It is convenient to plot them against input frequency since the amplitude does not change as much for constant energy.

From Fig. 7.6 (a) we see that if a high frequency input can be generated, the sleigh with a
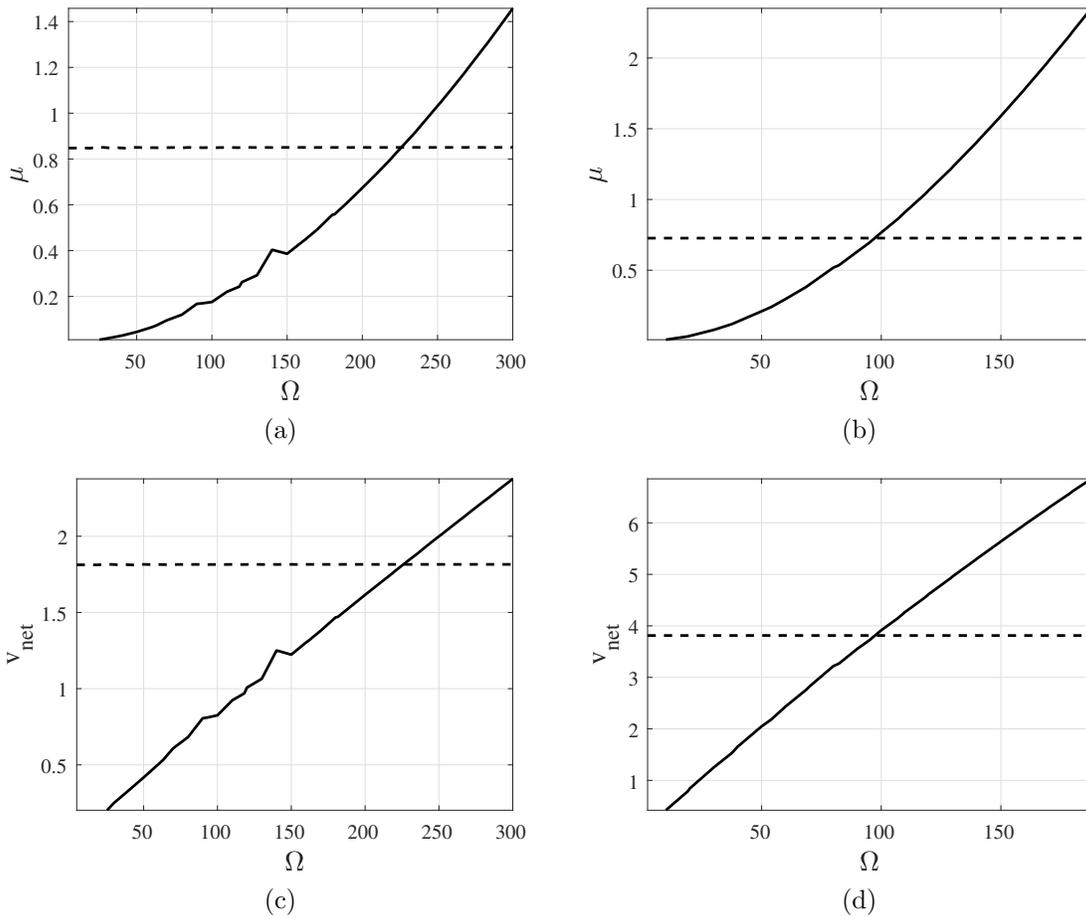
Figure 7.6: Dynamics on constant energy surfaces $E_{in} = E_{in}|_{\mu=\max\mu}$ (left) and $E_{in} = 10$ (right). (a-b) Efficiency of motion (c-d) Average velocity of the sleigh in the $(x, y)$ plane. Parameters are $c_u = 1$, $c_\omega = 1$, $\epsilon = 0.1$, and $K = 10$

passive degree of freedom can move much faster than the sleigh without one. This could motivate the use of vibration motors. In Fig. 7.6 (b), however, we see that for higher energy limit cycles, higher efficiency can be achieved at lower input frequencies. Another interesting thing to note is that for the sleigh with a passive degree of freedom, the velocity of the sleigh appears to increase linearly with respect to the input frequency as seen in Fig. 7.6 (c-d). Efficiency, therefore, increases as $\mu \propto \Omega^2$.

73

# Chapter 8

# Compliance in Nonholonomic Systems

Compliant mechanisms convert an input displacement and force into a displacement and force at another part of the body using elastic body deformations only. Compliant mechanisms have made their way into many common tools and machines from lids, bows and bicycle breaks [34] to end effectors for robotic arms and compliant grippers [1, 16, 19]. In mobile robotics, legged mobile robots have seen the utilization of compliant joints that seek to mimic the compliant joints of animals [33, 37, 52, 73]. Two features of compliant mechanisms stand out from the perspective of their applications to robots, a large number of unactuated or passive degrees of freedom and multiple stable configurations which can be retained with no applied forces [38, 59]. Passive degrees of freedom are naturally utilized by animals to facilitate efficient motion. Examples are the passive flapping of wings by insects to generate lift in hovering flight [21, 82] and passive deformations of fish to extract energy from ambient wake in a stream [65, 72].

While motion in a compliant mechanism is achieved through elastic deformation of the body as opposed to the interaction of rigid bodies, such mechanisms can nevertheless be modeled using rigid links by constructing pseudo rigid body models (PRBM) or rigid body approximations of compliant mechanisms. Such PRBM models have been used extensively in mechanism synthesis. Virtually all theoretical work on the dynamics of compliant mechanisms has subjected them to holonomic constraints alone. However nonholonomic constraints arise naturally in the dynamics of

mobile robots; mainly due to rolling no-slip constraints in wheeled robots.

Another method of introducing compliance in nonholonomic systems is origami. Origami is an ancient art of paper folding. One can create complex 3-D structures and mechanisms by simply folding a 2-D flat sheet along the prescribed fold lines. Fabrication of such complex shapes via traditional manufacturing techniques would indeed be very difficult if not impossible. The principle of origami is geometric and scale-independent, thus one can essentially apply the same design to create micro to macro-scale mechanisms. The absence of bulky rigid linkages in origami makes the resultant mechanism extremely lightweight and simplified. In addition, many origami mechanisms exhibit exceptional properties such as, multi-stability [2, 48, 49, 85], auxetics [48, 74, 85], tunable nonlinear stiffness [29, 47, 48], etc. In particular, a multi-stable system is one which possesses multiple stable equilibrium configurations and perturbations around any equilibrium configuration remain bounded in the absence of external inputs. Each of the stable configurations corresponds to a minima of the potential energy function associated with the mechanism. All these aforementioned properties make origami an attractive candidate for designing novel very high degree of freedom robots and mechanisms. Such origami systems can have many potential applications for robots that can slide, crawl and climb. In all such applications the origami robots would have to contend with nonholonomic constraints.

## 8.1   The Compliant Chaplygin Sleigh Example

In this section we bring together the themes of compliant mechanisms and their associated passive degrees of freedom with the theme of nonholonomic constraints to develop the dynamic model of a nonholonomic bistable planar compliant mechanism. This system can be thought of as a Chaplygin sleigh whose center of mass is able to move along the line joining the center of mass and the point where the velocity constraint is applied. The system is envisioned as being actuated by an internal balanced momentum wheel whose motion exerts a torque on the sleigh. The compliance of the mechanism introduces a passive degree of freedom with a quartic elastic potential. This leads to multiple stable static equilibrium configurations for the system. When the mechanism is subjected to a periodic torque, the result is limit cycle oscillations in a reduced velocity space and serpentine motion in the physical plane results. The limit cycles and the resulting motion of the sleigh are dependent on the amplitude and frequency of the forcing. The stable velocity of the sleigh can also

75

change depending on which potential well the limit cycles are near. This allows the sleigh to be steered in a desired direction by changing the frequency of the input. These findings are relevant to future work on compliant robots with wheels.

### 8.1.1 Pseudo Rigid Body Model (PRBM) of a Compliant Chaplygin Sleigh

Figure 8.1 (a) shows a four link mechanism with three compliant joints. Assuming that the compliant mechanism is always symmetric about the dashed line in Fig. 8.1 (b), the two joints at the rotor are equivalent to a single compliant joint. Such symmetry is maintained if $m_3 = m_4$, for then the constraint force at $m_1$ produces identical deflections about the dashed line. Therefore the equivalent model has a total of two compliant joints one at $m_1$ and one at $m_2$ with stiffnesses $k_1$ and $k_2$ respectively. The mechanism is similar to a Young mechanism [39] in that it consists of two compliant segments and two pin joints, however the two pin joints are opposite to each other, unlike a Young mechanism where they are adjacent. One node in this mechanism has a wheel that cannot slip in the transverse direction. Two casters support the mechanism at the front allowing motion in any direction. The system is modification of the Chaplygin sleigh, which consists of a platform and blade or runner (replaced in our model by a wheel) on one side that is in contact with the ground. The wheel reduces frictional dissipation for motion in the longitudinal direction, and while it does not slip in the transverse direction, it could either roll or slip in the longitudinal direction. A balanced rotor is placed at the joint with the wheel. This rotor is imagined to be driven by a motor at a desired angular velocity. We will further restrict the angular velocity of the rotor to be periodic with a chosen frequency and amplitude.

An equivalent pseudo rigid body model of the system is shown in fig. 8.1(b). The body fixed frame is denoted by $X_b - Y_b$ attached to point $P$, while the spatially fixed frame is denoted by $X - Y$. The body fixed frame makes an angle of $\theta$ with respect to the spatial frame. A vector in the spatial frame $\eta_s$ is related to a vector in the body frame, $\eta_b$ through a rotation transformation $\eta_s = \mathbf{R}\eta_b$ where

$$\mathbf{R} = \begin{bmatrix} \cos\theta & -\sin\theta \\ \sin\theta & \cos\theta. \end{bmatrix}$$

The mass of each of the links is concentrated at the four node points, with masses $m_1, ..., m_4$. The

76
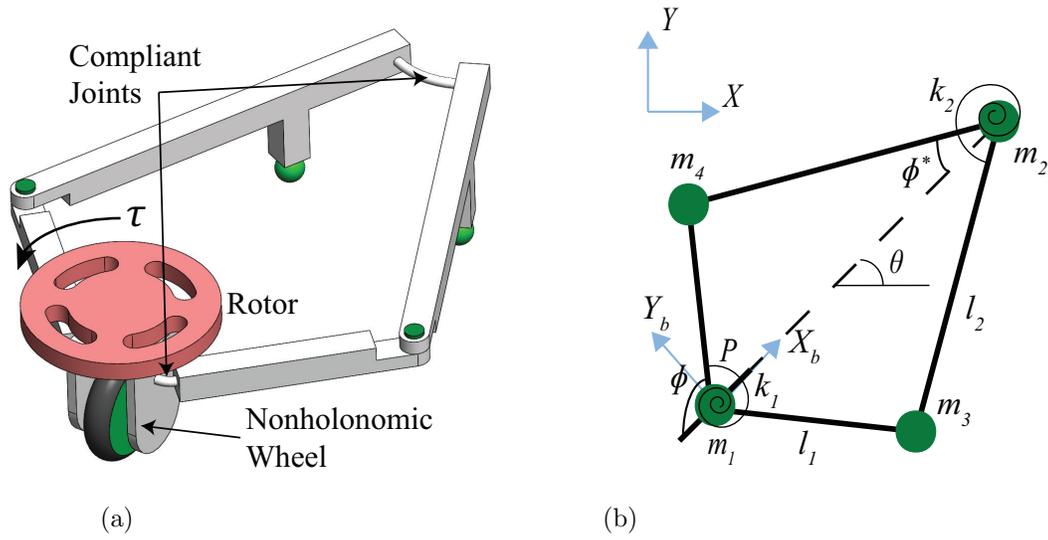
Figure 8.1: The bistable Chaplygin sleigh

choice of concentrating the mass at four nodes does not affect the qualitative behavior of the system as our analysis in will show, only the location of the center of the mass and its motion is important. The particular choice of lumped masses merely reduces the length of the calculations. In this paper we restrict ourselves to the case where the sleigh is balanced about the nonholonomic constraint, i.e. $m_4 = m_3$. The node at which the nonholonomic constraint is applied is denoted by $P$. The configuration of the compliant Chaplygin sleigh is parameterized by the location of the first mass, $(x_1, y_1)$, its orientation $\theta$ and its internal shape variable $\phi$. The joints at $m_1$ and $m_2$ each have a torsional spring of stiffnesses $k_1$ and $k_2$ respectively. The fixed lengths of the links $l_1$ and $l_2$ are not configuration variables but determine the physical shape of the sleigh and potential function. The configuration space of the system is $Q = SE2 \times S^1$, where $G = SE2$ is often defined as the fiber group and the group $S^1$ the shape manifold [7]. The tuple $(x_1, y_1, \theta, \phi)$ will be represented by $q = [q_1, q_2, q_3, q_4]^T$ for convenience. The Lagrangian for the compliant sleigh is

$$\mathcal{L}(q, \dot{q}, t) = \frac{1}{2}\dot{q}^T \mathcal{M}(q)\dot{q} - \mathcal{V}(\phi) \tag{8.1}$$

where $\mathcal{M}(q)$ is a locked inertia tensor and $\mathcal{V}(\phi)$ is the potential energy stored in the spring. In the undeflected position the two shorter links lie along the same line, therefore the angle $\phi$ is $\frac{\pi}{2}$ in the

77

undeflected position. The potential energy is given by

$$\mathcal{V}(\phi) = \frac{1}{2}k_1(2\phi - \pi)^2 + 2k_2\phi^{*2}, \quad \text{where} \tag{8.2}$$

$$\phi^* = \arcsin\left(\frac{l_1}{l_2}\sin\phi\right)$$

where $k_1 > 0$ and $k_2 > 0$ since both of the springs are resistive. The angle $\phi^*$ represents the angle between one of the long links and the $-X_b$ axis as shown in Fig. 8.1. Since $\phi^* = 0$ in the undeflected position the potential energy in the corresponding compliant joint is given by $\frac{1}{2}k_2(2\phi^*)^2 = 2k_2\phi^{*2}$. The extrema of $\mathcal{V}(\phi)$ are given by $\{\phi|\frac{\partial\mathcal{V}(\phi)}{\partial\phi} = 0\}$. By examining Fig. 8.1 and considering that $\phi \in (0, \pi)$ we see that there are two possibilities for the extrema of Eqn. (8.2). Either the potential function is bistable with an unstable position at $\phi = \frac{\pi}{2}$ and a stable position on either side or there is a single stable position at $\phi = \frac{\pi}{2}$. The parameters which cause each of the above cases can be found by checking the sign of $\frac{\partial^2\mathcal{V}}{\partial\phi^2}\Big|_{\phi=\frac{\pi}{2}}$, i.e. the condition for bistability is $\frac{\partial^2\mathcal{V}}{\partial\phi^2}\Big|_{\phi=\frac{\pi}{2}} < 0$. Direct calculation shows this condition to be

$$\frac{k_1}{k_2} < \frac{l_1\arcsin\left(\frac{l_1}{l_2}\right)}{\sqrt{l_2^2 - l_1^2}}\gamma. \tag{8.3}$$

When Eqn. (8.3) is satisfied, the potential function has two new minima, the first at $\phi_1 < \frac{\pi}{2}$ corresponding to what we will call the "closed" position of the compliant mechanism and the second at $\phi_2 > \frac{\pi}{2}$ corresponding to the "open" position.

The system must also satisfy a nonholonomic constraint that the rear wheel is not allowed slip in the transverse $(Y_b)$ direction, i.e.

$$\mathcal{W}(q)\dot{q} = 0, \quad \text{where} \quad \mathcal{W}(q) = \begin{bmatrix} -\sin\theta & \cos\theta & 0 & 0 \end{bmatrix} \tag{8.4}$$

with Pfaffian one form being

$$-\sin\theta dx + \cos\theta dy = 0. \tag{8.5}$$

We also introduce viscous frictional forces by means of a Rayleigh dissipation function that is proportional to the speeds of the each of the masses, $m_1$ to $m_4$. We also assume the structure is damped with the damping force being proportional to $\dot{\phi}$. This means the rate at which energy is
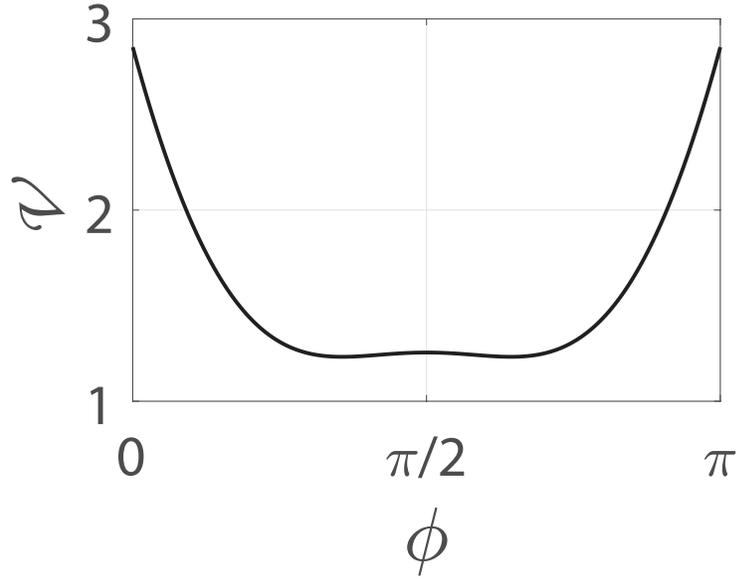
Figure 8.2: Potential energy of the spring as a function of $\phi$ for $\phi \in (0, \pi)$ for parameters $l_1 = 1$, $l_2 = 2$, $k_1 = 0.578$ and $k_2 = 2.289$

being dissipated is

$$\mathcal{R} = \frac{1}{2}c_1(\dot{x}_1 \cos\theta + \dot{y}_1 \sin\theta)^2 + \frac{1}{2}c_2(\dot{x}_2^2 + \dot{y}_2^2)$$
$$+ \frac{1}{2}c_3(\dot{x}_3^2 + \dot{y}_3^2) + \frac{1}{2}c_4(\dot{x}_4^2 + \dot{y}_4^2) + \frac{1}{2}c_m\dot{\phi}^2.$$

We will use $\mathbf{c} = [c_1, c_2, c_3, c_4, c_m]^T$ to denote the vector of dissipation coefficients. The equations of motion of the Chaplygin sleigh can be derived using the method outlined in Chapter 2 to be

$$\begin{bmatrix} \mathcal{M}_b & 0 \\ 0 & 1 \end{bmatrix} \dot{\xi} = \begin{bmatrix} \frac{-1}{B_0(\phi)^3}(B_1(\omega_1^2 + \omega_2^2) + B_2\omega_1^2) \\ \frac{-\omega_1}{2B_0}(B_3 u + B_4\omega_2) + \tau \\ \frac{-l_1}{B_0^4}(B_5(\omega_1^2 + \omega_2^2) + B_6\omega_1^2) - \frac{k}{8}B_7 \\ \omega_2 \end{bmatrix} + \mathcal{D}\xi. \tag{8.6}$$

where $u$ is the velocity of point $P$, $\omega_1$ is the angular velocity of the system, and $\omega_2 = \dot{\phi}$. Also $\mathcal{M}_b$ represents the locked inertia tensor, and $\mathcal{D}(\phi)\xi$ are the dissipation terms which are linear in the reduced velocities. The expressions for $B_0..B_7$ are given in the appendix.

79

Direct calculation shows that $\mathcal{M}_b$ takes the form

$$\mathcal{M}_b = \begin{bmatrix} A_1 & 0 & A_2 \\ 0 & A_3 & 0 \\ A_2 & 0 & A_4 \end{bmatrix} \tag{8.7}$$

where the terms $A_1$ to $A_4$ are given in the appendix. The equations of motion can then be rewritten as

$$\dot{\xi} = \begin{bmatrix} \mathcal{M}_b & 0 \\ 0 & 1 \end{bmatrix}^{-1} \mathbf{g}(\xi) = \mathbf{f}(\xi) \tag{8.8}$$

where $\mathbf{g}(\xi)$ is the right hand side of (8.12).

### 8.1.2 Nonlinear Dynamics of the Compliant Chaplygin Sleigh

To examine the role of compliance in the dynamical system Eqn. (8.17) it is useful to first examine the equations of motion of a rigid Chaplygin sleigh, i.e, one where the angle $\phi$ is a constant. It is natural to frame the equations of motion of such a system in terms of the variable,

$$l_c(\phi) = \frac{(B_0(\phi) - l_1 \cos\phi)m_2 - 2l_1 \cos\phi m_3}{m_1 + m_2 + 2m_3} \tag{8.9}$$

| $\mathbf{c}$ | Case | Fixed Points | $\mu$ | Path |
|---|---|---|---|---|
| | 1 | $u^e(E) > 0,\ \omega_1^e = 0,\ \omega_2^e = 0,\ \phi^e = \phi_1$ | $[a_{1,1}, a_{1,2}i, -a_{1,2}i]$ (U) | Line |
| | 2 | $u^e(E) > 0,\ \omega_1^e = 0,\ \omega_2^e = 0,\ \phi^e = \phi_2$ | $[-a_{2,1}, a_{2,2}i, -a_{2,2}i]$ (U) | Line |
| $\mathbf{c} = 0$ | 3 | $u^*(E) > 0,\ \omega_1^e = 0,\ \omega_2^* = 0,\ \phi^e = \frac{\pi}{2}$ | $[-a_{3,1}, a_{3,2}i, -a_{3,2}i]$ (U) | Line |
| $k_1 < \gamma k_2$ | 4 | $u^e(E) < 0,\ \omega_1^e = 0,\ \omega_2^e = 0,\ \phi^e = \phi_1$ | $[-a_{4,1}, a_{4,2}i, -a_{4,2}i]$ (U) | Line |
| | 5 | $u^e(E) < 0,\ \omega_1^e = 0,\ \omega_2^e = 0,\ \phi^e = \phi_2$ | $[a_{5,1}, a_{5,2}i, -a_{5,2}i]$ (U) | Line |
| | 6 | $u^e(E) < 0,\ \omega_1^e = 0,\ \omega_2^* = 0,\ \phi^e = \frac{\pi}{2}$ | $[a_{6,1}, a_{6,2}i, -a_{6,2}i]$ (U) | Line |
| $\mathbf{c} = 0$ | 7 | $u^*(E) > 0,\ \omega_1^e = 0,\ \omega_2^* = 0,\ \phi^e = \frac{\pi}{2}$ | $[-a_{7,1}, a_{7,2}i, -a_{7,2}i]$ (U) | Line |
| $k_1 > \gamma k_2$ | 8 | $u^e(E) < 0,\ \omega_1^e = 0,\ \omega_2^* = 0,\ \phi^e = \frac{\pi}{2}$ | $[a_{8,1}, a_{8,2}i, -a_{8,2}i]$ (U) | Line |

Table 8.1: Fixed points of the equations (8.12). The fixed points are denoted by $(u^e, \omega_1^e, \omega_2^e, \phi^e)$. The fixed points are divided according to the nature of the potential function (bistable when $k_1 < \gamma k_2$). For bistable case we use $k_1 = 0.578$, $k_2 = 2.289$ and for the single well potential we use $k_1 = 1$, $k_2 = 2$. The fourth column shows the nature of the eigenvalues of the Jacobian of the reduced system (8.12) for the cases where $\mathbf{c} = 0$. The notation employed is that each $a_{j,k} > 0$ corresponds to the $j$'th case for $j = 1, 2, 3...$ and $i = \sqrt{-1}$. The letters (S) and (U) indicate stable and unstable fixed points respectively.

80

which is the $x$ coordinate of the center of mass the sleigh in the body fixed frame $X_b - Y_b$. Setting $\phi$ equal to a constant in Eqn. (8.15) the reduced equations of motion are well known to be [6, 8, 15]

$$\dot{u} = l_c \omega_1^2$$
$$\dot{\omega_1} = \frac{-ml_c u \omega_1}{I + ml_c^2} \tag{8.10}$$

where $m = m_1 + m_2 + m_3 + m_4$ and $I$ is the moment of inertia of the sleigh about the center of mass. The dynamical system Eqn. (8.10) is dissipative in the sense that volumes in phase space shrink; the trace of the Jacobian of the vector field Eqn. (8.10) is negative. The system however converges the total energy. From Eqn. (8.10) it is obvious that $\omega_1 \to 0$ for all initial conditions and that the set $\{(u, \omega_1) | \omega_1 = 0\}$ is a set of nonisolated fixed points for the system. These fixed points are stable when $sign(u) = sign(l_c)$. In other words the stable motion of the sleigh is such that the velocity of the point $P$ is pointing towards the center of mass. This stable direction of motion persists even when the sleigh is actuated by a periodic torque [3, 25]; the periodically forced sleigh is shown to have motion such that $u > 0$ on average when $l_c > 0$. Therefore relative location of the center of mass with the point of contact determines the preferred direction of travel for the sleigh.

This feature can be exploited in the compliant mechanism since the center of mass is able to change location. The length parameter $l_c$ for the stable equilibria of the structure becomes $l_c(\phi_1)$ and $l_c(\phi_2)$ for the closed ($\phi_1 < \frac{\pi}{2}$) and open ($\phi_1 > \frac{\pi}{2}$) positions respectively. We show that a compliant mechanism can be designed such that $l_c(\phi_1) < 0$ and $l_c(\phi_2) > 0$ making use of the bistability to manipulate the preferred direction of travel of the compliant sleigh.

From the above equations one can see that any fixed point requires $\omega_2 = 0$ i.e. internal angle, $\phi$, is fixed. When the internal angle is fixed the equations of the system reduce to that of a rigid Chaplygin sleigh where fixed points are of the form $(u, \omega_1) = (u_0, 0)$ where $u_0$ is a constant. Setting $\omega_1 = \omega_2 = 0$ in the equations leaves only the potential energy terms which are zero when $\phi \in \{\phi_1, \phi_2, \frac{\pi}{2}\}$. Therefore all fixed points are of the form $(E, 0, 0, \phi_e)$ where $\phi_e$ is one of the equilibria for the potential function and $E > 0$ is the energy. These fixed points correspond to fixed points of the form $\xi = (u_0, 0, 0, \phi_e)$ for (8.17) where

$$u_0 = \pm \sqrt{\frac{2E}{m_1 + m_2 + 2m_3}}$$

81

In order to make full use of the bistability to change the location of the center of mass it becomes useful to find a set of parameters such that $l_c(\phi_1) = -l_c(\phi_2)$. This will allow us to apply any control law we use in one stable configuration to the other stable configuration. Substituting ?? into the aforementioned condition we get

$$m_2\sqrt{l_e^2 - 4l_2^2} = 0. \tag{8.11}$$

Therefore in order to satisfy $l_c(\phi_1) = -l_c(\phi_2)$ we require that either $m_2 = 0$ or $\sqrt{l_e^2 - 4l_2^2} = 0$ which only happens if $l_e = 2l_2$. However since $l_1 \leq l_2$ for bistability to be physically possible and by definition $l_e \leq 2l_1$, the constraint $l_e = 2l_2$ requires that $l_e = 2l_2 = 2l_1$ which is no longer bistable as the links are all along a line in the stable position. Therefore $l_c(\phi_1) = -l_c(\phi_2)$ requires that $m_2 = 0$.

### 8.1.3   Unforced Dynamics

We first note that $\mathcal{M}_b$ is symmetric and positive definite. Therefore the block diagonal matrix on the left side of Eqn. (8.17) is invertible. This implies that $\dot{\xi} = 0$ is and only if the right hand side of Eqn. (8.17) is zero. In particular the equation describing $\dot{\omega}_1$ can be directly obtained as

$$A_3\dot{\omega}_1 = \frac{-\omega_1}{2B_0}(B_3u + B_4\omega_2)$$

in the absence of forcing or dissipation. From the above we see that for the unforced case $\omega_1(0) = 0 \to \omega_1(t) = 0$. Therefore if $\omega_1(0) = 0$, $\dot{\omega}_1 = 0$, i.e., $\omega_1 = 0$ is an invariant manifold of Eqn. (8.17) just as in the case of the rigid Chaplygin sleigh. Dynamics on this invariant manifold correspond to the motion of the sleigh along a straight line in the longitudinal ($X_b$) direction, with perhaps $\dot{\phi}$ that is not identically zero.

Other invariant manifolds of Eqn. (8.17) exist when the viscous dissipation is absent and the applied torque on the sleigh is zero. In such cases the energy is an integral of motion of Eqn. (8.17) and we can further reduce the number of variables by writing one of the velocities in terms of the energy. We can confine our analysis of the stability of invariant manifolds of Eqn. (8.17) to level sets of the energy $E$ by solving the energy equation for $u$ to get $u(E, \omega_1, \omega_2, \phi)$ and substitute

this expression into the equations of motion. The equations of motion can then be written as

$$\begin{bmatrix} \dot{\omega}_1 \\ \dot{\omega}_2 \\ \dot{\phi} \end{bmatrix} = \begin{bmatrix} f_1(E, \omega_1, \omega_2, \phi) \\ f_2(E, \omega_1, \omega_2, \phi) \\ \omega_2 \end{bmatrix} = \mathbf{h}(\xi) \qquad (8.12)$$

From Eqn. (8.12) one can see that any fixed point requires $\omega_2 = 0$ i.e. internal angle, $\phi$, is fixed. When $\omega_2 = 0$ we see from the first equation of Eqn. (8.17) that $\omega_1 = 0$ is also necessary for any fixed point. Setting $\omega_1 = \omega_2 = 0$ in the equations leaves only the potential energy terms which are zero when $\phi \in \{\phi_1, \phi_2, \frac{\pi}{2}\}$. Therefore all fixed points are of the form $\xi_0 = (u_0(E), 0, 0, \phi^e)$ where $\phi^e$ is one of the equilibria for the potential function and

$$u_0(E) = \pm \sqrt{\frac{2(E - \mathcal{V}(\phi^e))}{m_1 + m_2 + 2m_3}} \qquad (8.13)$$

Due to the complexity of the equations, analysis of the eigenvalues of the Jacobian, $D\mathbf{h}$, of $\mathbf{h}(\xi)$ around the fixed points is cumbersome; however using the parameters chosen for our simulations (see Fig. 8.3) we can check the eigenvalues for each value of $\phi^e$ and values of $u \in [-10, 10]$. The nature of eigenvalues, $\mu$, of $D\mathbf{h}(\xi_0)$ is shown in Table 8.1. We see from Table 8.1 that $D\mathbf{h}(\xi_0)$ for any fixed point $\xi_0$ of $\mathbf{h}$ has a pair of imaginary eigenvalues showing that none of the fixed points are asymptotically stable.

We find that the sign of the real eigenvalue in each case varies as

$$sign(u_0) = sign(l_c(\phi^*)) \rightarrow a_{j,1} < 0$$
$$sign(u_0) \neq sign(l_c(\phi^*)) \rightarrow a_{j,1} > 0.$$

The real eigenvalue corresponds to an eigenvector of the form $[1, 0, 0]^T$ implying $\omega_1$ either grows or decays exponentially in the neighborhood of any fixed point. For any given energy and specified $\phi^e$ there are two fixed points corresponding to positive and negative values of $u_0$ Eqn. (8.13). This is due to the fact that $E(u_0, 0, 0, \phi^e) = E(-u_0, 0, 0, \phi^e)$. Therefore for any given energy there always exists at least one fixed point for which $sign(u_0) \neq sign(l_c(\phi^*))$ and in the neighborhood of such a fixed, any local perturbation of $\omega_1$ would grow locally. On the other hand for the fixed

83
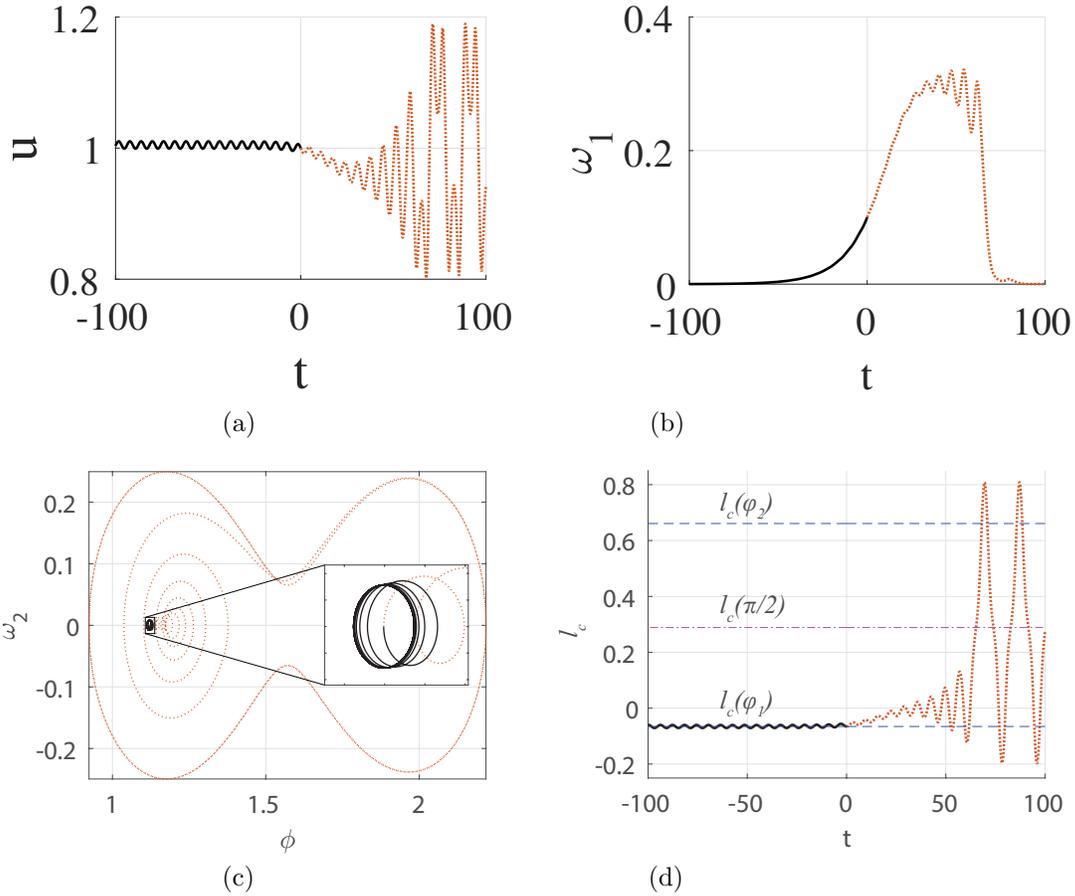
Figure 8.3: A simulation of the unforced mechanism without dissipation. The orange dotted line shows the forward time motion and the solid black line shows backward time motion. The horizontal lines in (e) correspond to the extrema of $\mathcal{V}(\phi)$. Parameters are $l_1 = 1$, $l_2 = 2$, $k_1 = 0.578$, $k_2 = 2.289$, $m_1 = .5$, $m_2 = .5$, $m_3 = 1$, $c_1 = 0$, $c_2 = 0$, $c_3 = 0$ and $c_4 = 0$.

point for which $sign(u_0) = sign(l_c(\phi^*))$ any perturbation in $\omega_1$ decays to zero in the neighborhood of a fixed point. Physical motion that corresponds to such a fixed point of the reduced equations is such that the velocity of point $P$ points towards the center of mass. Furthermore when $\omega_1 = 0$, $\dot\omega_1 = 0$ and the system reduces to a two degree of freedom system with two first integrals being the linear momentum and the energy. As a completely integrable system its motion must then be confined to a torus. This suggests that the fixed points of the unforced system are locally centers as the eigenvalues in the $(\omega_2, \phi)$ directions are imaginary and the solutions are all quasiperiodic. Numerical simulations show that any generic trajectory approaches oscillations in $(\omega_2, \phi)$ around this fixed point as $\omega_1 \to 0$ exponentially. The convergence of $\omega_1 \to 0$ is consistent with the behavior

| $\mathbf{c}$ | Case | Fixed Points | $\mu$ |
|---|---|---|---|
| $\mathbf{c} > 0$ $k_1 < \gamma k_2$ | 1 | $u^e = 0,\ \omega_1^e = 0,\ \omega_2^e = 0,\ \phi^e = \phi_1$ | $[-a_{9,1}, -a_{9,2}+a_{9,3}i, -a_{9,2}-a_{9,3}i, -a_{9,4}]$ (S) |
| | 2 | $u^e = 0,\ \omega_1^e = 0,\ \omega_2^e = 0,\ \phi^e = \phi_2$ | $[-a_{10,1}, -a_{10,2}+a_{10,3}i, -a_{10,2}-a_{10,3}i, -a_{10,4}]$ (S) |
| | 3 | $u^e = 0,\ \omega_1^e = 0,\ \omega_2^e = 0,\ \phi^e = \frac{\pi}{2}$ | $[-a_{11,1}, -a_{11,2}, a_{11,3}, -a_{11,4}]$ (U) |
| $\mathbf{c} > 0$ $k_1 > \gamma k_2$ | 4 | $u^e = 0,\ \omega_1^*(E),\ \omega_2^e = 0,\ \phi^e = \frac{\pi}{2}$ | $[-a_{12,1}, -a_{12,2}+a_{12,3}i, -a_{12,2}-a_{12,3}i, -a_{12,4}]$ (S) |

Table 8.2: Fixed points of the equations Eqn. (8.17). The fixed points are denoted by $(u^e, \omega_1^e, \omega_2^e, \delta^e)$. The fixed points are divided according to the nature of the potential function (bistable when $k_1 < \gamma k_2$). The fourth column shows the nature of the eigenvalues of the Jacobian of the system Eqn. (8.17). The notation employed is that each $a_{j,k} > 0$ corresponds to the $j$'th case for $j = 1, 2, 3...$ and $i = \sqrt{-1}$. The letters (S) and (U) indicate stable and unstable fixed points respectively.

of the rigid Chaplygin sleigh; all solutions of Eqn. (8.10) are such that $\omega \to 0$. The dynamics of the rigid Chaplygin sleigh are therefore embedded within the dynamics of the compliant mechanism. This behavior is demonstrated in Fig. 8.3. Beginning with initial conditions $(1, 0.1, 0, \phi_1)$ note that for the chosen parameters $l_c(\phi_1) < 0$. Therefore for $u(0) > 0$ we expect a perturbation of $\omega_1(0) = 0.1$ to grow locally until $l_c$ or $u$ changes sign (case 1 in Table 8.1). This is what we see in Fig. 8.3 (b), the perturbation in $\omega_1$ initially grows until $l_c$ begins to exhibit interwell oscillations around a fixed point corresponding to case 3 in Table 8.1 where $l_c > 0$ on average (Fig. 8.3 (d)). When this happens $\omega_1$ decays and converges to zero. Starting with the same initial conditions, in backwards time we see that $\omega_1 \to 0$ exponentially. In this case the trajectory converges to a periodic solution with intrawell oscillations about $\phi_1$. In both forward and backward the torus dynamics obtained by setting $\omega_1 = 0$. These are characterized by the closed curves we see in Fig. 8.3 (c).

### 8.1.4 Limit Cycles of the System With Dissipation

When viscous dissipation is non zero, in the absence of forcing the system will continue to dissipate energy as long as any of the velocities are not zero. Therefore the only fixed point of the system with dissipation is $(u, \omega_1, \omega_2) = (0, 0, 0)$. Setting the velocities to zero leaves only the potential forces on the right hand side of Eqn. (8.17). Therefore the compliant sleigh with viscous dissipation has fixed points corresponding to the extrema of the potential energy. Each, therefore takes the form $\xi = (0, 0, 0, \phi^e)$ where $\phi^e$ is one of the extrema of the potential energy. As a result we see three fixed points when $k_1 < \gamma k_2$ and one fixed point otherwise. These fixed points as well as the eigenvalues of the Jacobian of $\mathbf{f}(\xi)$ are listed in Table 8.2.

Since all the velocities associated with these fixed points must be zero, they correspond to

85

the sleigh being at rest such that $\phi = \phi^e$. These fixed points are stable as long $\phi^e$ is one of the minima of the potential energy as we see in cases 1, 2, and 4. For case 3, any perturbation will cause convergence to either of the fixed points of cases 1 or 2. These static fixed points play a key role in influencing the dynamics of the compliant sleigh even when it is subjected to a periodic forcing.



(a)    (b)
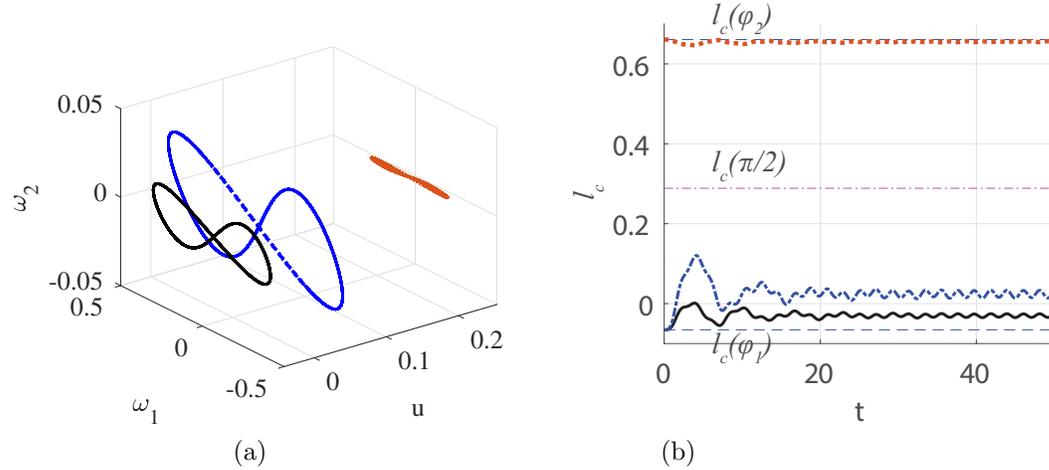
Figure 8.4: (a) Limit cycles of the compliant Chaplygin sleigh. (b) Position of the center of mass. Black solid line is for the case $\tau = 1.5\cos(1.5t)$ beginning from the closed position, the blue dashed line for $\tau = 2.2\cos(1.5t)$ also beginning from the closed position and the dotted orange line for $\tau = 1.5\cos(1.5t)$ beginning from the open position. Parameters are $l_1 = 1$, $l_2 = 2$, $k_1 = 0.578$, $k_2 = 2.289$, $m_1 = m_2 = 0.5$, $m_3 = 1$, $c_1 = c_2 = c_3 = c_4 = 0.05$.

When a periodic input is applied on the compliant sleigh, for instance through the periodic oscillations of a balanced rotor carried on the sleigh, it exhibits limit cycle motions near one of the stable equilibrium positions. We denote $(\bar{u}, \bar{\omega}_1, \bar{\omega}_2, \bar{\phi})$ to be the average values of the reduced velocities and $\phi$ on the limit cycle. In particular, three types of motions were identified. Forward $(\bar{u} > 0)$ or backward $(\bar{u} < 0)$ motion can be generated for the closed position $(\bar{\phi} < \frac{\pi}{2})$ depending on the amplitude and frequency of the input. Forward motion can also be generated for the open position $(\bar{\phi} > \frac{\pi}{2})$. These three types of limit cycles are shown in Figure 8.4 for a sample set of sleigh parameters. These parameters are chosen such that the center of mass is lies on the negative $X_b$ axis close to the point of contact in the closed position, i.e. $l_c(\phi_1) = -\epsilon$ where $\epsilon \ll 1$. This allows the sleigh to achieve both forward or backward motion for the closed position. For the solid black and dashed blue lines, we have $\phi(0) = \phi_1$ and for the dotted orange lines we have $\phi(0) = \phi_2$. In each case the resulting oscillations are close to $\phi(0)$.

Figure 8.4 (a) shows that when the center of mass is close to the point of contact $(l_c(\phi) \approx 0)$, the sleigh exhibits large amplitude oscillations in the angular velocities. For the same input applied

86

in the open position we get a different limit cycle such that $\bar{u}$ is much higher and the average velocity is greatly increased (Fig. 8.4 (a)). Conversely the oscillations in the angular velocity are reduced. Note that near the closed position both forward and backward motion can be achieved by changing the periodic input. The change in direction of travel is only achieved, however, when the point of contact is close to the center of mass of the sleigh in the closed position ($l_c(\phi_1) \approx 0$) and such that $l_c(\phi_1) < 0$ as seen in Fig. 8.4b. This effect is caused by the fact that increasing the amplitude of the input causes the limit cycle oscillations in $\phi$ to be not about the equilibrium position exactly but around a higher value ($l_c(\bar{\phi}) > 0 > l_c(\phi_1)$). The reversal in direction is consistent with the behavior of the unforced compliant sleigh and the classical Chaplygin sleigh in that the position of the center of mass relative to the constraint determines the preferred direction of travel.

This change in direction of travel is clearly seen in Fig. 8.5 (a) where we see that starting from the same position, one input causes the sleigh to propel itself forward while another causes motion in the opposite direction but at a similar velocity (Fig. 8.5 (b)). As discussed, this is due to the sign of $l_c(\bar{\phi})$ being different for each of the two cases. The ability to change direction of travel demonstrates a potential way to exploit the compliance of the system. Compliance and bistability also give us variations in the speed of the system as seen in Fig. 8.5b.



(a)                      (b)
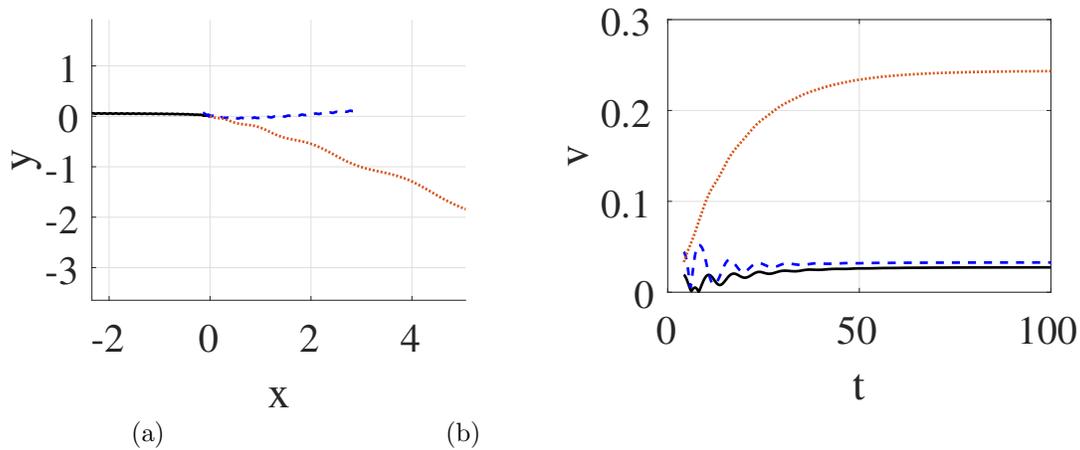
Figure 8.5: (a) trajectories in the $(x, y)$ plane, the trajectory for the open position is only shown for the first 20 seconds (b) average velocity of the sleigh. Parameters are $l_1 = 1$, $l_2 = 2$, $k_1 = 0.578$, $k_2 = 2.289$, $m_1 = .5$, $m_2 = .5$, $m_3 = 1$, $c_1 = .05$, $c_2 = .05$, $c_3 = .05$ and $c_4 = .05$. Initial conditions are all zero except for $\phi$ as indicated.

87

## 8.2 An Origami Inspired Nonholonomic System

In this section we develop an equivalent Chaplygin sleigh-like model for the locomotion of a bistable origami pattern called the *generalized Kresling pattern*. This work was done in collaboration with Doctor Suyi Li and Priyanka Bhovad from the Dynamic Matter Group at Clemson University. They are experienced with origami and performed the experimental work in this section. The origami system is modeled as a Chaplygin sleigh with an internal nonlinear oscillator. By using the nonlinear spring-like behaviors from the bistable Kresling origami, we show that intrawell oscillations of the Kresling pattern can cause the sleigh to travel in a circle on average. The radius and the average velocity of the circle are different when the Kresling pattern is oscillating around different equilibria. Moreover the physical space occupied by the mechanism is different in each of the two equilibrium configurations, with the mechanism moving faster in the larger configuration. We show that by taking advantage of the bistability of the Kresling pattern it is possible to switch the configuration of sleigh from the larger to the smaller one. Such switches in configuration are useful for a mobile robot that has to for instance navigate in narrow confined spaces.

### 8.2.1 Generalized Kresling Pattern

The "traditional" Kresling pattern was developed by Biruta Kresling [45] and its geometric design and bistability is extensively studied in literature [31,35,40,64]. It is designed as a flat-foldable mechanism, that is, its length at fully-contracted stable state is exactly zero. In this study, we use a "generalized" Kresling pattern, which has a non-zero length at fully-contracted stable state [2]. This non-zero length is described by a new design parameter $H$, and it opens up a new design space for the Kresling pattern. Moreover, the generalized Kresling pattern can better accommodate the realistic sheet material thickness in its design.

The design parameters of the generalized Kresling pattern are: $n$ (number of sides of the base and top polygon), $p$ (side length of the base and top polygon), $\mu_i$ (angle ratio), and $H$ (Kresling segment length at the fully-contracted stable state). The crease pattern is composed of equally spaced mountain and valley creases (Figure 8.6 (a)). The first and last valley creases are glued together to generate an axisymmetric twisted polygonal prism (Figure 8.6 (b)). The base and top of the cylinder create regular polygons that remain rigid during the folding motion. To design the generalized Kresling pattern, we start from the traditional Kresling, with its geometry given by
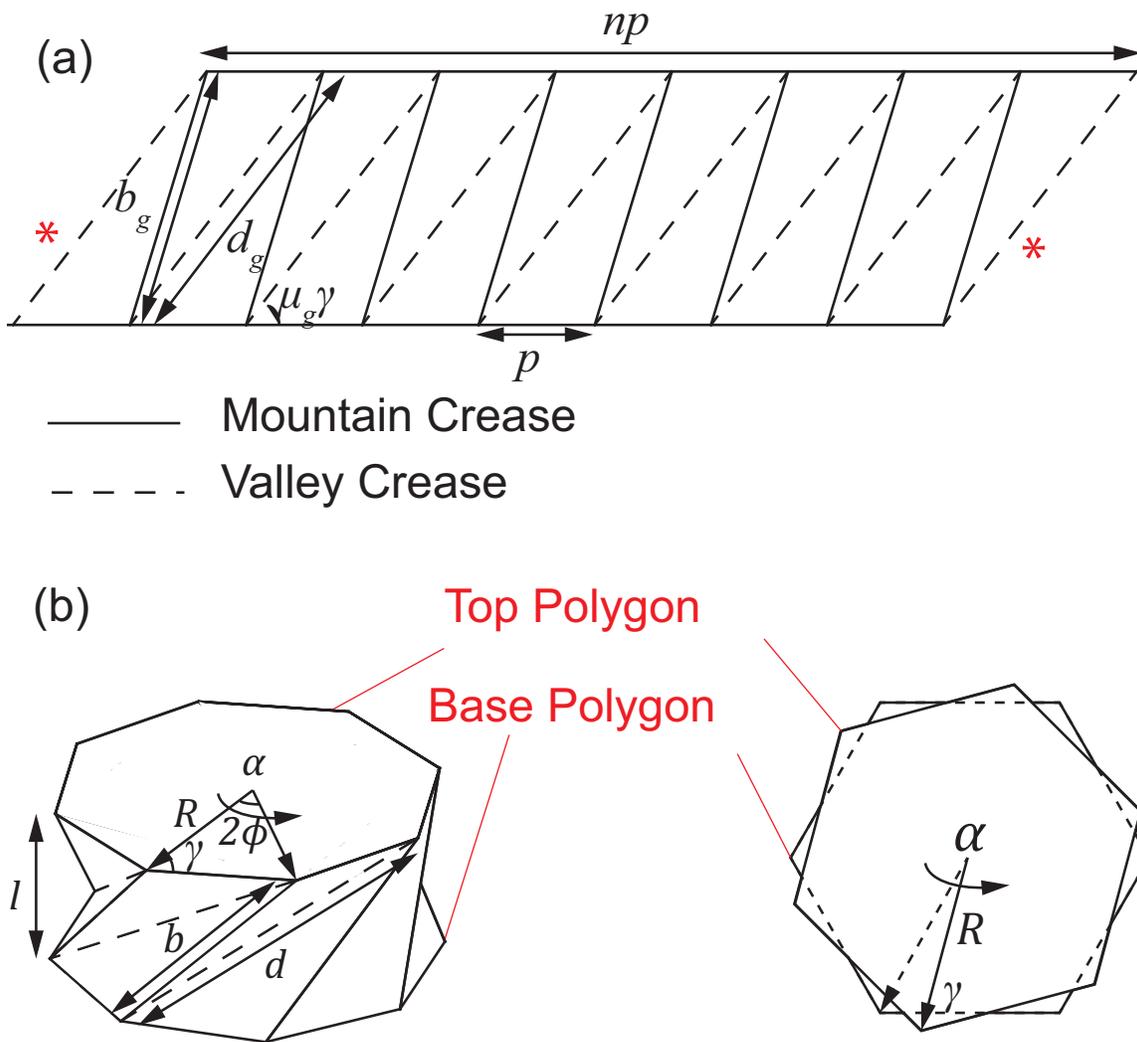
Figure 8.6: The design of the generalized Kresling pattern (a) Crease pattern depicting the design parameters. The creases marked with (*) are glued together to create a Kresling segment. (b) Isometric view and top view of folded Kresling segment depict the important geometric parameters and the sign convention for rotation angle $\alpha$

$$\phi = \frac{\pi}{n}, \quad R = \frac{p}{2\sin(\phi)}, \quad \gamma = \frac{\pi}{2} - \phi,$$

where $\phi$ is half the internal angle of the base and top polygon, $R$ is the circumscribed radius of the base and top polygon, $\gamma$ is the angle between the radius vector and polygon side as shown in Figure 8.6 (b). The strain-free lengths of the valley and mountain creases are then given by

$$d_i = 2R\cos(\gamma - \mu_i\gamma),$$

$$b_i = \sqrt{p^2 + d_i^2 - 2pd_i\cos(\mu_i\gamma)}.$$

The top polygon of traditional Kresling segment is translated away from the bottom polygon by a distance of $H$ to create the generalized Kresling. The resulting crease pattern is no longer flat-foldable; but retains an identical range of rotation as viewed from the top. The new strain-free lengths of valley and mountain crease and the angle of inclination of valley crease are given by

$$d_g = \sqrt{d_i^2 + H^2},$$

$$b_g = \sqrt{b_i^2 + H^2},$$

$$\mu_g\gamma = \cos^{-1}\left(\frac{p^2 + d_g^2 - b_g^2}{2pd_g}\right)$$

Here, the subscript $i$ refers to the parameters for traditional Kresling and subscript $g$ refers to those for generalized pattern. The angle of rotation ($\alpha$) is used to characterize the folding motion of a segment (Figure 8.6 (b)). The length of the segment ($l$) is defined as the perpendicular distance between top and bottom polygon. The lengths of valley and mountain crease are then calculated as

$$d = \sqrt{2R^2(1 - \cos(\alpha + 2\phi)) + l^2},$$

$$b = \sqrt{2R^2(1 - \cos(\alpha)) + l^2}. \tag{8.14}$$

From the fully-contracted geometry we can determine the upper limit for $\alpha$ to be, $\alpha_c = 2\mu_i\gamma$. The lower limit for $\alpha$ can be computed by setting the length $b$ equal to the natural length $b_g$ and solving for $\alpha$.

$$\alpha_e = \{\min(\alpha)|b(\alpha) = b_g\}.$$

The mountain and valley creases in Kresling segment can be assumed as truss members connected by pin joints [40]. It can be assumed that the length of the valley crease ($d$) remains constant and only mountain crease ($b$) is compressed or stretched throughout the folding motion [31]. With this assumption, the derivative of $d$ with respect to $\alpha$ is zero so that

$$l = \sqrt{H^2 + 2R^2(\cos(\alpha + 2\phi) - \cos(\alpha_c + 2\phi))}. \tag{8.15}$$

Thus, we have closed form solutions for describing the folding kinematics. The strain ($\epsilon$) and strain energy ($U$) due to folding can now be calculated as

$$\epsilon = \frac{b}{b_g} - 1, \text{ and } U = \frac{1}{2}K\epsilon^2,$$

where $K$ is the material stiffness. For the purpose of this analysis we normalize the strain energy $U$ by $K$, and define the non-dimensional strain energy as $E = \frac{1}{2}\epsilon^2$. The normalized strain energy of the Kresling segment is minimum at its two stable configurations (Figure 8.7). Thus, we have two distinct potential energy wells separated by a peak. This bistability in a Kresling segment arises due to the non-rigid foldable nature of the facets. That is, its facets are undeformed at the two stable states, but they have to undergo some deformation while folding between the two stable states. We will use this property of bistable generalized Kresling segment to get two distinct modes of locomotion in Chaplygin sleigh.
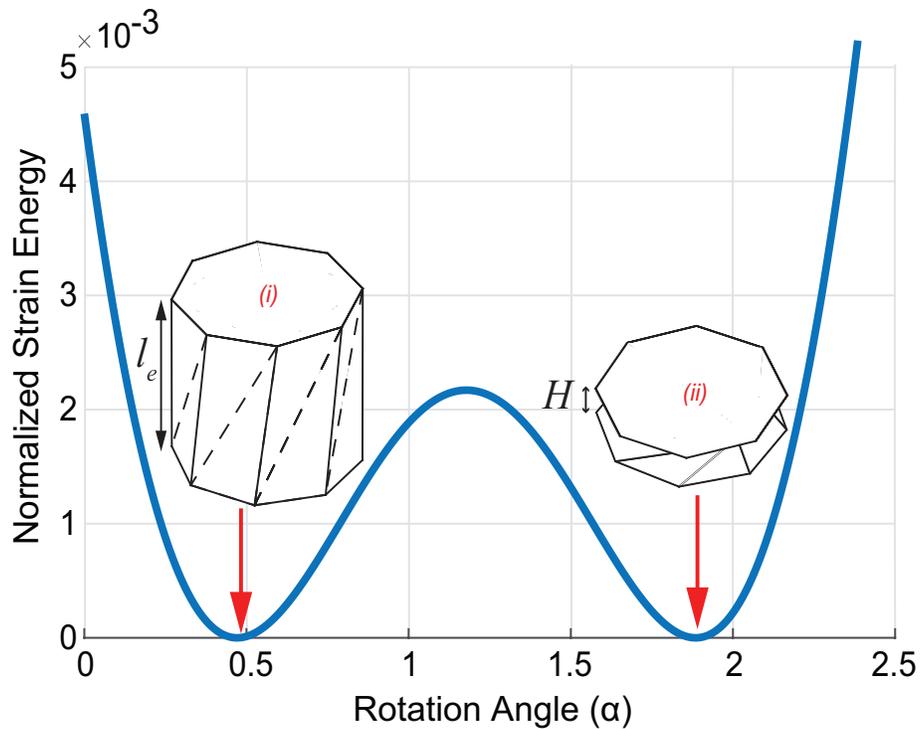


Figure 8.7: The normalized strain energy versus rotation angle for bistable generalized Kresling segment. (*i*) denotes fully-extended stable state, $l_e = l(\alpha_e)$ and (*ii*) denotes fully-contracted stable state. $n = 8, p = 30$ mm, $\mu_i = 0.8$ and $H = 20$ mm

### 8.2.2 Experimental Results

We have experimentally verified the bistability of generalized Kresling segment. The experimental setup is shown in Figure 8.8. The tests were performed on ADMET Universal Testing Machine (eXpert 5601). The generalized Kresling segment was fabricated from paper (Daler - Rowney Canford 150 gsm). First, the 2-D drawing of the pattern was prepared in the $Solidworks^{®}$ software. This pattern was then cut out of the paper with perforated creases using $CricutMaker^{®}$. Additional reinforcement triangles were attached to the triangular facets using double sided tape. Finally, the segment was folded by hand and the top and bottom polygons were attached to the segment using double sided tape. A custom rotation fixture was designed using dual ball-bearing hub to allow for free rotation of one end of the Kresling segment. One end of the Kresling segment was fixed to the rotation fixture mounted on the lower base plate and the other end was fixed to the upper platen.
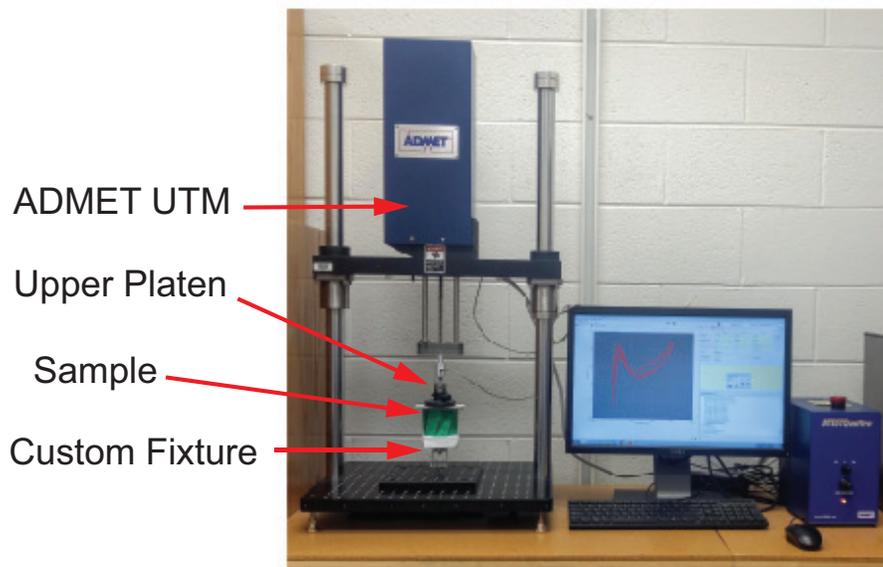


Figure 8.8: Experimental setup for verification of bistability for generalized Kresling segment

Some modifications to the pattern were deemed necessary in the fabrication of Kresling

www.manaraa.com
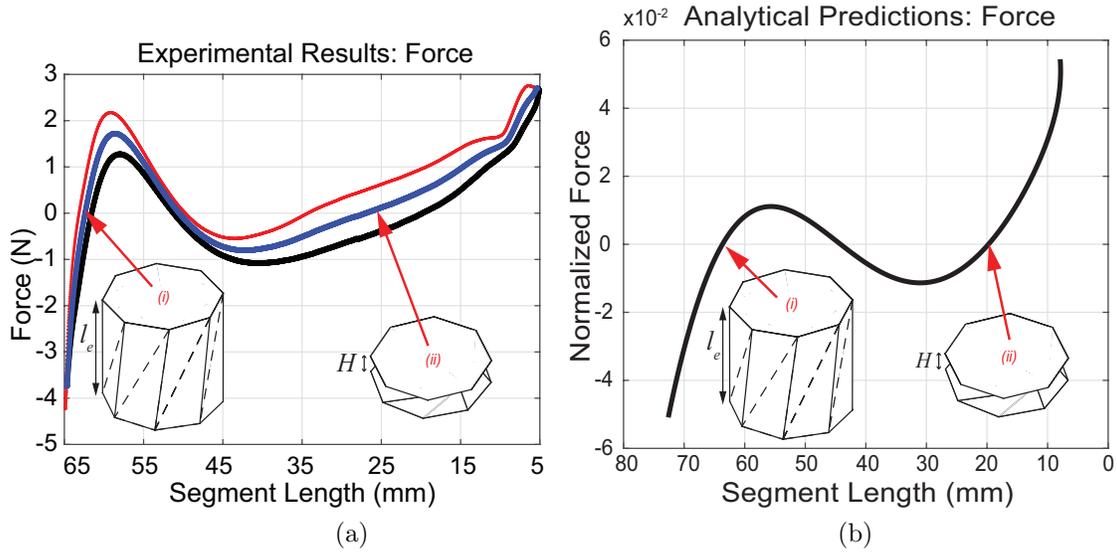
Figure 8.9: Verification of the bistability of Kresling segment (a)Experimental results: Force versus segment length. Red line represents reaction force under contraction and the black line represents reaction force under extension. The blue line is the averaged reaction force. (b) Analytical predictions: Normalized force versus segment length. $(i)$ denotes the fully-extended stable state, $l_e = l(\alpha_e)$ and $(ii)$ denotes the fully-contracted stable state. $n=8$, $p=30$ mm, $\mu_i=0.8$, $H=20$ mm

segment. During the initial testing it was observed that excessive stresses were developing along the mountain creases. This caused the bistable segment to tear after a few cycles of testing. Thus, the mountain creases were cut to allow smooth folding motion of the segment. A similar approach is used in literature, where the resulting pattern is called Flexigami [57]. Additionally, triangular reinforcements were added to the triangular facets to increase their relative stiffness compared to creases and get stronger bistability. The elasticity of paper, fabrication defects, contact between the deforming triangular facets, and internal friction cause the contraction and extension path to vary slightly. As a result, we see a hysteresis loop forming instead of a single curve for force versus displacement as seen in analytical prediction. The bistable nature of the generalized Kresling segment is evident from the Figure 8.9.

### 8.2.3 Dynamic Model

In this section we develop model of a Chaplygin sleigh like nonholonomic system based on the Kresling origami pattern. The Chaplygin sleigh is modeled as vertical plate connected to the wheel via a rigid arm. The sleigh has mass $m_c$ and moment of inertia $I_1$. The sleigh has a

93
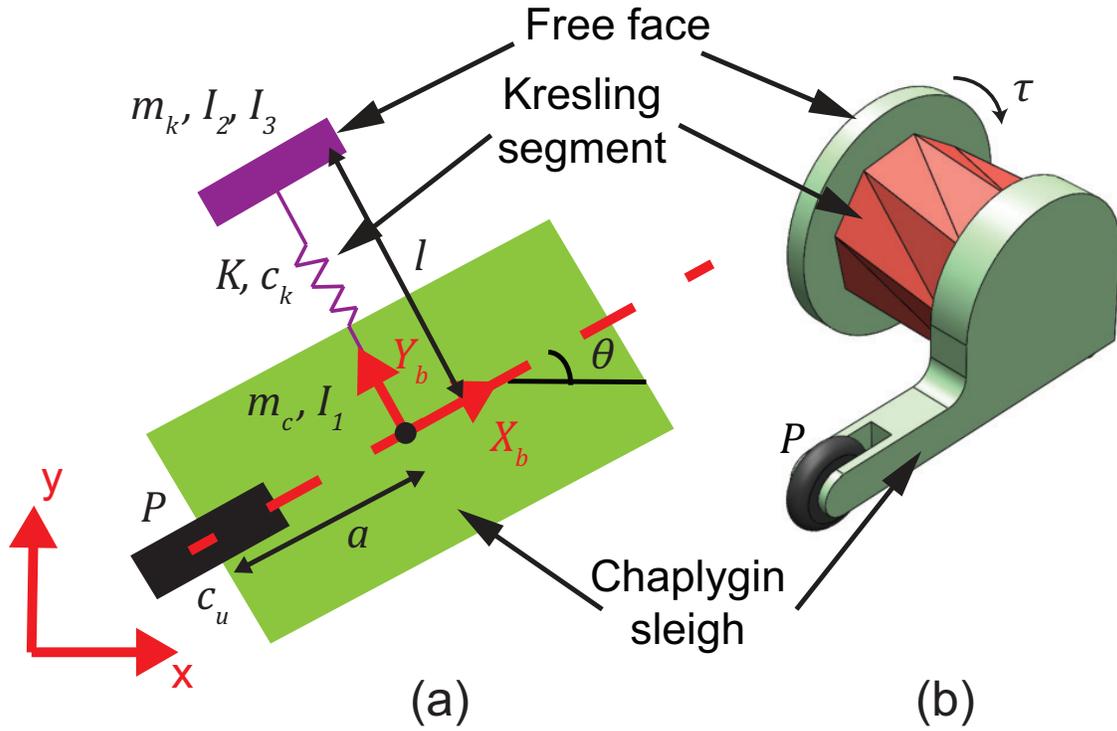
Figure 8.10: Origami inspired Chaplygin sleigh: (a) Schematic of the system depicting design parameters and co-ordinate systems (b) 3D visualization of the origami sleigh. The nonholonomic constraint is applied to the sleigh at point P.

nonholonomic constraint applied to point P on the wheel which does not allow motion in the $Y_b$ direction (Figure 8.10 (a)). The Kresling segment is mounted on the sleigh such that its base and top polygon are perpendicular to the $(x, y)$ plane and segment's axis of rotation is aligned with $Y_b$ (Figure 8.10 (b)). One face of the segment is fixed to the Chaplygin sleigh and the other face is free to rotate about its rotation axis. The torque $(\tau)$ is applied to the free face about $Y_b$ axis . This face is weighted with mass $m_k$ and moments of inertia about the $z$ axis and its own axis are $I_2$ and $I_3$ respectively.

The system has a configuration manifold $SE(2) \times S^1$ parameterized by $q = [x, y, \theta, \alpha]^T$ where $(x, y)$ is the position of the sleigh, $\theta$ is the orientation and $\alpha$ is the rotation angle of the Kresling segment. The positions and velocities of the free face can be written as

$$x_k = x - l(\alpha) \sin(\theta)$$

$$y_k = y + l(\alpha) \cos(\theta)$$

94

and

$$\dot{x}_k = \dot{x} - \dot{l}(\alpha, \dot{\alpha}) \sin(\theta) - l(\alpha)\dot{\theta} \cos(\theta)$$

$$\dot{y}_k = \dot{y} + \dot{l}(\alpha, \dot{\alpha}) \cos(\theta) - l(\alpha)\dot{\theta} \sin(\theta).$$

The Lagrangian of the system ($\mathcal{L}$) is then given by

$$\mathcal{L} = \frac{1}{2}m_c(\dot{x}^2 + \dot{y}^2) + \frac{1}{2}m_k(\dot{x_k}^2 + \dot{y_k}^2)$$
$$+ \frac{1}{2}(I_1 + I_3 + ml^2)\dot{\theta}^2 + \frac{1}{2}I_2\dot{\alpha}^2 - U(\alpha)$$

The system must satisfy the nonholonomic constraint that the velocity of point $P$ parallel to the origami structure is zero

$$-\sin(\theta)\dot{x} + \cos(\theta)\dot{y} = 0.$$

with Pfaffian one form being

$$-\sin\theta dx + \cos\theta dy = 0. \tag{8.16}$$

The system is also subject to Raleigh dissipation modeled by the dissipation function

$$\mathcal{R} = \frac{1}{2}c_u u^2 + \frac{1}{2}c_k \dot{l}^2$$

where $u$ is the velocity of point $P$ in the axis pointing to the center of mass and $c_k$ is the damping in the Kresling pattern. Let us define the body-fixed state vector $\xi = [u, \omega_1, \omega_2, \alpha]^T$ where $u$ is the velocity of $P$, $\omega_1 = \dot{\theta}$, and $\omega_2 = \dot{\alpha}$. The following reduced equations are then obtained

$$\begin{bmatrix} \mathcal{M}_b(\alpha) & 0 \\ 0 & 1 \end{bmatrix} \dot{\xi} = \begin{bmatrix} f_1(u, \omega_1, \omega_2, \alpha) \\ f_2(u, \omega_1, \omega_2, \alpha) \\ f_3(u, \omega_1, \omega_2, \alpha) \end{bmatrix} \tag{8.17}$$

where $f_1$, $f_2$, $f_3$ and the elements of $M_b(\alpha)$ are described in the appendix.

### 8.2.4 Limit Cycles of the Origami Chaplygin Sleigh

We simulate the equations of motion (8.17) under the effect of a periodic torque $\tau$. The origami robot exhibits limit cycle motion for a large range of parameters and control inputs. Al-

though the system may also exhibit chaos in the presence of large interwell oscillations, we focus on control of the mobile robot through intrawell oscillations exploiting the bistability of the origami structure to achieve multiple motion regimes. Since the origami structure will exhibit this bistability for a large range of parameters, we chose different parameters in the robot design than those used in the experiment. However we emphasize that origami is scalable making the units and scale of motion less relevant for our analysis. Limit cycle motion of the system is shown in Figure 8.11. Each of the velocities oscillates with the same frequency as that of the input making the limit cycle a loop in the $(u, \omega_1, \omega_2)$ space as shown in Figure 8.11 (c). Let us define $(\bar{u}, \bar{\omega}_1, \bar{\omega}_2)$ to be the average values of the velocities over one time period on the limit cycle. We find that $\bar{u} > 0$ and $\bar{\omega}_1 > 0$ making the limit cycle motion in the $(x, y)$ plane a circle on average as seen in Figure 8.11 (a).
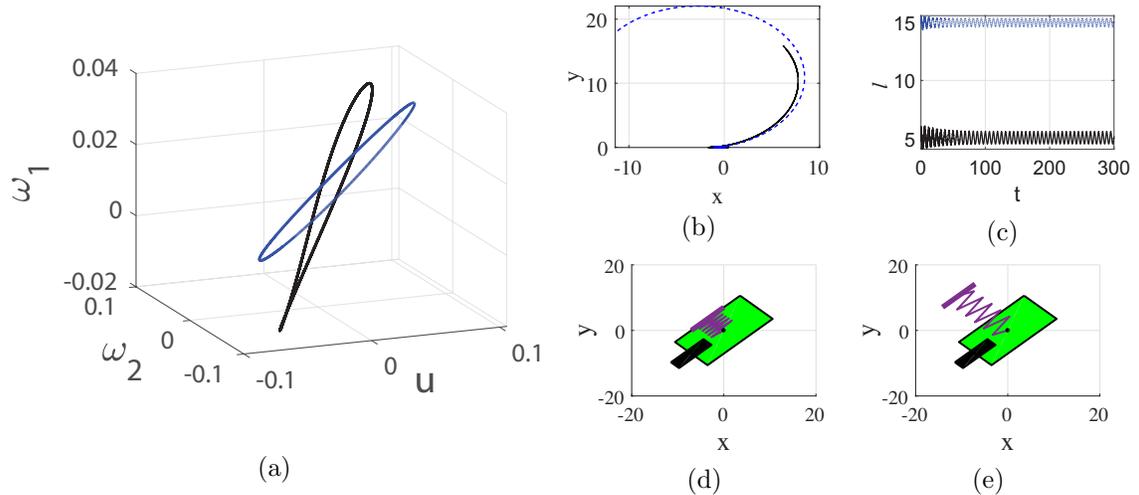


Figure 8.11: Sleigh response to periodic torque with $A = 100$, and $\Omega = 1$. Initial conditions are all zero except $\alpha(0) = \alpha_e$ for the blue dashed trajectory and $\alpha(0) = \alpha_c$ for the black solid lines in each subfigure. (a) The limit cycle in the velocity space, (b) The trajectory of the sleigh in the $(x, y)$ plane, (c) The length of the Kresling segment versus time, (d) schematic of the system in the fully-contracted position and (e) schematic of the sleigh in the fully-extended position. The geometry of the Kresling segment are $n = 8$, $p = 7$, $H = 5$, and $\mu_i = 0.8$ with stiffness $K = 5 \times 10^4$ and damping $c_k = 1$. Other parameters are $m_1 = 0.5$, $m_2 = 0.5$, $I_1 = I_2 = I_3 = 0.01$, $a = 10m$ and $c_u = 0.1$.

We find that the average values of all the limit cycle velocities change for each equilibrium position. When $\alpha(0) = \alpha_e$ we get $\bar{u} = 1.75 \times 10^{-2}$, $\bar{\omega}_1 = 1.47 \times 10^{-2}$ and $\bar{\omega}_2 = 0$ whereas for $\alpha(0) = \alpha_c$ we get $\bar{u} = 4.15 \times 10^{-3}$, $\bar{\omega}_1 = 7.94 \times 10^{-3}$ and $\bar{\omega}_2 = 0$. We find that when the Kresling segment rotation angle is close to $\alpha_e$ at which the segment is fully-extended we get both a higher $\bar{u}$ and $\bar{\omega}$; which means the sleigh absorbs more of the energy from the input torque in this position.

96

The radius of motion in the $(x, y)$ plane, however, depends on both of these. A similar effect is shown analytically for the elastic Chaplygin sleigh analyzed in [26] For this reason we see from Figure 8.11 (a) that the radius for $\alpha(0) = \alpha_c$ is actually smaller despite $\bar{\omega}_1$ being lower. We also find that in the fully-extended position, the robot occupies more space (Figures 8.11 (d) and (e)). This becomes another trade-off for the robot moving faster in this configuration. Based on the required task the robot is able to move faster, with a larger radius while occupying more space or move on a tight circle as a smaller robot.



<div align="center">(a)</div>



<div align="center">(b)</div>



<div align="center">(c)</div>



<div align="center">(d)</div>
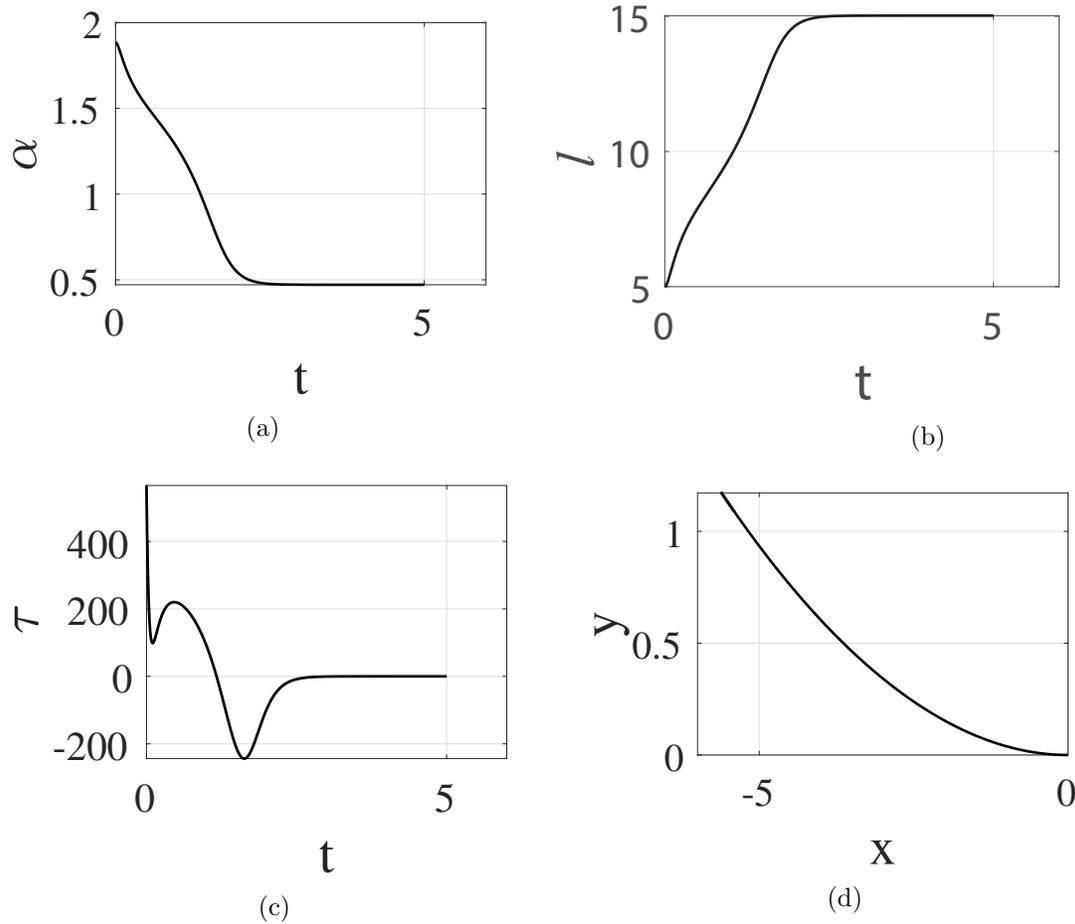
Figure 8.12: Sleigh transition procedure with $K_p = 400$ and $K_d = 400$. Initial conditions are all zero except $\alpha(0) = \alpha_c$. (a) The angle of rotation of the Kresling segment, (b) The length of the Kresling segment (c) Applied torque and (d) The trajectory in the $(x, y)$ plane. The geometry of the Kresling segment are $n = 8$, $p = 7$, $H = 5$, and $\mu_i = 0.8$ with stiffness $K = 5 \times 10^4$ and damping $c_k = 1$. Other parameters are $m_1 = 0.5$, $m_2 = 0.5$, $I_1 = I_2 = I_3 = 0.01$, $a = 10$ and $c_u = 0.1$.

In order to make use of the bistability we must be able force the Kresling segment to

<div align="center">97</div>

transition from one potential well to another. Since $\alpha$ and $l$ are mutually increasing and decreasing, a torque on the free face of the segment can be efficiently used to transition the segment to the other potential well. We show that this can be done with PD control. The proportional term allows us to define the desired potential well and the derivative term serves to compound with dissipation to decrease the convergence rate of the response. When we require the segment to transition wells; we switch off the periodic input and apply a control law of the form

**while** $(|\alpha - \alpha_d| > e)$ **do**

$\qquad \tau = -K_p(\alpha - \alpha_d) - K_d\omega_2$

**end while**

where $e$ is some chosen small error, $\alpha_d \in \{\alpha_e, \alpha_c\}$ is the desired value of the Kresling segment rotation angle and $K_p$ and $K_d$ are coefficients for the controller. The controller gains must be large enough to force a transition over the unstable position. The exact values required depend on initial conditions so we simply chose large values and show that that the control input is still of the same order as the periodic input. The feedback control law allows us to switch wells immediately even while the sleigh is moving. We first show a transition with zero initial conditions to focus on the dynamics of this controller.



<center>(a)                                               (b)</center>
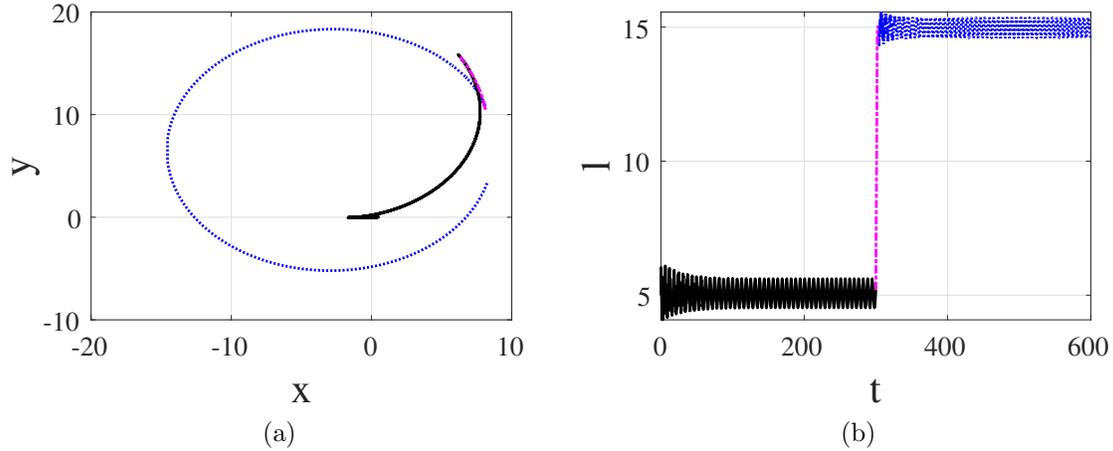
Figure 8.13: Robot switching from the fully-contracted position to the fully-extended potion. Oscillations about the fully-contracted position are shown in black lines, the transition in magenta dash-dotted lines and oscillations about the fully-extended position in blue dashed lines. (a) The trajectory in the plane. (b) The length of the Kresling segment. The geometry of the Kresling segment are $n = 8$, $p = 7$, $H = 5$, and $\mu_i = 0.8$ with stiffness $K = 5 \times 10^4$ and damping $c_k = 1$. Other parameters are $m_1 = 0.5$, $m_2 = 0.5$, $I_1 = I_2 = I_3 = 0.01$, $a = 10$ and $c_u = 0.1$.

In Figure 8.12 (a) and (b) we see that the segment is able to smoothly transition from one

<center>98</center>

equilibrium position to the other in under 5 seconds. Figure 8.12 (c) shows that the input required to transitions is of the same order as the sinusoidal input we use to steer the sleigh. The response of the sleigh itself is seen in Figure 8.12 (d).

A simulation of the control law is shown in Figure 8.13. The sleigh begins with $\alpha(0) = \alpha_c$ and we apply a periodic input with $A = 100$ and $\Omega = 1$ for $t \in [0, 300)$ and then the origami sleigh is required to transition to the other stable configuration using the transition procedure. We then apply the same periodic input until $t = 600$. We see that during the first three hundred seconds the sleigh first travels backward briefly during the transient phase and then travels along a circle with $\bar{u} = 4.15 \times 10^{-3}$ and $\bar{\omega}_1 = 7.94 \times 10^{-3}$ (Figure 8.13 (a)). The system then transitions to the other stable configuration. Once the periodic input starts again we see another transient phase where $u$ is on average less than zero before the sleigh settles to a limit cycle with $\bar{u} = 1.75 \times 10^{-2}$ and $\bar{\omega}_1 = 1.47 \times 10^{-2}$. The system can therefore change its speed and radius travel using the torque on the Kresling segment as the only control input.

# Chapter 9

# Conclusion

Many recent works use techniques in [75] to develop gaits for underactuated nonholonomic systems. Most such works, however, consider systems with only one dynamic variable and the dynamic equations are driftless allowing for generation of simple gaits via Stokes theorem techniques. In this dissertation we have developed motion planning for underactuated systems that require modeling through multiple dynamic equations but contain only one control input. This is done by modeling the steady state dynamics of the system through the harmonic balance method. We map the relationship between an input periodic torque and the steady state periodic response of a system and use this relationship to achieve desired motion in the $(x, y)$ plane. This is a novel method to control a planar mobile robot and similar techniques are now being implemented in fish robots [46, 68]. Future work on this will involve controlling the transient phase of the motion as well as the error in following a path. There is also much more work that can be done in applying the techniques in this dissertation to swimming robots. Preliminary results on this are discussed in Chapter 3 and published in [68, 70]. Similar work is now also being done at the University of Maryland [46] using feedback instead of a time dependent periodic input. Using feedback has some advantages like often being easier to work with analytically, however accurately predicting the eventual motion of the sleigh can be very difficult without potentially unrealistic assumptions.

Underactuated systems such as those considered in this dissertation often arise due to the presence of passive degrees of freedom. We show how passive degrees of freedom can increase the range of dynamics exhibited by a nonholonomic system leading to phenomena such as chaos and limit cycles. The presence of a spring on such a passive degree of freedom was found to have a stabilizing

influence leading to regular dynamics such as limit cycles and convergence to fixed points. This is also true for periodically forced systems. In Chapter 7 we show that the addition of a passive degree of freedom can improve the locomotion characteristics of a nonholonomic system by allowing for higher speed and energy efficiency to be achievable. We also introduce two additional ways that elastic potentials can be introduced in nonholonomic systems, namely compliance and origami. Such mechanisms exhibit many mechanical and dynamic properties which can be useful in designing robots.

# Bibliography

[1] L. Belzile and B. Birglen. A compliant self-adaptive gripper with proprioceptive haptic feedback. *Autonomous Robots*, 36:76–91, 2014.

[2] Priyanka Bhovad and Suyi Li. Using multi-stable origami mechanism for peristaltic gait generation: A case study. In *ASME 2018 International Design Engineering Technical Conferences and Computers and Information in Engineering Conference*, pages V05BT07A061–V05BT07A061. American Society of Mechanical Engineers, 2018.

[3] Ivan Bizyaev, Alexey V Borisov, Valery V Kozlov, Ivan S Mamaev, et al. Fermi-like acceleration and power-law energy growth in nonholonomic systems. *arXiv preprint arXiv:1807.06262*, 2018.

[4] Ivan A Bizyaev. The inertial motion of a roller racer. *Regular and Chaotic Dynamics*, 22(3):239–247, 2017.

[5] Ivan A Bizyaev, Alexey V Borisov, and Sergey P Kuznetsov. The chaplygin sleigh with friction moving due to periodic oscillations of an internal mass. *Nonlinear Dynamics*, pages 1–16, 2019.

[6] A. M. Bloch. *Nonholonomic Mechanics and Control*. Springer Verlag, 2003.

[7] A. M. Bloch, P. S. Krishnaprasad, J. E. Marsden, and R. M. Murray. Nonholonomic Mechanical Systems with Symmetry. *Archive for Rational Mechanics and Analysis*, 136:21–99, 1996.

[8] A. V. Borisov and I. S. Mamaev. On the history of the development of the nonholonomic mechanics. *Regular and Chaotic Dynamics*, 7(1):43–47, 2003.

[9] A. V. Borisov and I. S. Mamaev. The dynamics of a chaplygin sleigh. *Journal of Applied Mathematics and Mechanics*, 73(2):156–161, 2009.

[10] Alexey Vladimirovich Borisov and Ivan Sergeevich Mamaev. On the history of the development of the nonholonomic dynamics. *Regular and Chaotic Dynamics*, 7(1):43–47, 2002.

[11] Francesco Bullo and Miloš Žefran. On mechanical control systems with nonholonomic constraints and symmetries. *Systems & Control Letters*, 45(2):133–143, 2002.

[12] Frans Cantrijn, Jorge Cortés, Manuel De León, and David Martin De Diego. On the geometry of generalized chaplygin systems. In *Mathematical Proceedings of the Cambridge Philosophical Society*, volume 132, pages 323–351. Cambridge University Press, 2002.

[13] Ofir Chakon and Yizhar Or. Analysis of underactuated dynamic locomotion systems using perturbation expansion: the twistcar toy example. *Journal of Nonlinear Science*, 27(4):1215–1234, 2017.

[14] O. Chakron and Y. Or. Analysis of underactuated dynamic locomotion systems using perturbation expansion: The twistcar toy example. *Journal of Nonlinear Science*, 2017.

[15] S. A. Chaplygin. On the theory of the motion of nonholonomic systems : The reducing multiplier theorem. *Translated version in Regular and Chaotic Dynamics*, 2008.

[16] W. Crooks, S. Rozen-Levy, B. Trimmer, C. Rogers, and W. Messner. Passive gripper inspired by manduca sexta and the fin ray® effect. *The International Journal of Robotics Research*, 35(1-3):161–185, 2017.

[17] Tony Dear, Scott David Kelly, Matthew Travers, and Howie Choset. Mechanics and control of a terrestrial vehicle exploiting a nonholonomic constraint for fishlike locomotion. In *ASME 2013 Dynamic Systems and Control Conference*, pages V002T33A004–V002T33A004. American Society of Mechanical Engineers, 2013.

[18] Tony Dear, Scott David Kelly, Matthew Travers, and Howie Choset. Snakeboard motion planning with viscous friction and skidding. In *Robotics and Automation (ICRA), 2015 IEEE International Conference on*, pages 670–675. IEEE, 2015.

[19] R. Deimel and O. Brock. A novel type of compliant and underactuated robotic hand for dexterous grasping. *The International Journal of Robotics Research*, 14(4):161–185, 2016.

[20] Stijn Derammelaere, Cosmin Copot, Michiel Haemers, Florian Verbelen, Bram Vervisch, Clara Ionescu, and Kurt Stockman. Realtime locomotion control of a snakeboard robot based on a novel model, enabling better physical insights. *European Journal of Control*, 45:57–64, 2019.

[21] M. H. Dickinson, Fritz-Olaf Lehmann, and S. P. Sane. Wing rotation and the aerodynamic basis of insect flight. *Science*, 284:1954 – 1960, 1999.

[22] Chaotic dynamics of the Chaplygin sleigh with a passive internal rotor. V. fedonyuk and p. tallapragada. *Nonlinear Dynamics*, 2018.

[23] Determining Lyapunov exponents from a time series. A. wolf and j. b. swift and h. l. swinney and j. a. vatsano. *Physica D : Nonlinear Phenomena*, 16(3):285–317, 1985.

[24] Vitaliy Fedonyuk and Phanindra Tallapragada. The dynamics of a two link chaplygin sleigh driven by an internal momentum wheel. In *American Control Conference (ACC), 2017*, pages 2171–2175. IEEE, 2017.

[25] Vitaliy Fedonyuk and Phanindra Tallapragada. Sinusoidal control and limit cycle analysis of the dissipative chaplygin sleigh. *Nonlinear Dynamics*, pages 1–12, 2018.

[26] Vitaliy Fedonyuk and Phanindra Tallapragada. The dynamics of a chaplygin sleigh with an elastic internal rotor. *Regular and Chaotic Dynamics*, 24(1):114–126, 2019.

[27] Vitaliy Fedonyuk, Phanindra Tallapragada, and Yongqiang Wang. Limit cycle analysis and control of the dissipative chaplygin sleigh. In *ASME Dynamic Systems and Control Conference*, 2017.

[28] NM Ferrers. Extension of lagrange's equations. *Quart. J. Pure Appl. Math*, 12(45):1–5, 1872.

[29] E T Filipov, T Tachi, and G H Paulino. Origami tubes assembled into stiff, yet reconfigurable structures and metamaterials. *Proceedings of the National Academy of Sciences*, 112(40):12321–12326, oct 2015.

[30] R. Genesio and A. Tesi. Harmonic balance methods for the analysis of chaotic dynamics in nonlinear systems. *Automatica*, 28(3):531–548, 1992.

[31] Simon D Guest and Sergio Pellegrino. The folding of triangulated cylinders, part i: geometric considerations. *Journal of applied mechanics*, 61(4):773–777, 1994.

[32] E. Gutman and Y. Or. Simple model of a planar undulating magnetic microswimmer. *Physical Review E*, 90(1):013012, 2014.

[33] D. W. Haldane, C. S. Casarez, J. T. Karras, J. Lee, E. W. Schaler C. Li, A. O. Pullin, D. Yun, H. Ota, A. Javey, and R. S. Fearing. Integrated manufacture of exoskeletons and sensing structures for folded millirobots. *Journal of Mechanisms and Robotics*, 7(2):021011, 2015.

[34] Larry L Howell. *Compliant mechanisms*. John Wiley & Sons, 2001.

[35] Giles W Hunt and Ichiro Ario. Twist buckling and the foldable cylinder: an exercise in origami. *International Journal of Non-Linear Mechanics*, 40(6):833–843, 2005.

[36] Auke Jan Ijspeert. Central pattern generators for locomotion control in animals and robots: a review. *Neural networks*, 21(4):642–653, 2008.

[37] K. Jayaram and R. J. Full. Cockroaches traverse crevices, crawl rapidly in confined spaces, and inspire a soft, legged robot. *Proceedings of the National Academy of Sciences*, 113(8):950–957, 2016.

[38] Brian D Jensen and Larry L Howell. Bistable configurations of compliant mechanisms modeled using four links and translational joints. *Journal of Mechanical Design*, 126(4):657–666, 2004.

[39] Brian D Jensen, Larry L Howell, and Linton G Salmon. Introduction of two-link in-plane, bistable compliant mems. In *Proceeding of the 1998 ASME Design Engineering Technical Conferences, DETC98/MECH-5837*, September 13-16 1998.

[40] Cai Jianguo, Deng Xiaowei, Zhou Ya, Feng Jian, and Tu Yongming. Bistable behavior of the cylindrical origami structure with kresling pattern. *Journal of Mechanical Design*, 137(6):061406, 2015.

[41] S. D. Kelly, M. J. Fairchild, P. M. Hassing, and P. Tallapragada. Proportional heading control for planar navigation: The chaplygin beanie and fishlike robotic swimming. In *Proceedings of the American Control Conference*, 2012.

[42] Scott D Kelly and Richard M Murray. Geometric phases and robotic locomotion. *Journal of Robotic Systems*, 12(6):417–431, 1995.

[43] Kyoung Chul Koh and Hyung Suck Cho. A smooth path tracking algorithm for wheeled mobile robots with dynamic constraints. *Journal of Intelligent and Robotic Systems*, 24(4):367–385, 1999.

[44] Ilya Kolmanovsky and N Harris McClamroch. Hybrid feedback laws for a class of cascade nonlinear control systems. *IEEE Transactions on Automatic Control*, 41(9):1271–1282, 1996.

[45] Biruta Kresling. Natural twist buckling in shells: From the hawkmoth's bellows to the deployable kresling-pattern and cylindrical miuraori. In *Proceedings of the 6th International Conference on Computation of Shell and Spatial Structures*, pages 1–4, 2008.

[46] Jinseong Lee, Brian Free, Shyline Santana, and Derek A Paley. State-feedback control of an internal rotor for propelling and steering a flexible fish-inspired underwater vehicle. In *2019 American Control Conference (ACC)*, pages 2011–2016. IEEE, 2019.

[47] S Li and K W Wang. Fluidic origami: a plant-inspired adaptive structure with shape morphing and stiffness tuning. *Smart Materials and Structures*, 24(10):105031, 2015.

[48] Suyi Li, Hongbin Fang, Sahand Sadeghi, Priyanka Bhovad, and Kon-Well Wang. Architected origami materials: How folding creates sophisticated mechanical properties. *Advanced Materials*, 31(5):1805282, 2019.

[49] Suyi Li and K. W. Wang. Fluidic origami with embedded pressure dependent multi-stability : a plant inspired innovation. *Journal of The Royal Society Interface*, 12(111):20150639, 2015.

[50] Yu G Martynenko. The theory of the generalized magnus effect for non-holonomic mechanical systems. *Journal of Applied Mathematics and Mechanics*, 68(6):847–855, 2004.

[51] Alexander J McDonald and Kirk T McDonald. The rolling motion of a disk on a horizontal plane. *arXiv preprint physics/0008227*, 2000.

[52] V. Megaro, J. Zehnder, M. Bacher, S. Coros, M. Gross, and B. Thomaszewski. A computational design tool for compliant mechanisms. *ACM Transactions on Graphics*, 36(4):82–94, 2019.

[53] Andrija Milojević. Compliant bistable mechanisms, 2011.

[54] R. Murray and S. Sastry. Nonholonomic motion planning : Steering using sinusoids. *IEEE Transactions on Automatic Control*, 30(5):700–716, 1993.

[55] Richard M Murray and S Shankar Sastry. Steering nonholonomic systems in chained form. In *Decision and Control, 1991., Proceedings of the 30th IEEE Conference on*, pages 1121–1126. IEEE, 1991.

[56] Richard M Murray and S Shankar Sastry. Nonholonomic motion planning: Steering using sinusoids. *IEEE Transactions on Automatic Control*, 38(5):700–716, 1993.

[57] Nigamaa Nayakanti, Sameh H. Tawfick, and A. John Hart. Twist Coupled Kirigami Cellular Metamaterials and Mechanisms. *Extreme Mechanics Letters*, 2017.

[58] Anibal Ollero and Guillermo Heredia. Stability analysis of mobile robot path tracking. In *Proceedings 1995 IEEE/RSJ International Conference on Intelligent Robots and Systems. Human Robot Interaction and Cooperative Robots*, volume 3, pages 461–466. IEEE, 1995.

[59] Patrick G Opdahl, Brian D Jensen, and Larry L Howell. An investigation into compliant bistable mechanisms. In *Proceeding of the 1998 ASME Design Engineering Technical Conferences*, pages 13–16, September 13-16 1998.

[60] J. M. Osborne and D. V. Zenkov. Steering the chaplygin sleigh by a moving mass. In *Proceedings of the American Control Conference*, 2005.

[61] J. Ostrowski, A. Lewis, R. Murray, and J. Burdick. Nonholonomic mechanics and locomotion: the snakeboard example. In *Proceedings of the Control and Decision Conference*, pages 2391–2397, 1994.

[62] James P Ostrowski, Jaydev P Desai, and Vijay Kumar. Optimal gait selection for nonholonomic locomotion systems. *The International journal of robotics research*, 19(3):225–237, 2000.

[63] Jim Ostrowski and Joel Burdick. Gait kinematics for a serpentine robot. In *Robotics and Automation, 1996. Proceedings., 1996 IEEE International Conference on*, volume 2, pages 1294–1299. IEEE, 1996.

[64] Alexander Pagano, Tongxi Yan, Brian Chien, A Wissa, and S Tawfick. A crawling robot driven by multi-stable origami. *Smart Materials and Structures*, 26(9):094007, 2017.

105

[65] Passive, Active Flow Control by Swimming Fishes, and Mammals. F. e. fish and g. v. lauder. *Annual Review of Fluid Mechanics*, (38):193–224, 2006.

[66] C. Piccardi. Bifurcations of limit cycles in periodically forced nonlinear systems: the harmonic balance approach. *IEEE Transactions on Circuits and Systems I: Fundamental Theory and Applications*, 41(4):315–320, 2002.

[67] B. Pollard, V. Fedonyuk, and P. Tallapragada. Limit cycle behavior and model reduction of an oscillating fish-like robot. In *Proceedings of the ASME 2018 Dynamic Systems and Control Conference*, 2018.

[68] B. Pollard, V. Fedonyuk, and P. Tallapragada. Swimming on limit cycles with nonholonomic constraints. *Nonlinear Dynamics*, 2019.

[69] B. Pollard and P. Tallapragada. An aquatic robot propelled by an internal rotor. *IEEE/ASME Transaction on Mechatronics*, 2016.

[70] Beau Pollard, Vitaliy Fedonyuk, and Phanindra Tallapragada. Limit cycle behavior and model reduction of an oscillating fish-like robot. In *ASME 2018 Dynamic Systems and Control Conference*, pages V001T04A006–V001T04A006. American Society of Mechanical Engineers, 2018.

[71] Beau Pollard and Phanindra Tallapragada. Passive appendages improve the maneuverability of fish-like robots. In *APS Division of Fluid Dynamics Meeting Abstracts*, 2017.

[72] Passive propulsion in vortex wakes. D. n. beal and f. s. hover and m. s. triantafyllou and j. c. liao and g. v. lauder. *Journal of Fluid Mechanics*, (549):385 – 402, 2006.

[73] Simon Rutishauser, Alexander Sprowitz, Ludovic Righetti, and Auke Jan Ijspeert. Passive compliant quadruped robot using central pattern generators for locomotion control. In *2008 2nd IEEE RAS & EMBS International Conference on Biomedical Robotics and Biomechatronics*, pages 710–715. IEEE, October 19-22 2008.

[74] M. Schenk and S. D. Guest. Origami folding: A structural engineering approach. In *Origami 5 Fifth International Meeting of Origami Science Mathematics and Education*, pages 1–16, 2011.

[75] Elie A Shammas. Generalized motion planning for underactuated mechanical systems. *The dissertation thesis*, 2006.

[76] Alfred Shapere and Frank Wilczek. Geometry of self-propulsion at low reynolds number. *Journal of Fluid Mechanics*, 198:557–585, 1989.

[77] Jarrod M Snider et al. Automatic steering methods for autonomous automobile path tracking. *Robotics Institute, Pittsburgh, PA, Tech. Rep. CMU-RITR-09-08*, 2009.

[78] P. Tallapragada. A swimming robot with an internal rotor as a nonholonomic system. *Proceedings of the American Control Conference*, 2015.

[79] P. Tallapragada and V. Fedonyuk. Steering a chaplygin sleigh using periodic impulses. *Journal of Computational and Nonlinear Dynamics*, 2017.

[80] P. Tallapragada and S. D. Kelly. Reduced-order modeling of propulsive vortex shedding from a free pitching hydrofoil with an internal rotor. In *Proceedings of the 2013 American Control Conference*, 2013.

[81] P. Tallapragada and S. D. Kelly. Integrability of velocity constraints modeling vortex shedding in ideal fluids. *Journal of Computational and Nonlinear Dynamics*, 2016.

106

[82] J. Whitney and R. Wood. Aeromechanics of passive rotation in flapping flight. *Journal of Fluid Mechanics*, 660:197 – 220, 2010.

[83] O. Wiezel and Y. Or. Optimization and small-amplitude analysis of purcells three-link microswimmer model. *Proceedings of the Royal Society A*, 2016.

[84] Jeffrey S Wit. Vector pursuit path tracking for autonomous ground vehicles. Technical report, Florida University Gainesville Center for Intelligent Machines and Robotics, 2000.

[85] H. Yasuda and J. Yang. Reentrant origami-based metamaterials with negative Poisson's ratio and bistability. *Physical Review Letters*, 114(18):1–5, 2015.